Department of Physics

Cavendish Laboratory

Degenerate Bose Gases in a Uniform Potential

Igor Gotlibovych

Churchill College

April 2014

This dissertation is submitted for the degree of
Doctor of Philosophy

Cavendish Laboratory

University of Cambridge

J J Thomson Avenue

Cambridge CB3 0HE

UK

Declaration

I declare that this thesis is my own work and is not substantially the same as any that I have submitted or am currently submitting for a degree, diploma or any other qualification at any other university. No part of this thesis has already been or is being concurrently submitted for any such degree, diploma or any other qualification. This thesis does not exceed the word limit of sixty thousand words, including tables, footnotes, bibliography and appendices, set out by the Faculty of Physics and Chemistry.

Abstract

This thesis describes the first ever implementation of an atomic Bose-Einstein condensate (BEC) in a uniform three-dimensional system. We prepare a degenerate sample of ^{87}Rb in a customizable uniform box trap and perform a range of experiments demonstrating fundamental quantum-mechanical and statistical effects.

A dilute vapour of ^{87}Rb atoms is first cooled to degeneracy in a conventional harmonic trap. The single-chamber apparatus described in this thesis utilizes evaporative cooling in an optimized hybrid trap to produce large degenerate samples of over 3×10^5 atoms with a repetition rate of $25\,\mathrm{s}$. The partially condensed gas is then loaded into a uniform optical box formed by intersecting three specially shaped blue-detuned laser beams: two parallel sheet-like beams cross a tube beam at right angles, creating a dark cylinder-shaped trap. The gravitational force is cancelled using an external magnetic field gradient, creating a region of space with a nearly uniform potential. The gas is than evaporatively cooled to condensation in the uniform trap.

We than study partially condensed samples using absorption imaging in time of flight. We develop the methods necessary to extract thermodynamic properties of the sample from these images. We characterize the critical point for condensation and observe saturation of the thermal component in a partially condensed cloud, in agreement with Einsteins textbook picture of a purely statistical phase transition. Further, we observe the quantum Joule-Thomson effect, namely isoenthalpic cooling of an (essentially) ideal gas. In our experiments this cooling occurs spontaneously, due to energy-independent collisions with the background gas in the vacuum chamber. We extract a Joule-Thomson coefcient $\mu_{\mathrm{JT}} > 10^9\,\mathrm{K/bar}$, about ten orders of magnitude larger than observed in classical gases. We show that quantum-statistical effects dominate over the interaction effects.

Lastly, we study the ground-state properties of the homogeneous atomic Bose gas using high-resolution Bragg spectroscopy. For a range of box sizes, up to $70\,\mu\mathrm{m}$, we directly observe Heisenberg-limited momentum uncertainty of Bose-condensed

atoms. We measure the condensate interaction energy with a precision of $k_\mathrm{B} \times 100\,\mathrm{pK}$ and study, both experimentally and numerically, the dynamics of free expansion of the interacting condensate released from the box potential. All our measurements are in good agreement with theoretical expectations for a perfectly homogeneous gas, which also establishes the uniformity of our optical-box system on a sub-nK energy scale.

While uniform systems have always provided a basis for the theoretical description of ultra-cold Bose gases, all experimental studies to date where conducted in non-uniform external potentials, most commonly in harmonic traps. Our experiments allowed the first direct experimental validation of many theoretical predictions, and paved the way for future novel studies.

Acknowledgements

This thesis is the culmination of several years of hard work. It was a dominant and formative part of my life throughout these years, and it would not have been the same without the people who guided and supported me, both in and outside the lab. First and foremost, my thanks goes to my supervisor Zoran Hadzibabic for allowing me to join his group. While our world views might differ, I could not have wished for a better mentor in the field of physics. It is due to his vision and optimism that our research has advanced to the stage presented here. I would further like to thank the original members of our group who laid the foundations for every experiment I have been involved with: during their time here, Naaman Tammuz and Robbie Campbell always offered helpful advice, and their publications were essential for every newcomer to the group. Continuity was upheld by Stuart Moulder and Scott Beattie, who were at hand for most of my PhD. Alex Gaunt's experimental and computational contributions to this work are hard to over-estimate. Further, both Alex and Richard Fletcher were a great help with the preparation of every manuscript, including this thesis. I would like to extend my gratitude to Robert Smith, who has been (and continues being) a pillar of our group, and possesses the uncanny ability to bring any experiment back to life when all other attempts have failed. With Nir Navon and Martin Robert-de-Saint-Vincent, the latest postdoctoral researchers to join our group, providing advice and supervision, I feel that current as well as future students are in safe hands.

Of all the members of our research group, it is undeniably Tobias Schmidutz, whom I have worked with closely for three years, who deserves my deepest thanks. I have spent more hours with him than any other person over the course of my PhD, and I could not have wished for a better friend and colleague. Without his help, the completion of this work would have hardly been possible.

Last but not least, I would like to thank Matt, Giulia, my fiends and my family for believing in me unconditionally.

Contents

Chapter 1

Introduction

1.1 Background

Quantum mechanics has proven to be one of the most successful modern-day physical theories, its fundamentals remaining unchallenged for nearly a century. From the early 20th century onwards, the description of many-particle systems has been central to the development, understanding and applications of the quantum theory: while a single particle in an external potential is, in many cases, a useful model, our world is inherently many-particle. Indeed, most phenomena in areas as varied as atomic physics, condensed matter physics, and stellar physics, can only be understood in terms of a fully quantum theory. Historically significant examples include superfluidity, superconductivity, and neutron stars.

Interestingly, Planck's quantized description of black-body radiation - one of the most significant steps towards a consistent quantum theory, implicitly introduced several of the key concepts that were to prove instrumental in extending single-particle quantum mechanics (which was, in fact, not formulated carefully until decades after Planck) to many-body systems. These concepts are: first, the identification of microstates in statistical mechanics with different occupations of quantized energy levels; second, the indistinguishability of identical particles; and third, the classification of all particles (elementary or composite) into two classes, namely bosons and fermions, depending on their spin. We briefly review each in turn.

First, we recall that for any particle confined in an external potential, quantum theory predicts the existence of discrete energy levels, each with their associated eigenstate, that the particle can occupy. For example, a quantum-mechanical harmonic oscillator has the energy levels $E_n = (n + 1/2)\hbar\omega$ for $n = 0, 1, 2, \ldots$, where ω

is the corresponding "classical" oscillation frequency. If the oscillator is in thermal equilibrium with a bath of temperature T, the probability to find state N occupied is proportional to the Boltzmann factor $\exp[-E_n/(k_BT)]$. The probalility to find the particle in it's ground state ($n = 0$) increases rapidly as the temperature is reduced below $k_BT \sim \hbar\omega$. We would say that at this temperature the system transitions from a predominantly incoherent thermal state, described well by classical statistical mechanics, into one that is predominantly coherent and thus fully quantum.

If the same harmonic trap contains many non-interacting particles, each will occupy one of the energy levels E_n. We would have to associate a microstate, with its respective energy, with each possible arrangement of the particles between the levels. For example, 3 particles could be distributed as follows: particle 1 in level 0, particles 2 and 3 in level 1, or particle 2 in level 0, particles 1 and 3 in level 1, etc. [Fig. 1.1 (a)]. However, as long as the particles are distinguishable, each will behave essentially independently from the others.
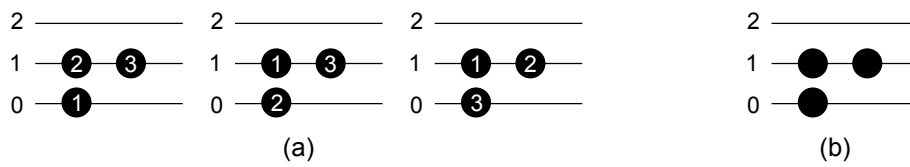
Figure 1.1: Three different microstates of distinguishable particles (a), and the corresponding single microstate of indistinguishable particles (b).

This changes if the particles are indistinguishable - since we can only tell the number of particles in each state, all three microstates in the above example are *identical*, and there is only one microstate corresponding to 1 particle in level 0 and 2 particles in level 1 [Fig. 1.1 (b)]. In addition, quantum mechanics places limitations on the allowed occupation number for each level: for particles with a half-integer spin - fermions - it can only be 0 or 1, while for particles with integer spin - bosons - it is unrestricted[1].

The occupations of different levels in an ensemble of identical particles will thus be described by a different statistical distribution depending on the type of particles: Fermi-Dirac statistics [1, 2] for fermions, and Bose-Einstein statistics [3] for bosons. Further, both distributions will deviate significantly from their classical counterpart

---

[1]Strictly speaking, the constraint is on the exchange symmetry of the many-particle wavefunction (odd for fermions, even for bosons). We must thus consider a basis of suitable many-particle eigenstates. However, it can be shown that the description given in the text is identical for the purposes of statistical mechanics.

for temperatures *much higher* than $\hbar\omega$: in fact, quantum-mechanical nature will manifest itself for $k_{\mathrm{B}}T \sim N^{1/3} \times \hbar\omega$, where N is the number of particles - a large factor for most macroscopic systems[2]. Such a gas is called *degenerate*. A degenerate Fermi gas is characterised by nearly constant occupation over low-lying levels up to a given threshold, with a rapid decrease in occupation for higher energies [Fig. 1.2 (a)]. A degenerate Bose gas exhibits *macroscopic occupation* of the ground state [Fig. 1.2 (b)] - this is because at any given T, Bose-Einstein statistics only allow finitely many particles in the excited states ($n > 0$), the excess forcibly accumulating in the ground state. This behaviour of bosons was first studied theoretically by
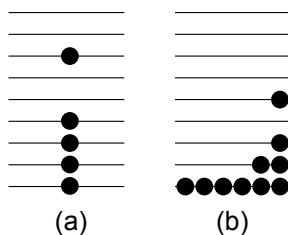
Figure 1.2: Typical occupation of low-lying energy levels in a degenerate Fermi (a) and Bose (b) gas.

Einstein [4, 5], and bears the name of Bose-Einstein condensation, hinting at the fact that, thermodynamically, it represents a (second-order) phase transition - one driven by quantum statistics rather than inter-particle interactions. Both superfluidity and superconductivity have since been linked to the behaviour of degenerate bosons. While these systems are generally dense and strongly interacting, the production of weakly interacting "textbook" condensates eluded experimentalists for a further 70 years. Most gases undergo an interaction-driven transition to a liquid (or solid) phase long before they reach quantum degeneracy. This necessitates the use of extremely dilute clouds, pushing the transition temperature into the nK range. Development of techniques that would allow cooling to these low temperatures thus presented the main experimental challenge, that was eventually overcome by the groups of Wieman and Cornell [6] and Ketterle [7] in 1995.

The Bose-Einstein condensates (BECs) of ultra-cold atoms have since proven to be a highly prolific system for fundamental studies, not least because they allow tuning of a wide range of parameters - from trapping geometry to inter-particle interaction strength. Suggested applications include quantum computing, simulations of superfluid and superconducting behaviour, and precision metrology [8].

---

[2]The exact scaling with N will depend on the external trapping potential, e.g. taking the form $N^{2/3}$ in a uniform system (see Chapter 2)

However, most experiments on ultra-cold atomic gases to date have been conducted in harmonically trapped atomic clouds, while conventional many-body systems are uniform and transitionally invariant. Various methods have been developed to overcome this problem and extract uniform-system properties from a harmonically trapped sample [9–18] - most rely on the local density approximation (LDA, see later). Sometimes harmonic trapping can even be advantageous, allowing simultaneous mapping of uniform-system properties at different (local) particle densities. On the other hand, in many important situations local approaches are inherently limiting, for example, for studies of critical behavior with diverging correlation lengths. The possibility to directly study a spatially uniform quantum-degenerate gas has thus remained an important experimental challenge. So far, atomic Bose-Einstein condensates (BECs) have been loaded into elongated [9] or toroidal [10] traps that are uniform along only one direction while still harmonic along the other two directions.

This Thesis describes the first ever implementation of a truly uniform degenerate Bose gas, as well as a variety of experimental studies performed on this system. While many of the techniques we use to study uniform Bose-Einstein condensates derive from those used previously on harmonically trapped clouds, there are also significant differences which we seek to highlight throughout this work. Our measurements allow the most direct tests of the theory of the uniform Bose gas, but also serve as a benchmark for the quality of our system and its suitability for future studies.

1.2 Thesis outline

This thesis is structured as follows:

- Chapter 2 provides a review the theoretical framework used to describe Bose-Einstein condensates in arbitrary power-low potentials, including the uniform case.

- Chapter 3 contains technical details of our BEC experiment, and describes production of harmonically trapped condensates.

- Chapter 4 explains how we succeeded in creating a uniform box trap, and explains how the atoms can be loaded from the harmonic into the box trap and cooled to degeneracy.

- Chapter 5 presents an extensive characterization of the thermodynamic properties of partially degenerate uniform clouds, including transition temperature and heat capacity.

- Chapter 6 focuses on the ground state properties of the uniform BEC, and presents results of two-photon Bragg spectroscopy performed on quasi-pure samples.

- Finally, in Chapter 7 we summarize our findings and point out potential implications of our work and future research directions.

1.3 Publications arising from this work

Many of the results presented in this Thesis were published over the course of the past few years.

1. Methods described in Chapter 3 are summarized in

   I. Gotlibovych, T. F. Schmidutz, S. Moulder, R. L. D. Campbell, N. Tammuz, R. J. Fletcher, A. L. Gaunt, S. Beattie, R. P. Smith, and Z. Hadzibabic, "A compact single-chamber apparatus for Bose-Einstein condensation of ^{87}Rb," *arXiv:1212.4108*, Dec. 2012 [19]

2. Key experimental results of Chapter 4 first appeared in

   A. L. Gaunt, T. F. Schmidutz, I. Gotlibovych, R. P. Smith, and Z. Hadzibabic, "Bose-Einstein Condensation of Atoms in a Uniform Potential," *Physical Review Letters*, vol. 110, p. 200406, May 2013 [20]

3. Experimental studies presented in Chapter 5 formed the basis for

   T. F. Schmidutz, I. Gotlibovych, A. L. Gaunt, R. P. Smith, N. Navon, and Z. Hadzibabic, "Quantum Joule-Thomson Effect in a Saturated Homogeneous Bose Gas," *Physical Review Letters*, vol. 112, p. 040403, Jan. 2014 [21]

4. Measurements presented in Chapter 6 were published in

   I. Gotlibovych, T. F. Schmidutz, A. L. Gaunt, N. Navon, R. O. Smith, and Z. Hadzibabic "Observing the Ground-State Properties of an Interacting Homogeneous Bose Gas" *in preparation*, 2014 [22]

Chapter 2

Theory of the Ideal Bose Gas in an External Potential

In this Chapter, we briefly review the important theoretical results on the thermo-dynamics of an ideal Bose gas confined in a power-law potential, to be referred to repeatedly in subsequent chapters. We start by considering a power-law potential of the form

$$U(\mathbf{r}) = \sum_i A_i |x_i|^{s_i} \tag{2.1}$$

in three dimensions ($i = 1, 2, 3$). A potential with $s_1 = s_2 = s_3 = s$ (or, more generally, $s^{-1} = (s_1^{-1} + s_2^{-1} + s_3^{-1})/3$) will have the same thermodynamic properties as the corresponding spherically-symmetric potential $U(\mathbf{r}) = Ar^s$. Thus, $s = 2$ corresponds to a harmonic trap, while a uniform trap is obtained in the limit $s \to \infty$[1]. Finding the discrete single-particle energy levels is generally non-trivial[2]. However, most of the time we are dealing with a large number of excited states, and it is convenient to replace all thermodynamic sums over these states by integrals of the form

$$\sum_{i=1}^n f(\epsilon_i)\epsilon_i \approx \int_0^{\epsilon_n} f(\epsilon)g(\epsilon)\mathrm{d}\epsilon, \tag{2.2}$$

where we have defined the *density of states* $g(\epsilon)$. Approximating the number of accessible states with energies in the interval $[\epsilon, \epsilon + \mathrm{d}\epsilon]$ by $g(\epsilon)\mathrm{d}\epsilon$ is known as the semi-classical approximation [23]. In degenerate Bose gases, this approximation obviously breaks down for the ground state, which must be treated separately.

---

[1] At the same time, we must set $A_i \propto r_0^{-s_i}$ if we are to maintain a constant volume.

[2] Well-known textbook cases which have analytic solutions include the harmonic trap and the rectangular uniform box.

The functional form of $g(\epsilon)$ depends on the trapping potential. We define the parameter α according to

$$\alpha = \frac{3}{2} + \sum_i \frac{1}{s_i} \quad \text{or} \quad \alpha = \frac{3}{2} + \frac{3}{s}. \tag{2.3}$$

Our definition of α is consistent with [23], while [24] uses $\eta \equiv \alpha - 1$. Using this definition, the in-trap density of states can be written as [23, 24]

$$g(\epsilon) = C_\alpha \epsilon^{\alpha-1} \equiv \frac{1}{\Gamma(\alpha)E_\alpha}\left(\frac{\epsilon}{E_\alpha}\right)^{\alpha-1}, \tag{2.4}$$

where $\Gamma(\alpha) = \int_0^\infty x^{\alpha-1}e^{-x}\mathrm{d}x$ is the gamma function. On dimensional grounds, E_α must be proportional to the ground state energy E_0 of the respective trap. For a harmonic trap with frequencies $(\omega_x, \omega_y, \omega_z)$ and a uniform trap with volume V, we find the following results:

	harmonic	uniform
	$\bar{\omega} = (\omega_x\omega_y\omega_z)^{1/3}$	$\bar{l} = (l_x l_y l_z)^{1/3} = V^{1/3}$
$\alpha =$	3	$3/2$
$\bar{E}_0 =$	$\hbar\bar{\omega}$	$\pi^2\hbar^2/(2m\bar{l}^2)$
$E_\alpha =$	$\bar{E}_0$	$(4/\pi)\bar{E}_0$

The thermodynamics of a Bose gas in the potential $U(\mathbf{r})$ can be described uniquely in terms of $g(\epsilon)$, temperature T and the chemical potential μ. In the case of a uniform system with constant volume, these reduce to the known variables (V, T, μ), suggesting the grand potential $\Omega(V, T, \mu)$ as a suitable starting point [25] for all thermodynamic calculations[3]. Within the semi-classical approximation, we can compute the total atom number N, energy E and grand potential Ω in terms of the chemical potential μ. Noticing that positive occupation numbers in Bose statistics imply $\mu \leq 0$, we find that the integral over the thermal occupancies of all excited states $N_{\mathrm{th}} \to N_c$ as $\mu \to 0_-$. Using the above notation, we find

$$N_c = \zeta(\alpha)\left(\frac{k_\mathrm{B}T}{E_\alpha}\right)^\alpha, \tag{2.5}$$

where $\zeta(\alpha) = \sum_{i=1}^\infty i^{-\alpha}$ is the Riemann zeta function. For $N > N_c$ the ground state occupation N_0 becomes macroscopic, and must be treated as an additive term to all our integrals - the particles in the ground state form a Bose-Einstein condensate.

---

[3](V, T, μ) are known as the natural variables of the thermodynamic potential Ω. The system is fully described by $\Omega(V, T, \mu)$, for example the energy can be expressed as $E = \frac{\mathrm{d}\Omega}{\mathrm{d}\beta}$.

Inverting the above equation, we can define the critical temperature T_c at fixed atom number as

$$k_\mathrm{B} T_c = \left(\frac{N}{\zeta(\alpha)} \right)^{1/\alpha} E_\alpha. \tag{2.6}$$

We define the dimensionless temperature τ by rescaling to the critical temperature (2.6):

$$\tau = \frac{T}{T_c}. \tag{2.7}$$

Another useful quantity is the *fugacity*

$$\mathcal{Z} = e^{\beta\mu}, \tag{2.8}$$

with $\beta = \frac{1}{k_\mathrm{B} T}$.

The entropy S can be calculated from Ω using $S = -\left. \frac{\mathrm{d}\Omega}{\mathrm{d}T} \right|_{V,\mu}$. It is easy to show that the contribution of the ground state atoms to Ω, E and S is negligible for all but the lowest temperatures ($T \ll T_c$). We can therefore set the ground state energy to 0. In Table 2.1, we summarize the results in the cases $T \leq T_c$, $T \geq T_c$ and $T \gg T_c$. Throughout this thesis, $g_\alpha(z) = \sum_{i=1}^{\infty} i^{-\alpha} z^i$ is the polylogarithm function, with $g_\alpha(0) = \zeta(\alpha)$. For $T \leq T_c$, we have $\mu = 0$ and thus $\mathcal{Z} = 1$. For $T \gg T_c$ we have $\mathcal{Z} \ll 1$ and we can approximate g_α with its truncated series.

Table 2.1: Important thermodynamic properties of a BEC in a general power-law trapping potential.

temperature	$\tau \leq 1$	$\tau \geq 1$	$\tau \gg 1$
fugacity	$\mathcal{Z} = 1$	$\mathcal{Z} < 1$	$\mathcal{Z} \ll 1$
$N =$	$N_c + N_0$	$\frac{g_\alpha(\mathcal{Z})}{\zeta(\alpha)} N_c$	$\frac{\mathcal{Z}}{\zeta(\alpha)} N_c$
$\frac{N_\mathrm{th}}{N} =$	τ^α	1	1
$\frac{\Omega}{k_\mathrm{B} T} =$	$-\frac{\zeta(\alpha+1)}{\zeta(\alpha)} N_\mathrm{th}$	$-\frac{g_{\alpha+1}(\mathcal{Z})}{g_\alpha(\mathcal{Z})} N$	$-N$
$\frac{E}{k_\mathrm{B} T} =$	$\alpha \frac{\zeta(\alpha+1)}{\zeta(\alpha)} N_\mathrm{th}$	$\alpha \frac{g_{\alpha+1}(\mathcal{Z})}{g_\alpha(\mathcal{Z})} N$	αN
$\frac{S}{k_\mathrm{B}} =$	$(\alpha+1) \frac{\zeta(\alpha+1)}{\zeta(\alpha)} N_\mathrm{th}$	$\left[(\alpha+1) \frac{g_{\alpha+1}(\mathcal{Z})}{g_\alpha(\mathcal{Z})} - \ln(\mathcal{Z}) \right] N$	$\left[(\alpha+1) + \ln\left(\frac{\tau^\alpha}{\zeta(\alpha)} \right) \right] N$

It is worth noting that within the local density approximation (LDA), the peak thermal phase space density in the trap $\rho = n\lambda_T^3$, defined in terms of peak atom

density n and the thermal wavelength $\lambda_T = (2\pi\hbar^2/mk_BT)^{1/2}$, approaches its peak value of $\zeta(3/2) = 2.612$ for $\tau \to 1_+$. Since $\rho \propto n$, we can write

$$\rho = \zeta(3/2)\tau^{-\alpha}. \tag{2.9}$$

In the limit $\tau \gg 1$, this allows us to write the entropy S in terms of ρ only - we shall exploit this fact subsequently.

Chapter 3

The Testbed: a Single-Chamber Ultracold Atom Experiment

The aim of this Chapter is to provide an overview of the design and construction of the apparatus [19] that formed the backbone of all experiments described in this Thesis. The system was initially built for training and was used in the early cooling experiments in our group [26–28]. This was to form the seed for a new, independent BEC experiment. While re-using an existing design promised to shorten the construction time, we were hoping to create a machine that would offer the performance and flexibility sufficient for a variety of proof-of-principle studies. Specifically, building on the existing design, we were hoping to optimize it to achieve most of the following:

- robust performance

- high atom numbers in a harmonic BEC

- high repitition rates

- easy optical access for future experiments

- space for additional coils, optics etc.

As proven by the various experiments described in subsequent Chapters, the system fulfilled all of these criteria. During my PhD, the original "donor" vacuum system had to be disassembled, cleaned, reassembled and baked. The new laser system went through several iterations before becoming fully operational, and the magnetic coil arrangement evolved in accordance with our experimental needs. We further chose to implement a hybrid magnetic-optical trap introduced by Lin *et al.* [29], in

which we were able to reliably produce quasi-pure BECs of $> 3 \times 10^5$ atoms with a repetition of over $1/30\,\mathrm{s}^{-1}$. This is comparable to or exceeds most multi-chamber ^{87}Rb setups. Efficient production of harmonic BECs provides an indispensable tool for further studies described in this Thesis. Nonetheless, considering the low cost, simplicity and excellent optical access of the system described in this Chapter, we feel that it warrants some interest in its own right. Our implementation will be of interest to groups wanting to design simple and cost-efficient BEC machines for various applications

Below, we describe the design considerations that guided the construction of the system, explain the BEC production sequence and quantify its performance at various stages.

3.1 The vacuum system

3.1.1 General considerations

Ultra-cold atom experiments typically require an ultra-high vacuum (UHV) environment. The atomic sample of relatively high density n is confined to a certain region of the vacuum chamber using a variety of techniques. Outside this region, UHV conditions prevail, and the background gas has a much lower density $n_{\mathrm{bg}} \ll n$. This is necessary because scattering and heating due to (two-body) collisions with the background gas limit any experiment to a timescale of the order $\tau_{\mathrm{bg}} = \Gamma_{\mathrm{bg}}^{-1}$, where Γ_{bg} is the corresponding collision rate [27]. Besides limiting the time available for conducting any useful experiments, τ_{bg} first and foremost determines the feasibility of creating a degenerate sample in thermal equilibrium. In fact, as we shall see below (see 3.5), the timescale for thermal equilibration, $\tau_{\mathrm{eq}} = \Gamma_{\mathrm{eq}}^{-1}$, is the lower bound on the time needed to cool any sample evaporatively. The simple timescale argument suggests that the collision rates in our experiment must satisfy

$$\tau_{\mathrm{bg}} \gtrsim \tau_{\mathrm{eq}}, \tag{3.1}$$

$$\text{or, equivalently, } \Gamma_{\mathrm{bg}} \lesssim \Gamma_{\mathrm{eq}}. \tag{3.2}$$

Note that for simplicity we consider two-body collisions only. The collision rates for two- and three-body processes scale as n and n^2, respectively, meaning that the two-body rate dominates for all but the highest densities in our experiments ($\sim 10^1 4\,\mathrm{cm}^{-3}$; see e.g. [30] and references therein). Then, assuming the mean velocities of the trapped and background atoms are $\bar{v}$ and $\bar{v}_{\mathrm{bg}}$, respectively, and with σ being

the typical collision cross-section, we find:

$$\Gamma_{\mathrm{bg}} \sim \sigma n_{\mathrm{bg}} \bar{v}_{\mathrm{bg}}, \tag{3.3}$$

$$\Gamma_{\mathrm{eq}} \sim \sigma n \bar{v}. \tag{3.4}$$

Strictly speaking, the applicable value for σ depends on the relative velocity, but we shall neglect the fact for an order-of-magnitude estimate. Typical values will range from the high-temperature hard-ball limit, $4\pi r^2$ (r being the atomic radius), to the low-temperature scattering cross-section $8\pi a^2$ (a being the effective scattering length), but the difference is irrelevant for the argument presented here. Now, assuming our sample is at a temperature T, while the background gas has $T_{\mathrm{bg}} \approx 300\,\mathrm{K}$, and remembering that $\bar{v} \propto \sqrt{T}$, we can re-write (3.2) as

$$n_{\mathrm{bg}} \lesssim n\sqrt{T_{\mathrm{bg}}/T}. \tag{3.5}$$

Consider we want to crate a uniform BEC of $N = 10^5$ atoms at $T = 30\,\mathrm{nK}$ in a box with volume $V = 30 \times 30 \times 30\,\mu\mathrm{m}^3$. The atom density in the trap is $n = N/V = 4 \times 10^{12}\,\mathrm{cm}^{-3}$, the temperature ratio is $T_{\mathrm{bg}}/T = 10^{10}$, and (3.5) requires $n_{\mathrm{bg}} \lesssim 10^{-5}n$, corresponding to a background pressure

$$p_{\mathrm{bg}} = n_{\mathrm{bg}} k_{\mathrm{B}} T \lesssim 1.5 \times 10^{-9}\,\mathrm{mbar}.$$

It has to be remembered that this is an absolute *upper bound* on p_{bg}, while typical pressures will be in the region of $10^{-11}\,\mathrm{mbar}$. During the early cooling stages, n is typically much smaller than the value assumed above.

τ_{bg} can be easily identified as the $1/e$ lifetime of a trapped sample: assuming atoms are predominantly lost via two-body collisions with the background gas, the in-trap atom number will evolve according to

$$\dot{N} = -\frac{1}{\tau_{\mathrm{bg}}}N = -c_1 n_{\mathrm{bg}} N. \tag{3.6}$$

Measuring τ_{bg} gives us a simple way to quantify the background pressure in the immediate vicinity of the cold atomic cloud, without resorting to expensive gauges.

3.1.2 Sources of ^{87}Rb atoms

At this point, it might seem that our aim is to reduce the background pressure as far as possible. However, loading atoms into the trap imposes contradicting requirements. The starting point of most cooling sequences is loading the atoms into a magneto-optical trap (MOT, see 3.4). This can be achieved in one of several ways:

- using a chirped [31] or Zeeman [32] slower

- from a 2D MOT [33, 34]

- directly from the background gas, as described here.

The last option was chosen in our setup because of its proven simplicity and reliability. It relies on a the background pressure of ^{87}Rb in the chamber to load the MOT. The loading rate depends only on the MOT geometry and is proportional to the background density of ^{87}Rb, n_{Rb}. Releasing ^{87}Rb into the chamber increases the background gas density, which we now write as $n_{\mathrm{bg}} = n_{\mathrm{bg,0}} + n_{\mathrm{Rb}}$. We can now write the rate equation similar to (3.7) for the atom number in the MOT:

$$\dot{N} = -c_1(n_{\mathrm{bg,0}} + n_{\mathrm{Rb}})N + c_2 n_{\mathrm{Rb}}. \tag{3.7}$$

Setting $N(0) = 0$, we find the solution has the form

$$N(t) = N_{\mathrm{max}} \left(1 - \exp(-t/\tau_{\mathrm{MOT}})\right), \tag{3.8}$$

$$\tau_{\mathrm{MOT}}^{-1} = c_1(n_{\mathrm{bg,0}} + n_{\mathrm{Rb}}) = c_1 n_{\mathrm{bg}} = \tau_{\mathrm{bg}}^{-1}, \tag{3.9}$$

$$N_{\mathrm{max}} = \frac{c_2}{c_1} \frac{n_{\mathrm{Rb}}}{n_{\mathrm{bg,0}} + n_{\mathrm{Rb}}}. \tag{3.10}$$

The two noteworthy features of this solution are:

- first, the $1/e$ MOT loading time τ_{MOT} is identical to the lifetime of a trapped sample τ_{bg}, and both *decrease* with n_{Rb}

- second, the maximum MOT loading N_{max} *increases* with n_{Rb} until $n_{\mathrm{Rb}} \gg n_{\mathrm{bg,0}}$

We see that, while reducing the density of contaminants $n_{\mathrm{bg,0}}$ remains beneficial, the required background ^{87}Rb density is determined by balancing the benefits of increasing the atom number in the MOT against the decrease in lifetime. The resulting limitations on trapping time can be circumvented in a two-chamber experiment, where the MOT chamber is kept at a higher background pressure than the "science chamber" by differential pumping, and the atoms are transferred between the two spatially separated regions by using suitable moving trapping potentials. The improved lifetime generally comes at the cost of increased complexity and reduced repetition rate. In our experiments, we followed a different approach: building on the group's previous experience with a single-chamber setup, we were hoping to optimize the background pressure (as well as the later stages of the BEC production sequence) in order to achieve excellent performance within the limitations of our

vacuum topology. Further, our system provides sufficient optical access for complex experiments.

The choice of atomic sources affects the performance of a single-chamber ^{87}Rb system markedly. This is because the natural abundance of ^{87}Rb is only 28%. When using an atom source with the natural isotope ratio, the remaining 72% of ^{85}Rb will contribute to $n_{\text{bg},0}$, but *not* to n_{Rb} in (3.9) and (3.10). A simple estimate using the above model shows that, the background pressure and thus the lifetime τ_{bg} being equal, the achievable MOT loading scales directly as the relative abundance of the trappable isotope. By using a source of isotopically pure ^{87}Rb, we can theoretically achieve a 3.6-fold enhancement in the MOT loading. We shall see that this translates into even greater gains later in the evaporation sequence.

3.1.3 Assembly and performance

The original single-chamber vacuum system, developed for the early proof-of-principle experiments in our group [26–28], allowed us to cool atoms in a magneto-optical trap [35]. However, the system used vapour sources of Rb in its natural isotope mixture, and the measured lifetimes in a magnetic trap did not exceed 3.5 s. It was thus decided to rebuild the system, with particular care given to cleaning, baking and eliminating potential sources of leaks and contaminations.

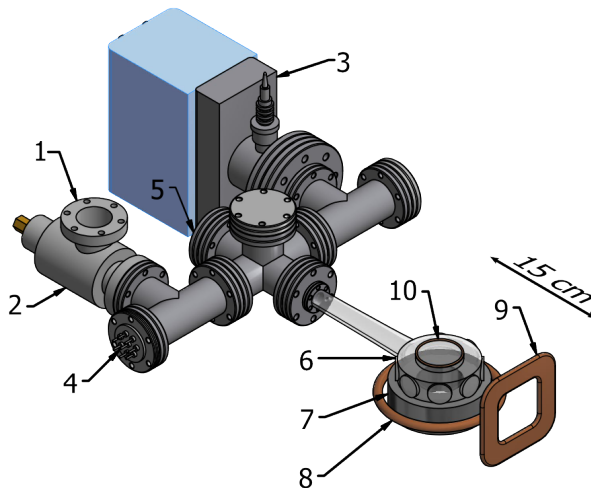**Figure 3.1:** Single-chamber vacuum system: 1 - turbo pump port, 2 - valve, 3 - ion pump, 4 - ^{87}Rb dispensers, 5 - viewport, 6 - glass cell. We also show the magnetic coils for creating: 7 - quadrupole field, 8 - bias field, 9 - guide field, 10 - RF field. All coils except 9 and 10 are paired (only one coil per pair is shown).

The layout of the vacuum system is shown in Fig. 3.1. The system is constructed

from standard vacuum components, with the exception of a pyrex cell by Triad Technology [36] which allows optical access via two 50 mm (top and bottom), seven 25 mm anti-reflection-coated windows and the 25 mm vacuum tube. The system uses standard CF flanges with copper gaskets. In day-to-day operation, the vacuum is maintained by a single 45 l/s ion pump (Oerlikon IZ50 [37]). Additional high-volume pumps (a turbo pump backed by a scroll pump), used during the bake-out only, are separated by an UHV all-metal angle valve (Series 540, DN40 by VAT Vacuum [38]). For the atomic sources, we installed 98% enriched ^{87}Rb atomic vapour sources (AS-3-Rb87(98%)-50-V from Alvatec [39]).

All components were cleaned in several stages:

1. mechanical cleaning with a scouring pad (steel parts only)

2. ultrasonic cleaning in an acetone bath (steel parts only)

3. rinsing with isopropanol

4. rinsing with water

5. rinsing with methanol

After assembly, the system was baked at 200 °C for one week. The temperature gradients across the system, as well as the heating and cooling rates, were monitored using multiple thermocouples and held within the manufacturer specified limits for the respective components.

Pure ^{87}Rb is released into the system by applying a heating current to the atomic vapour source. Initially, the walls of the vacuum system adsorb most of the atoms, making it impossible to maintain a high enough pressure in the MOT region. Once the surfaces saturate, the atoms are predominantly removed by the ion pump, and a near-constant pressure can be maintained by activating the ^{87}Rb sources daily[1] to match the average loss rate. The released quantity is controlled by the duration and magnitude of the applied current.

We achieved magnetic trap lifetimes of over 20 s, corresponding to a background pressure of $\sim 2 \times 10^{-11}$ mbar. Under typical experimental conditions, we increase the background pressure to improve the MOT loading, reducing τ_{bg} to about 10 s.

---

[1]The flow rates in our system are on the order of $0.1\,h^{-1}$, making more frequent adjustments unnecessary

3.2   Magnetic field coils

The magnetic quadrupole field for both the MOT and the magnetic trap is created by an anti-Helmholtz pair of 16-turn water-cooled coils wound from 4 mm copper tubing ("7" in Fig. 3.1). These create an axial gradient of $B' = 400\,\mathrm{G/cm}$ when carrying 200 A.

The quantisation axis for optical pumping is provided by a magnetic field along the imaging axis. We use a low-inductance planar 10 turn coil wound from 5 mm copper wire ("9" in Fig. 3.1), providing a field of 5 G at the atoms.

Gravity compensation during long-time-of-flight (ToF) measurements is achieved by combining a quadrupole field (created by the MOT coils) with a homogeneous vertical bias field. Residual potential curvature is minimized by a high bias field strength. We use two 50-turn coils in a Helmholtz configuration ("8" in Fig. 3.1), providing a bias field of 70 G when run at 10 A.

A radio-frequency (RF) field for forced evaporative cooling is created by a three-turn coil mounted against the top viewport of the cell. For transitions between neighbouring m_F states separated by up to 15 MHz, we achieve Rabi frequencies above 20 kHz using 600 mW of RF power.

3.3   Laser system for BEC experiments

3.3.1   Atomic level structure of ^{87}Rb

Alkali atoms have long been favoured for atomic physics experiments due to their simple and well-understood electronic level structure. Since they only possess one electron in the outermost shell, their excitations at low energies are described extremely well by the single active electron approximation. Due to LS-coupling [41], ^{87}Rb exhibits a fine-structure doublet, comprising the D1 line ($5^2\mathrm{S}_{1/2} \rightarrow 5^2\mathrm{P}_{1/2}$) at 795 nm and the D2 line ($5^2\mathrm{S}_{1/2} \rightarrow 5^2\mathrm{P}_{3/2}$) at 780 nm [40]. These are well separated, and in our experiments we only use the D2 line. The total electron angular momentum $\mathbf{J} = \mathbf{L} + \mathbf{S}$ further couples to the nuclear angular momentum $\mathbf{I} = 3/2$, leading to the hyperfine splitting of the ground state into the $F = 1$ and $F = 2$ states. The D2 excited states is split into the $F' = 0, 1, 2, 3$ hyperfine states. The resulting level structure is shown in Fig. 3.2. The transition between stretched states $F = 2 \rightarrow F' = 3$ provides an essentially closed two-level system, which we can utilize for laser cooling and trapping. Still, spontaneous decay into the $F = 1$
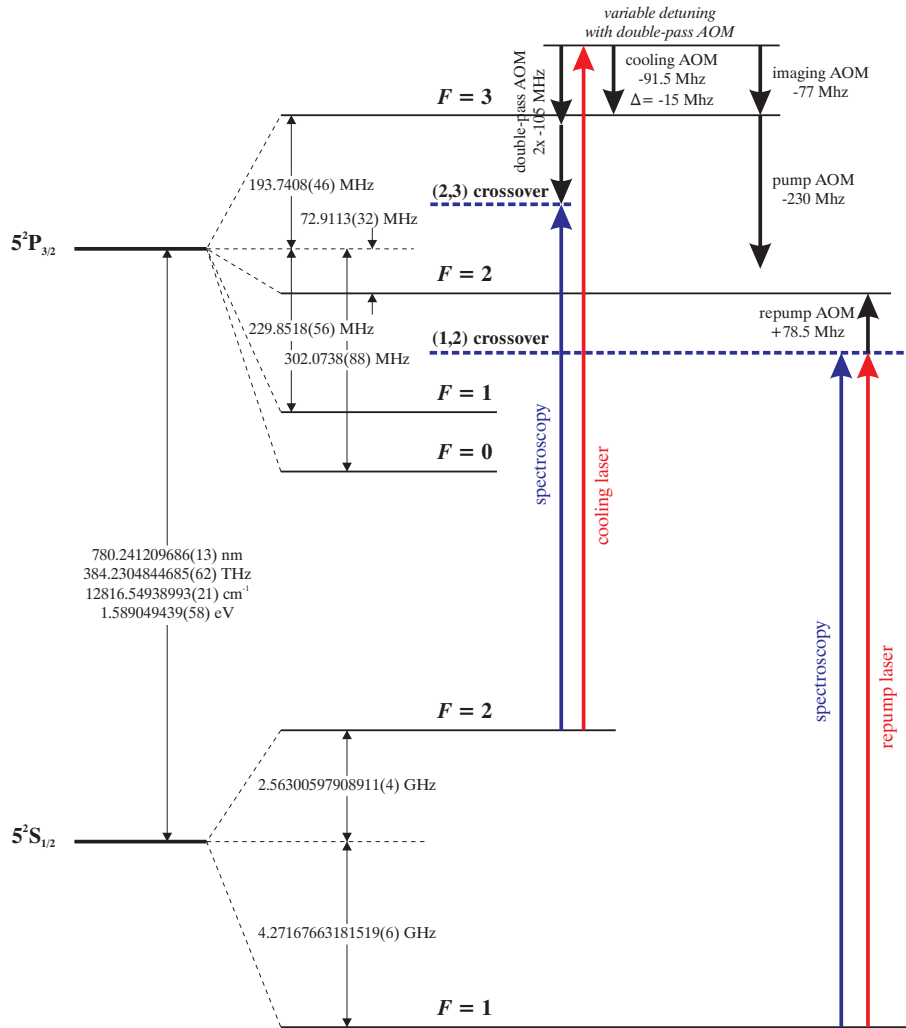
Figure 3.2: ^{87}Rb D2 line structure (reproduced from [40], showing laser frequencies, transitions used for locking and AOM-induced shifts (see text for details).

ground state is possible via higher-order transitions, and any atom in this state is permanently lost from the cooling process. To counteract population growth in this dark state, a second laser beam (the repump beam) is used to pump atoms from the $F = 1$ to the $F' = 2$ (or any other excited) state. These atoms can then return to the cooling cycle via spontaneous decay.

Besides laser cooling, we also use resonant light to pump the atoms into the magnetically trappable Zeeman states via the $F = 2, m_F \rightarrow F' = 2, m_{F'} = m_F + 1$ transition, as well as to implement absorption imaging on the $F = 2 \rightarrow F' = 3$ line. This means our laser system must produce four different laser frequencies, each stable to a few 100s kHz while tunable over many MHz, as summarized in Table 3.1.

Table 3.1: Laser frequencies for the ^{87}Rb BEC experiment. Note that pumping and imaging detunings refer to Zeeman-shifted lines.

beam	transition	detuning Δ (MHz)	power (mW)
cooling	$F = 2 \rightarrow F' = 3$	-15..-70	~ 100
imaging	$F = 2 \rightarrow F' = 3$	0	~ 100
pumping	$F = 2 \rightarrow F' = 2$	0	~ 10
repump	$F = 1 \rightarrow F' = 3$	0	~ 10

3.3.2 Laser system for cooling and trapping

All the required frequencies are derived from external-cavity diode lasers (ECDLs) [42–47]. These offer a good balance of stability, cost, linewidth, and tunability. Many designs are available, and we have experimented with several home-built as well as commercial products. The operating principles, design and performance of ECDLs are described in Appendix A. We eventually settled for a commercial model (DLpro from Toptica [48]). The necessary stability is achieved by locking each ECDL to an atomic line of ^{87}Rb using saturation absorption spectroscopy [49]. We describe the locking technique in detail in Appendix B; here, it suffices to say that the technique allows us to stabilize the laser frequency to that of any of the dipole-allowed transitions within the D2 line, but also to the so-called cross-over frequencies. The cross-over frequency is the mean of the frequencies of two transitions sharing the same ground state. Stabilizing an ECDL to a cross-over peak is often easier due to a stronger spectroscopic feature (see Appendix B for details). Acousto-optic modulators (AOMs) can be used to change a laser frequency by up to a few 100 MHz, allowing us to derive frequencies within this range of the locking frequency. However, using AOMs to bridge the hyperfine splitting of the $5^2\mathrm{S}_{1/2}$ ground state (6.8 GHz) requires complicated multi-pass setups that suffer from power losses. We therefore use two separate laser sources: one for repump and and one for cooling, imaging and optical pumping.

The locking and AOM configuration we use is shown in Fig. 3.2. The red arrows indicate ECDL frequencies, the black arrows indicate AOM-induced shifts, and the blue arrows indicate the reference frequency used for locking. The dashed blue lines indicate cross-over frequencies. The optical layout implementing this scheme is shown in Fig. 3.3.

The part of cooling light used for spectroscopy is frequency-shifted using a

double-pass AOM. The AOM is placed between two focusing lenses, such that the minus-first order is always retroreflected back through the AOM, experiencing the same negative frequency shift (~ 105 MHz) twice. The laser is locked to the $F = 2 \rightarrow F' = (2,3)$ cross-over peak, meaning that the laser frequency in the main output is ca. 210 MHz higher than the cross-over frequency. The double-pass AOM remains aligned for any frequency shift and can thus be used for easy frequency tuning. Up to 50 mW of the available output power are used to seed a tapered amplifier (BoosTA from Toptica [48]), providing up to 1.5 W of output power. Imaging and pump beams are derived from the amplifier's output using a beam splitter and two AOMs (see Fig. 3.2) and recombined using a polarizing beam splitter. A final AOM after the tapered amplifier is used to reach the cooling frequency.

Each of the output beams passes through a shutter. This serves several purposes: it enables us to keep the AOM at operating temperature while the beam is shut, thus improving power stability, and eliminates any light diffracted due to stray radio-frequency signals from the AOM driver. AOMs can still be used for precise timing and allow a much faster switching time compared to mechanical shutters.
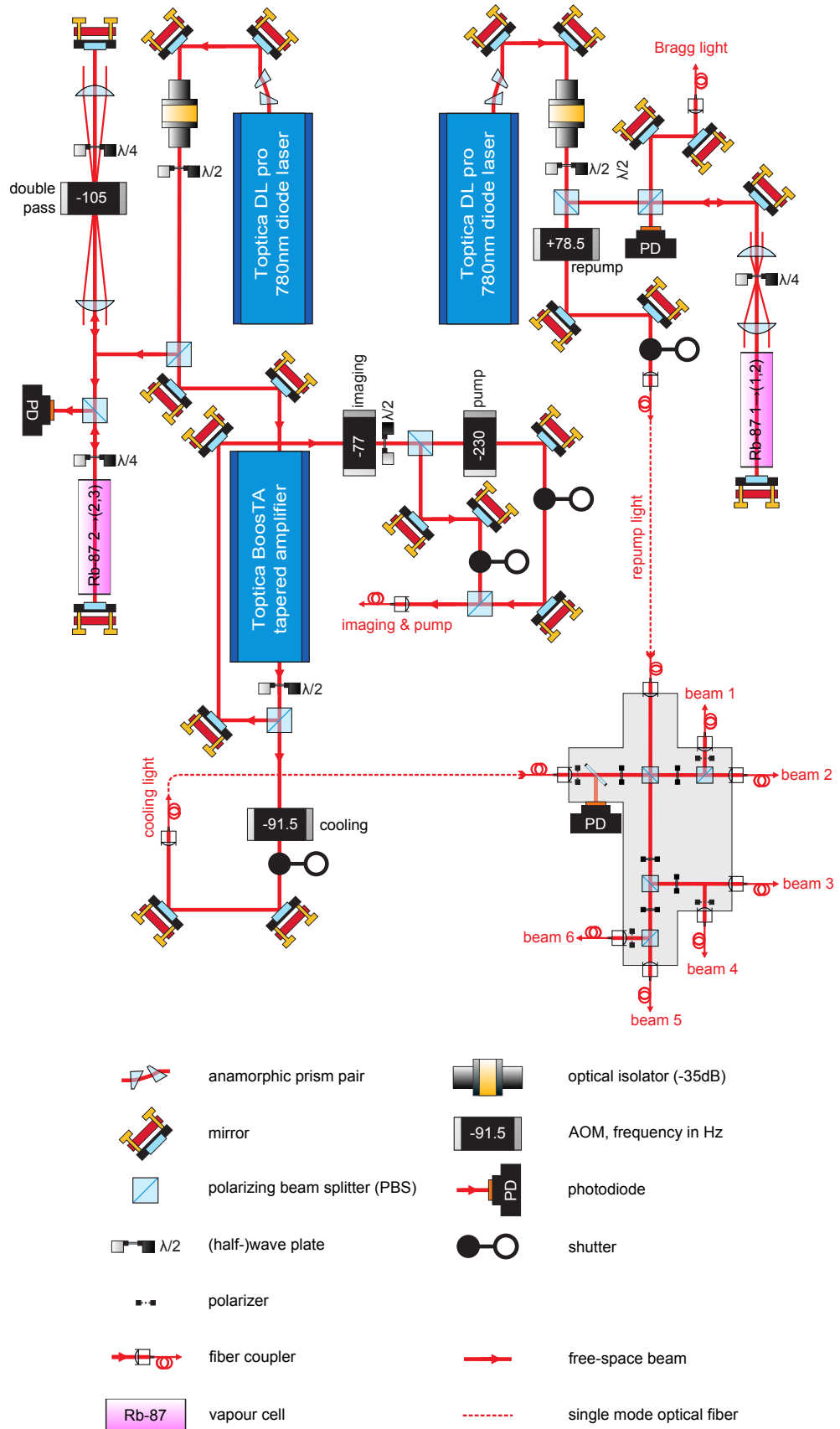
Figure 3.3: Layout of the laser system

3.3.3 Fiber optics and beam delivery

Polarization-maintaining single-mode optical fibers (PM630-HP with APC couplers from Thorlabs [50]) are used to guide beams to the BEC setup. The cooling and repump beams are delivered to the eight-way fiber port cluster shown in Fig. 3.3 and Fig. 3.4. This is used to combine cooling and repump light and split it 6-way for the MOT beams. The fiber coupling efficiency is determined by the overlap between the free-space laser mode and the eigenmode of the fiber. Assuming the free-space beam is collimated and the fiber tip is exactly in focus of the collimation lens, the maximum efficiency achievable when coupling an elliptic Gaussian beam with waists w_x and w_y into a fiber with a mode field diameter (MFD) of $2w_f$ is

$$C = \frac{4w_f^2 w_x w_y}{(w_x^2 + w_f^2)(w_y^2 + w_f^2)}, \tag{3.11}$$

with a maximum at $w_f = \sqrt{w_x w_y}$. One can see that the maximum coupling efficiency $C_{\max} = 4w_x w_y/(w_x + w_y)^2$ depends weakly on the beam ellipticity, only dropping to 89% for a 2:1 beam. Beam shaping is therefore secondary, as long as we choose the appropriate lens and collimate the beams well. We achieved good results using an aspheric lens mounted on a micrometre translation stage for precise collimation, and two steering mirrors providing decoupled degrees of freedom for spatial alignment. In practice, we achieve a free-space-to-fiber coupling efficiency of at least 45% at every stage. About 20% of the available cooling light power is therefore delivered to the MOT.
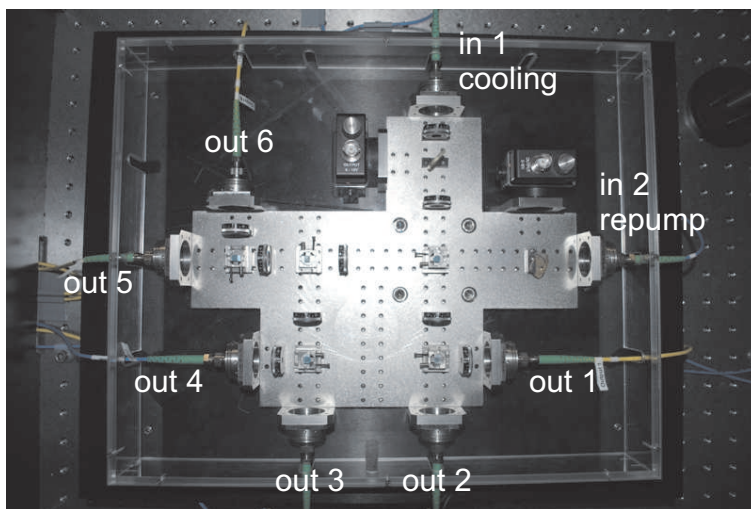
Figure 3.4: Fiber port cluster used for beam splitting

Similarly, imaging and pump beams are coupled into polarization-maintaining

fibers and delivered to the MOT setup. Fig. 3.5 shows the arrangement of MOT, imaging and pumping beams relative to the vacuum system.
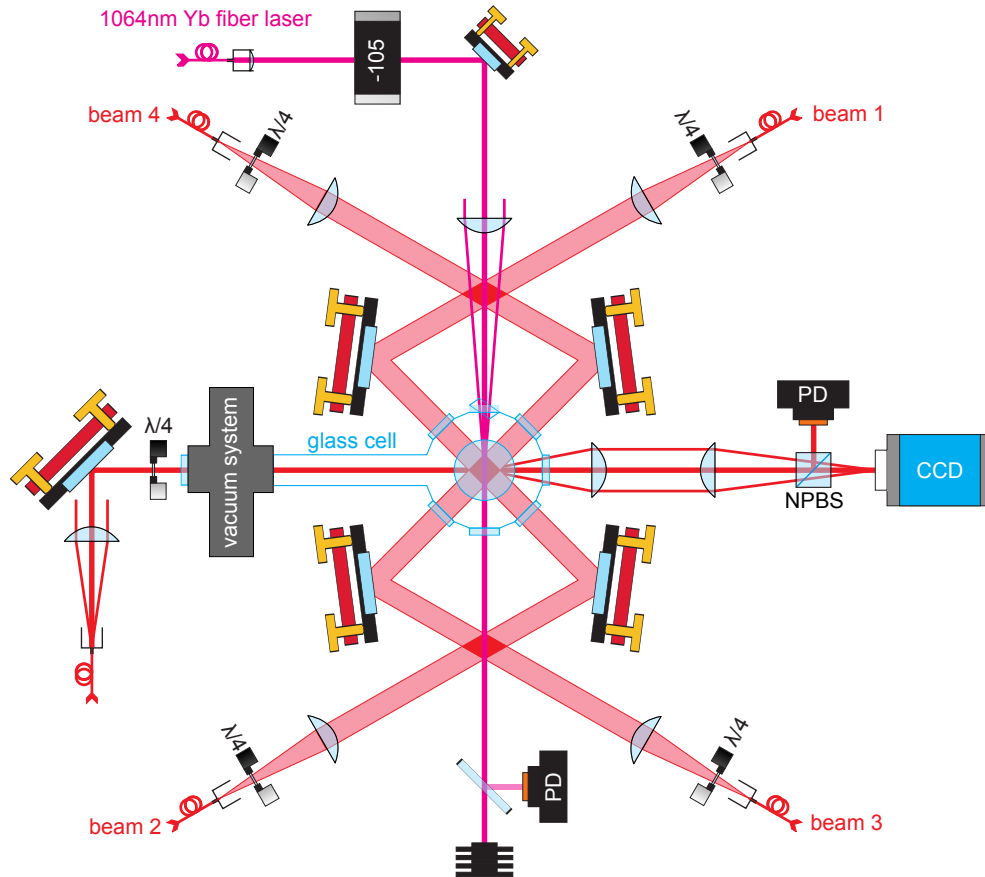
Figure 3.5: Optical layout of the single chamber system, showing four of the six MOT beams (1-4), the optical path for the imaging and pump beams (left to right) and the ODT beam (top to bottom).

The MOT beams, as well as the pump and imaging beams, are collimated to the maximum size permitted by the science cell's 1" windows, simplifying alignment of the MOT. All beams are circularly polarized using quarter-wave plates. The choice of polarizations is explained below.

3.3.4 Dipole trap beam

Figure 3.5 also shows the optical-dipole-trap (ODT) beam used for the hybrid trap. It is derived from a 20 W ytterbium fiber laser (YLR-20-LP from IPG Photonics). After passing through an AOM, the beam is focused by a concave-convex pair of lenses, allowing the adjustment of both waist size and position. We typically use a beam waist of $65\,\mu$m and a maximum power of 5 W at the atoms. Higher powers

lead to excessive atom losses, which can be attributed to two-photon transitions [51]; these transitions are caused by the large linewidth of the trapping laser (1.8 nm in our case). The focal point is positioned between one and two beam waists below the zero of the magnetic quadrupole field. The beam power is controlled in the range $0.01 - 5$ W using a feedback loop consisting of a photodiode, a proportional-integral-derivative (PID) controller, and the AOM. Throughout this range, we achieve an root-mean-square (rms) power noise below 1 mW over a bandwidth of 1 kHz.

3.3.5 Computer control

The experiment is controlled using a system of PXI-compatible output boards from National Instruments [52]. The current system consists of a PXIe-1082 chassis holding two PXI-6536 digital output cards, and a PXI-6713 and PXI-6733 analog output cards. Each digital card provides 32 TTL-compatible channels, and each analog card provides 8 outputs. The digital channels are individually isolated using optocouplers. The high coil current can be switched using an IGBT driver, and its strength is controlled via an analog input of the power supply. Laser beams can be switched and detuned using digital and analogue signals, respectively. The outputs are programmed using Cicero software by Aviv Keshet using NI DAQmx drivers. All outputs are synchronized by distributing a common clock signal between the PXI cards. One of the digital outputs is used to provide trigger signals for the imaging camera. Images recorded by the CCD camera are read out and processed using a LabView program written by Tobias Schmidutz, and further image analysis is explained subsequently.

3.4 Magneto-optical trapping and laser cooling

3.4.1 Theoretical foundations

The principle of magneto-optical trapping is to combine laser cooling by six pairwise counter-propagating red-detuned beams with a quadrupole field to provide confinement in both momentum space and real space [41,53]. Consider the beam and field configuration shown in Fig. 3.6 (a) below.

We will restrict our discussion to a model atom having a ground state with total angular momentum $F = 0$ and an excited state with $F = 1$. In an external field, the upper level will thus be Zeeman-split into the $m_F = -1, 0, +1$ states, as shown
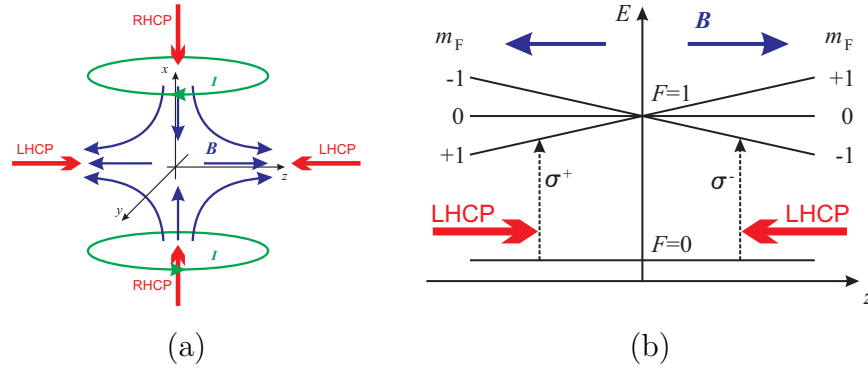
Figure 3.6: Magneto-optical trapping: (a) field orientation and corresponding beam polarizations (y beams not shown); (b) operating principle

in Fig. 3.6 (b). The combination of the fields and beam polarizations chosen ensures that the *left*-hand circularly polarized (LHCP) beam propagating in the *positive z* direction drives the $|0, 0\rangle \to |1, 1\rangle$ (σ^+) transition, which is closer to resonance for $z < 0$, where B points in the *negative z* direction, and vice versa. The cooling and confinement is easily seen by considering the time-averaged force acting on the atom due to each of the two counter-propagating beams along z [53]:

$$F_\pm = \pm\frac{\hbar k \Gamma}{2}\frac{S}{1 + S + (2\delta_\pm/\Gamma)^2}, \tag{3.12}$$

where k is the wavenumber, Γ is the natural linewidth of the transition, $S = I/I_{\text{sat}}$ is the ratio of beam intensity I to saturation intensity $I_{\text{sat}} = \frac{2\pi^2}{3}\frac{\hbar\Gamma c}{\lambda^3}$, and δ is the effective detuning as seen by the atom. The latter is affected by three factors: the detuning of the laser δ_0, the Doppler shift due to the atom's velocity $\mp kv$, and the Zeeman shift due to the quadrupole field $\mp g_F \mu_B B'z/\hbar = \mp\alpha z$. The resultant force is

$$F = F_+ + F_- \tag{3.13}$$

$$= \frac{\hbar k \Gamma S}{2}\left[\frac{1}{1 + S + \left(2\frac{\delta_0 - kv - \alpha z}{\Gamma}\right)^2} - \frac{1}{1 + S + \left(2\frac{\delta_0 + kv + \alpha z}{\Gamma}\right)^2}\right] \tag{3.14}$$

$$\approx -(kv + \alpha z)\frac{8\hbar k S(-\delta_0)}{\gamma\left[1 + S + \left(\frac{2\delta_0}{\Gamma}\right)^2\right]^2}. \tag{3.15}$$

In 3.15 we assumed $kv \ll |\delta_0|$, $\alpha z \ll |\delta_0|$. This shows that the force is approximately linear in v and z, and will provide both confinement and cooling for red (negative) detuning. Cooling is achieved by damping the motion of individual atoms. More generally, the cooling region (MOT volume) will be limited to $\alpha z \lesssim |\delta_0|$, and the

37

maximum initial velocity (and thus temperature) of atoms that can be cooled will be limited to $kv \lesssim |\delta_0|$.

3.4.2 Doppler limit and sub-Doppler cooling

The temperature achievable in a magneto-optical trap is limited to what is known as the Doppler limit, T_{D}. The limit arises due to the stochastic nature of photon re-emission by the atoms, resulting in heating [54]. The cooling effect is balanced by stochastic heating at a temperature

$$k_B T_{\mathrm{D}} = \frac{\hbar \Gamma}{2}. \tag{3.16}$$

For ^{87}Rb, $\Gamma = 2\pi \times 6.1\,\mathrm{MHz}$ [40] and $T_{\mathrm{D}} \approx 150\,\mu\mathrm{K}$. However, it has been shown that multi-level atoms moving in a light field with spatially varying polarization can be cooled to temperatures below the Doppler limit [53, 55–57]. In the counterprop-agating beam configuration described above ($\sigma^+ - \sigma^-$), the atomic cloud will reach lower temperatures if the magnetic field gradient is turned off and the laser detuning is increased further. This cooling stage at the end of MOT loading is referred to as optical molasses [58]. The ultimate cooling limit withing the semiclassical theory of atom-light interaction (that is, treating the external degrees of freedom of the atom, as well as light, classically) is the recoil temperature T_{R} given by [56]

$$k_B T_{\mathrm{R}} = \frac{\hbar^2 k^2}{2m}. \tag{3.17}$$

For ^{87}Rb, the recoil limit is $T_{\mathrm{R}} \approx 0.2\,\mu\mathrm{K}$ - 3 orders of magnitude below the Doppler limit, leaving significant scope for optimizing the starting conditions before trans-ferring atoms from the MOT into a purely magnetic trap. It is worth noting that temperatures below T_{R} have also been achieved [59], and can be explained within the quantum atom-light model.

3.4.3 Experimental implementation

For the MOT we use an axial field gradient of $B' = 13\,\mathrm{G/cm}$ and a cooling-light detuning of $-25\,\mathrm{MHz}$. Typically, we load a MOT of 10^9 atoms in $15\,\mathrm{s}$, but $5\,\mathrm{s}$ is often sufficient to produce BECs with $> 10^5$ atoms. MOT atom numbers can be deduced using either absorption imaging or the intensity of fluorescence light collected on a photodiode. The latter is less accurate, with the signal deviating from a simple linear scaling for optically dense clouds. However, it is our preferred method as it can

be used for non-destructive in-sequence diagnostics, following the initial calibration using absorption imaging.

Following the initial loading stage, we compress the MOT by increasing B' to $64\,\text{G/cm}$ for $20\,\text{ms}$, and then detune the cooling light to $-68\,\text{MHz}$ for $1\,\text{ms}$ (CMOT, [60]). We found that these steps reduce the temperature and improve transfer into the magnetic trap. These steps are followed by $2\,\text{ms}$ of optical molasses, during which the magnetic field is switched off and the cooling-light detuning of $-68\,\text{MHz}$ is maintained. This cools the cloud to $\approx 15\,\mu\text{K}$ - well below the Doppler limit. Lower temperatures are possible, albeit at the expense of atom number.

3.5 Evaporative cooling

3.5.1 Theoretical basics

To overcome the fundamental limitations of optical cooling, a different mechanism is required. A commonly used method that leads to further reduction in T while increasing the cloud's phase-space density is evaporative cooling. The idea behind evaporative cooling is to allow the atoms carrying energy well above the thermal average to escape - which after rethermalization leads to a decrease in the temperature. This process can be repeated by gradually decreasing the trap depth. An analytical model proposed in [61] allows us to describe the evolution of all relevant quantities during evaporation by simple power laws. If we assume that atoms with energies above $\eta k_{\text{B}} T$ are allowed to escape from a trap with characteristic power α^2, we can show that these carry away $\gamma = \frac{\eta}{\alpha+3} - 1$ times the average thermal energy per atom. We then find that the relevant quantities scale as N^q during the evaporative cooling, with characteristic exponents q shown in Table 3.2 (note that [61] defines parameter $\xi \equiv \alpha + 3/2$).

Successful evaporation towards BEC requires an increase in the phase-space density ρ as N decreases, i.e. $q_\rho < 0$. Additionally, continuing evaporation requires a sufficiently fast thermalization rate, which is proportional to the collision rate κ. Runaway evaporation is possible if κ increases, requiring $q_\kappa < 0$. The range of η where efficient evaporation is possible depends on the trap shape. The conditions for runaway evaporation in different trapping potentials are shown in Table 3.3. We compare linear, harmonic and uniform trapping potentials ($s = 1, 2$ and ∞, respectively).

---

[2]As defined previously, $\alpha = 3/2 + 3/s$ for an r^s potential

Table 3.2: Scaling exponents during evaporative cooling; reproduced from [61]

variable	symbol	exponent q
atom number	N	1
temperature	T	γ
volume	V	$\gamma(\alpha - 3/2)$
density	n	$1 - \gamma(\alpha - 3/2)$
p.s.d.	$\rho = n\lambda_T^3$	$1 - \gamma\alpha$
collision rate	$\kappa = n\sigma\bar{v}$	$1 - \gamma(\alpha - 2)$

It can be seen that traps with higher s (and thus steeper walls) can generally achieve gains in phase space density at lower η, meaning faster experimental sequences. Large η will require slow evaporation, which must be balanced with atomic losses due to background collisions and thus finite in-trap lifetime. However, runaway evaporation is only possible for $s < 6$, excluding especially the case of the uniform trap[3]. Further, in Table 3.3 we show the characteristic exponents in different traps at fixed $\eta = 10$. It can be seen that, while ρ increases fastest in traps with larger s, κ (and n) shows the opposite trend. This in part justifies the use of a linear trap, i.e. a magnetic quadrupole trap, in the early stages of the evaporation sequence, where density is low.

Having discussed the basics, we now consider three possible implementations of traps suitable for evaporative cooling, before presenting the experimental details.

3.5.2 Magnetic trap with radio-frequecncy (rf) evaporation

A magnetic quadrupole field $\mathbf{B} = B'(x, -y/2, -z/2)^{\mathbf{T}}$ provides a convenient linear trap for atoms with a permanent magnetic moment $\mu_{\mathbf{B}}$. Consider the Zeeman energy $V = -\mu_{\mathbf{B}} \cdot \mathbf{B} = g_F\mu_B m_F B$, where F is the total angular momentum quantum number, m_F - its projection along the direction of $\mathbf{B}$, and g_F is the corresponding Landé g-factor. This potential will confine states with $g_F m_F > 0$. Considering hyperfine sub-levels of the $2S_{1/2}$ state of ^{87}Rb, we find that the trappable states are $F = 2$, $m_F = +1, +2$ and $F = 1$, $m_F = -1$. Removal of the most energetic atoms from the magnetic trap is achieved by selectively transferring these to untrapped

---

[3]Evaporation in a uniform trap will be discussed in Chapter 4.

Table 3.3: Comparison of evaporation conditions in common trap types.

Trap type:	linear	harmonic	uniform
α	9/2	3	3/2
p.s.d. gain ($q_\rho < 0$) for	$\eta > 5.5$	$\eta > 4$	$\eta > 2.5$
runaway evaporation ($q_\kappa < 0$) for	$\eta > 6.3$	$\eta > 6$	never
	Typical exponents for $\eta = 10$:		
N	1	1	1
T	1.2	2.3	5.7
V	3.7	3.5	0
n	-2.7	-2.5	1
ρ	-4.5	-6	-7.5
κ	-2.1	-1.3	3.8

states. The process is described in more detail in [62]. The underlying principle is as follows: the Zeeman splitting of the hyperfine states increases with B, and thus with distance from the centre of the trap, x. Choosing a radio frequency (rf) such that $hf_{\text{rf}} = \mu_B B(x)$ for some x will cause transitions to untrapped states in atoms energetic enough to reach the corresponding region of the trap, i.e. with energies $E > E_0 = g_F \mu_B m_F B(x)$. An atom starting in the $F = 2$, $m_F = 2$ state will be successively transferred to the states with the same F and $m_F = 1$, $m_F = 0$, etc. It can be seen that $E_0/(k_{\text{B}}T)$ will define the evaporation parameter γ. The value of γ, which in turn determines the evaporation rate, can thus be adjusted by changing f_{RF}.

The field direction is not constant inside the trap, and perfect trapping requires that $\mu_{\mathbf{B}}$ follows $\mathbf{B}$ adiabatically. The Larmor precession frequency must therefore be much higher than the trapping frequency. For sufficiently strong fields, this is the case everywhere except at the trap centre. The associated losses (Majorana spin-flip transitions) limit the cooling in magnetic quadrupole traps to a few μK. Magnetic traps without a zero have been used to avoid these Majorana losses [6, 7, 63]. An alternative is to use an optical trap [64].

3.5.3 Optical dipole trap (ODT)

Optical dipole forces of a red-detuned laser beam can be used to confine the atoms in the high-field region. Due to the AC Stark shift of the ground state energy, the atom experiences a potential of the form [41]

$$U_{\text{od}}(\mathbf{r}) = \frac{\hbar\Gamma}{8}\frac{\Gamma}{\delta}\frac{I(\mathbf{r})}{I_{\text{sat}}}, \tag{3.18}$$

where $I(\mathbf{r})$ is the intensity of the confining light field. For negative (red) detuning, atoms are thus attracted to regions of higher intensity. Multiple configurations with both red and blue detuned beams have been studied [65].

A single Gaussian beam propagating along z with the waist at focus w_0 creates a potential of the form

$$U(r, z) = U_0\left(\frac{w_0}{w(z)}\right)^2\exp\left(\frac{-2r^2}{w^2(z)}\right), \tag{3.19}$$

$$w(z) = w_0\sqrt{1 + (z/z_R)^2}, \tag{3.20}$$

$$z_R = \pi w_0^2/\lambda. \tag{3.21}$$

The beam waist w_0 determines the radial confinement, while the the Rayleigh length z_R determines the axial confinement. The potential near $(r, z) = (0, 0)$ is approximately harmonic, with trapping frequencies given by $\omega_r^2 = 4U_0/w_0^2$ and $\omega_z^2 = 2U_0/z_R^2$. Evaporation can be forced by reducing the trap depth U_0. However, in doing so we also reduce the trapping frequencies and thus *increase* the effective volume - the resulting correction to the scalings presented in Table 3.2 is effectively descibed by substituting $\alpha \to \alpha - 3/2$. Thus, our *harmonic* trap will only perform as well as a *uniform* one, with the effective volume remaining constant with temperature. As discussed above, this will rule out efficient run-away evaporation. While crossing two or more beams is possible to improve confinement, the unfavourable scaling remains as long as the evaporation is forced by a simple scaling of the overall optical power.

Various techniques have been used to improve evaporation efficiency in optical traps [64, 66–70]. A simple method combining a single-beam ODT with a magnetic quadrupole field to achieve efficient evaporations was proposed in [29]. It combines the benefits of optical and magnetic traps, and allows efficient evaporation to degeneracy. This hybrid trapping technique is described next.

3.5.4   Magneto-optical hybrid trap

The hybrid trap uses a single-beam ODT to confine the cloud radially. The weak axial confinement is enhanced by adding a magnetic quadrupole field, with the magnetic zero displaced vertically from the ODT axis. In our system the parameters are chosen as follows:

- quadrupole field gradient $B' = 14.8 \pm 0.1\,\mathrm{G/cm}$ (just below the gravity-compensating value of $15.3\,\mathrm{G/cm}$)

- ODT beam waist $w_0 = 65 \pm 5\,\mu\mathrm{m}$

- vertical distance from the magnetic zero to the ODT axis $z_0 = -60 \pm 5\,\mu\mathrm{m}$

The resulting geometry improves the scaling of the average trapping frequency with trap depth, as discussed in [29,70,71]. To emphasize this point, we plot the effective trapping frequency $\bar{f} = (f_x f_y f_z)^{1/3}$ versus trap depth U_0 in Fig. 3.7. Both are obtained from a numerical model of our hybrid potential. The range shown in

(a)   (b)
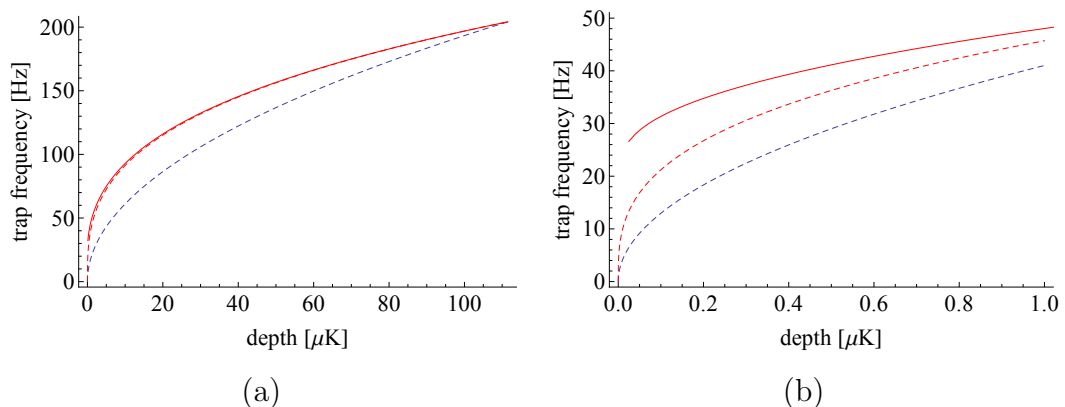
Figure 3.7: Effective trapping frequency versus trap depth in a hybrid trap. Solid red line: our hybrid trap; dashed blue line: a purely optical trap with equivalent starting conditions, $\bar{f} \propto U_0^{1/2}$; dashed red line: $\bar{f} \propto U_0^{1/3}$ (see text).

Fig. 3.7 (a) corresponds to optical power of the ODT beam of $0 - 5\,\mathrm{W}$, while panel (b) shows the detail for small powers of up to $60\,\mathrm{mW}$ (corresponding to trap depth below $1\,\mu\mathrm{K}$). We also show the evolution of the trapping frequency in a purely optical trap with equivalent starting conditions. As explained above, each of the three frequencies, and thus $\bar{f}$, scale as $U_0^{1/2}$ in a pure ODT. In the hybrid trap, the axial trapping frequency is determined by the quadrupole field, and thus remains nearly constant. This results in a scaling of the form $\bar{f} \propto U_0^{1/3}$ (dashed red line). For

large depths, this agrees well with the calculated frequency. The evaporation will thus be described by $\alpha = 2$, corresponding to $s = 6$ - the borderline case for runaway evaporation. At low ODT powers the scaling improves further - because we choose a magnetic field gradient that does not fully compensate gravity, the trap depth goes to 0 while the trapping frequencies remain non-zero, as seen in Fig. 3.7 (b). The behaviour thus approaches that of a (constant-$\bar{f}$) harmonic trap, making runaway evaporation possible. The performance of a hybrid trap is thus far superior to that of a gravity-compensated single-beam optical trap[4].

3.5.5 Experimental sequence

Following molasses, the atoms are optically pumped into the $|F, m_F\rangle = |2, 2\rangle$ hyperfine ground state, using a combination of resonant $|F = 2\rangle \rightarrow |F' = 2\rangle$ σ^+ light and repump light. We pump $> 80\%$ of the atoms into the $|2, 2\rangle$ state in $40\,\mu$s, while heating the cloud slightly, to $40\,\mu$K.

The atoms are then captured in a magnetic potential by suddenly turning on the quadrupole field with $B' = 64\,$G/cm[5] and then ramping B' to $80\,$G/cm over $200\,$ms. Finally, the trap is further compressed by raising B' to $200\,$G/cm over $500\,$ms.

From this point on, the evaporative cooling to condensation can be divided into three stages: (**I**) RF evaporation, (**II**) transfer into the hybrid trap, and (**III**) ODT evaporation.

Fig. 3.8 summarizes the evolution of the relevant experimental parameters during the evaporation sequence, while Fig. 3.9 displays the evolution of the atom number N, the temperature T, and the calculated phase-space density ρ.

N and T are measured using time-of-flight (ToF) absorption imaging (see 3.6) and ρ is calculated from a semi-classical model [29], using the analytic expression for the hybrid trapping potential. We verified the parameters of the model (such as beam waist) by measuring trapping frequencies and comparing them with theoretical predictions. We omit the calculated values of ρ in stage **II**, where they are unreliable because the trapping potential varies slowly over large volumes.

---

[4]A single-beam ODT performs better without gravity compensation, but it still lacks the axial confinement of our hybrid trap.

[5]By matching the gradient of the CMOT, we ensure that the captured cloud is close to the equilibrium density distribution of the new trapping potential. Any "mode mismatch" leads to heating as the cloud relaxes to its new equilibrium shape.
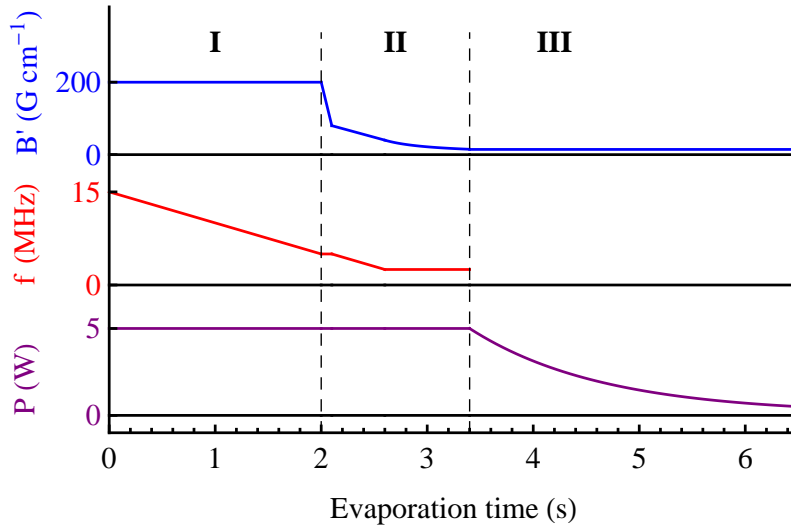
Figure 3.8: Evaporation sequence in the hybrid trap. We show the evolution of (top to bottom) the magnetic field gradient B', RF frequency f, and ODT power P. The sequence has three stages: (**I**) RF evaporation, (**II**) transfer into the hybrid trap, and (**III**) ODT evaporation.

RF Evaporation

During the initial evaporation stage in the compressed trap (**I** in Figs. 3.8 and 3.9), we ramp the RF frequency linearly from $15\,\text{MHz}$ to $5\,\text{MHz}$ in $2\,\text{s}$. We achieve a 30-fold increase in the peak phase space density, with an evaporation efficiency $q_\rho = \mathrm{d}[\ln \rho]/\mathrm{d}[\ln N] = -2.1$. According to 3.5.1, this corresponds to $\eta = 7.6$.

At the end of this stage the cloud typically contains $N = 50 \times 10^6$ atoms at $T = 90\,\mu\text{K}$.

Loading of the Hybrid Trap

In stage **II** the magnetic field gradient is decompressed to just below the gravity-compensating value, $B'_g = mg/\mu_B = 15.3\,\text{G/cm}$, where m is the atom mass, g is the gravitational acceleration and μ_B is the Bohr magneton. From this point on, the atoms are supported against gravity by optical forces only, while the confinement along the ODT axis is dominated by the magnetic forces [29]. Note that the ODT beam is on from the beginning of the magnetic trapping (see Fig. 3.8), but initially does not have a dominant role.

We decompress B' to $80\,\text{G/cm}$ over $100\,\text{ms}$ while keeping the RF frequency constant, then decompress further to $B'_1 = 40\,\text{G/cm}$ while sweeping the RF frequency linearly to $2.5\,\text{MHz}$ in $0.5\,\text{s}$; this provides a good gain in phase-space density de-
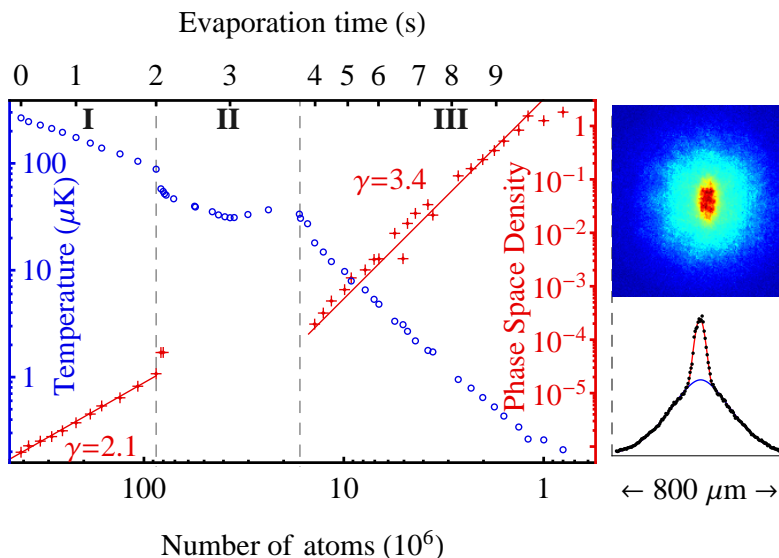
Figure 3.9: BEC production. We plot the temperature T (blue open circles, left axis) and phase-space density D (red crosses, right axis) versus atom number N (bottom) and time t (top) throughout the cooling sequence. See Fig. 3.8 and text for details of stages **I** - **III**. Also shown are an absorption image of a partially condensed cloud after 50 ms of time-of-flight expansion [optical density varies between 0 (blue) and 3 (red)] and its integrated profile. Fits to the thermal and condensed components are indicated.

spite the weak magnetic confinement. Finally, the magnetic field is decompressed from B_1' to $B_2' = 14.8$ G/cm. In this step we sweep the field gradient according to $B'(t) = B_1' \times (1 + t/\tau)^{-1}$, where $\tau = t_2 B_2'/(B_1' - B_2')$ and the sweep duration is $t_2 = 800$ ms. This changes the RF-limited trap depth approximately linearly with time, with the approximation being exact in the case of no ODT and $B_2' = B_g'$.

As the magnetic trap is decompressed, the cloud shape is distorted, making thermometry less accurate during this stage. Further, computing the peak phase-space density relies on integrating over all trapping volume, but convergence is very slow for gently sloping potential in the downwards direction below the magnetic zero. Thus, temperatures shown in Fig. 3.9 should be treated with caution, and ρ is not shown for this stage.

At the end of the loading stage, we typically have 20×10^6 atoms at $30\,\mu$K.

Optical Evaporation

For $B' < B'_g$, evaporation is no longer driven by the RF field. Instead, the trap depth is limited by the potential at the saddle point vertically below the magnetic-field zero [70]. Evaporation can be forced by lowering the ODT power P, albeit at the cost of reducing the trapping frequencies. However, our hybrid trap has 3 times the trapping frequency of an optical trap with the same starting depth and frequencies when approaching condensation. Moreover, unlike in a purely optical trap, the effective trapping frequency remains positive (in our case, near $30\,\mathrm{Hz}$) as the trap depth approaches zero, allowing efficient evaporation to very low temperatures.

We ramp P exponentially to its final value, P_end, with a time constant of $1.25\,\mathrm{s}$ and total ramp duration of $7\,\mathrm{s}$ (both parameters have been optimized empirically). We achieve an evaporation efficiency of $q_\rho = -3.4$, leading to condensation at $P_\mathrm{end} = 0.16\,\mathrm{W}$. Assuming the trap is harmonic with (nearly) constant frequencies in the late evaporation stages, we find $\eta = 7.4$ (see 3.5.1).

At the critical point, $N \approx 10^6$ and $T \approx 250\,\mathrm{nK}$. At this point, the trapping frequency is about 30 Hz along the ODT axis and about 90 Hz radially.

Lowering the ODT power further results in quasi-pure[6] condensates of $> 3 \times 10^5$ atoms. The lifetime of the quasi-pure BEC is $\sim 3\,\mathrm{s}$, consistent with the expected 3-body losses [72].

3.6 Imaging

All the thermodynamic properties of atomic clouds, i.e. the total atom number N, the condensate number N_0, and the temperature T, were extracted by recording and analyzing the density distribution of the atomic clouds, such as the one shown in Fig. 3.9. In studying BECs prepared in a harmonic trap, we typically record the optical density (OD) of a cloud after long time of flight (ToF) using absorption imaging [73]. More generally, we need a technique that would allow us to record clouds *in situ* as well as after variable ToF, meaning a wide range of ODs (typically 0-30). This can be achieved using high-intensity imaging [74], as explained below, and is a necessary prerequisite for studying BECs in box-like potentials.

As shown below, optical density can be interpreted as the line density of the atomic cloud. While N can be obtained from these by simple integration, extracting N_0 and T relies on an analytic model of the cloud (either *in situ* or in ToF). Below,

---

[6]we can only reliably detect thermal fractions down to about 30%

we review the well-known results for harmonically trapped clouds [73]. These will form the basis for developing corresponding results for clouds in power-law and uniform potentials in subsequent chapters.

To conclude this section, we will briefly review the practical side of image analysis. Again, we will built on these techniques in subsequent chapters.

3.6.1 Absorption imaging

Absorption of light with intensity I by the atomic cloud of density n can be described by the general Beer's law

$$\frac{\mathrm{d}I}{\mathrm{d}z} = -n\sigma(I)I, \tag{3.22}$$

with absorption cross-section $\sigma(I)$. For resonant light, we can write [74]

$$\sigma = \frac{\sigma_0}{c_\sigma} \frac{1}{1 + I/I_{\mathrm{sat}}}. \tag{3.23}$$

Here, σ_0 is the resonant absorption cross-section, c_σ accounts for any deviations from the ideal resonant cross-section due to polarization imperfections, and I_{sat} is the (effective) saturation intensity. In our experiment, we use circularly polarized light, and $\sigma_0 = 3\lambda^2/(2\pi)$.

In the low-intensity limit ($I \ll I_{\mathrm{sat}}$), we find that the column density $\tilde{n}$ can be calculated from the light intensity before and after the atoms (I_{i} and I_{f}, respectively) via

$$\tilde{n} = \int n(z)\mathrm{d}z = \sigma_0^{-1} \times \mathrm{OD} = \sigma_0^{-1} \left[-c_\sigma \ln\left(\frac{I_{\mathrm{f}}}{I_{\mathrm{i}}}\right) \right]. \tag{3.24}$$

Experimentally, the two intensities are obtained by recording the imaging beam on a CCD or CMOS sensor with and without the atoms (in our setup, we use a PCO Pixelfly CCD camera [75]). The maximum OD that can be recorded is limited by the signal-to-noise ratio in the I_{f}. Increasing the intensity I_{i} to counter (and decreasing the exposure time to keep the CCD from saturating) takes us into the mid- or high-intensity regime.

The choice of imaging intensity is dictated by the trade-off between the signal-to-noise ratio and the available dynamic range (and level quantization) of the detector. If we choose the intensity too high, the signal will be generally well above the noise floor, but the relative variations across the image will be small and eventually the error will be dominated by signal quantization. In practice, this means that for best results the (raw) optical density must be on the order of 1-3.

3.6.2 High-intensity imaging

At high intensities, the absorption cross-section can no longer be treated as constant. Using (3.23) to integrate (3.22), we find that (3.24) has to be modified to include a linear term [74]:

$$\tilde{n} = \sigma_0^{-1} \left[-c_\sigma \ln\left(\frac{I_\mathrm{f}}{I_\mathrm{i}}\right) + \frac{I_\mathrm{i} - I_\mathrm{f}}{I_\mathrm{sat}} \right].$$ (3.25)

While measuring ODs in the low-intensity limit only requires ratios of measured CCD counts, high-intensity imaging requires absolute calibration of the recorded intensities. We do this by recording thermal clouds produced at the end of the same experimental sequence with different intensities I_i. All images are processed with different assumed values of I_sat, and we choose the one that yields the smallest variations in total atom number $N = \iint \tilde{n} \mathrm{d}x\mathrm{d}y$ versus I_i. Finally, c_σ is calibrated by comparing N_0 and N_th in partially condensed clouds with theoretical predictions, as described in [76, 77]. We find typically find $c_\sigma = (1.7 \pm 0.2)$, and we repeat the calibration after any major change to the experiment. This c_σ is typical of other similar experiments [78, 79].

3.6.3 Condensate Density

Absorption imaging yields the column density $\tilde{n}(x, y) = \int n(x, y, z)\mathrm{d}z$. Below, we present a theoretical model for n and thus $\tilde{n}$. The parameters of the model are the thermodynamic variables such as T, N_0 and N_th. Having an analytic model allows us to determine these parameters by least-square fitting of the model function to our measured $\tilde{n}$. Below, we review the theoretical description for clouds trapped in or released from a harmonic potential.

Trapped Gas

At temperatures $0 < T < T_c$, the gas has two components: the condensate in the ground state and the thermal cloud comprising atoms in the excited states. Detecting the condensate experimentally requires a theoretical model for the spatial density of each component.

The thermal component can be treated semi-classically [24] to obtain the density profile

$$n_\mathrm{th}(\mathbf{r}) = \frac{1}{\lambda_T^3} g_{3/2}\left[\exp\left(\frac{\mu - V(\mathbf{r})}{k_B T}\right)\right],$$ (3.26)

with the polylogarithm function $g_j(z) = \sum_i z^i/i^j$

The density of the condensate part is directly proportional to $|\Psi|^2$, where Ψ is the many-body ground state wavefunction. For an ideal gas, this would be the Gaussian ground state of the simple harmonic oscillator. However, even in dilute gases, this is strongly affected by interactions. We only consider two-body scattering processes described by the s-wave scattering length a. In the mean-field approximation, Ψ obeys the Gross-Pitaevskii equation [23]

$$i\hbar \frac{\partial \Psi}{\partial t} = -\frac{\hbar^2}{2m}\nabla^2\Psi + V(\mathbf{r})\Psi + U_0|\Psi|^2\Psi \qquad (3.27)$$

with $U_0 = 4\pi\hbar^2 a/m$ As discussed in [80], the kinetic energy term can be neglected under conditions typical in atomic BEC experiments (Thomas-Fermi approximation), and (3.27) can be solved to yield

$$n_0(\mathbf{r}) = \max\left(\frac{\mu - V(\mathbf{r})}{U_0}, 0\right). \qquad (3.28)$$

In the harmonic potential $V = \frac{1}{2}m(\omega_x^2 x^2 + \omega_y^2 y^2 + \omega_z^2 z^2)$, the density profile is thus parabolic and can be clearly distinguished from the thermal profile (3.26). Note that both components will have the same aspect ratio in an anisotropic trapping potential, the extent in a given direction being inversely proportional to the the trapping frequency. In general, imaging the trapped gas in-situ will yield a bimodal profile, and fitting the density distribution with a weighted sum of $n_{\text{th}}(\mathbf{r})$ and $n_{\text{c}}(\mathbf{r})$ allows quantitative analysis of the condensate.

Free Expansion

While in-situ imaging provides a direct picture of the condensate in real space, it is often convenient to study particle distributions in momentum space instead. A distinguishing property of the condensate in an anisotropic trap is that, unlike the thermal fraction, it is anisotropic in momentum space. Experimentally, this is possible to observe in a time-of-flight (ToF) measurement, where the condensate is allowed to expand freely for a fixed time before imaging. For large expansion times and negligible interactions, this technique provides a direct image of the momentum distribution.

Considering the time-dependence of density distributions above, it can be shown that both n_0 and n_{th} expand self-similarly [73]: the functional form of n_0 remains parabolic due to interactions, and n_{th} follows the $g_{3/2}$ distribution above (for a more detailed review, see [27, 28]). Keeping the essential functional form only, we can

write:

$$n_{\text{th}}(x, y, z) \propto g_{3/2} \left[\exp \left(\frac{\mu}{k_{\text{B}}T} - \sum_{i=x,y,z} \frac{x_i^2}{2R_i^2(t)} \right) \right], \tag{3.29}$$

$$n_0(x, y, z) \propto \max \left(1 - \sum_{i=x,y,z} \frac{x_i^2}{a_i^2(t)}, 0 \right). \tag{3.30}$$

For a partially condensed sample, we can set $\mu = 0$. Integrating (3.29) and (3.30) along z, we find the column densities

$$\tilde{n}_{\text{th}}(x, y) \propto g_2 \left[\exp \left(- \sum_{i=x,y} \frac{x_i^2}{2R_i^2(t)} \right) \right], \tag{3.31}$$

$$\tilde{n}_0(x, y) \propto \max \left(1 - \sum_{i=x,y} \frac{x_i^2}{a_i^2(t)}, 0 \right)^{3/2}. \tag{3.32}$$

The thermal radii R_i, and thus T, as well as the condensed fraction, can be determined by least-square fitting of the measured $\tilde{n}$ with a fitting function of the form $f(x, y) = A_{\text{th}}\tilde{n}_{\text{th}}(x, y) + A_0\tilde{n}_0(x, y)$. The fitting algorithm will only be numerically stable if the measured distribution is bimodal, as shown in the inset of Fig. 3.9. This is generally the case for thermal fractions above 50% and long ToF. If the condensed fraction is small or ill-defined, we can often extract N_{th} and T reliably by *excluding* the central region of the image and fitting the thermal wings only. This technique can be used to determine a good starting point for the bimodal fit [28]. Further, it becomes essential when analyzing uniform BECs: while we shall derive a functional form analogous to (3.31) for fitting the thermal wings, no analytic form is known for $\tilde{n}_0$. Further, $\tilde{n}_{\text{th}}$ peaks more steeply in the uniform trap case, meaning that the bimodality of the distribution is not clearly visible like it is in the harmonic case.

Chapter 4

Towards a Uniform BEC

Having created a Bose-Einstein condensate in a harmonic trap, our next goal was
to transfer it into a uniform potential. In this Chapter, we describe the necessary
steps. These include creating a suitable box potential, cancelling residual fields such
as gravity, and finally optimizing the experimental sequence to produce large BECs.
Further, we address the problem of detecting condensation in a uniform system,
as well as measuring thermodynamic properties of partially condensed clouds in a
uniform trap. We find that the experimental signature differs significantly from
the well-known case of a harmonic trap, making an accurate theoretical description
essential for further studies.

4.1 Adding the box potential

Most potentials used in atom trapping experiments can be described by simple power
laws. For example, we have described the linear quadrupole trap and the quadratic
optical dipole trap. Our ability to shape magnetic fields is somewhat limited: while
one can imagine a quadratic potential or, as in the case of a Helmholtz coil pair,
one with a leading term of order four, these generally offer very weak confinement,
limited by the size of current carrying components[1]. Optical fields, on the other
hand, can be engineered much more freely, with the achievable spatial resolution
only limited by the diffraction limit of the optics used. The resulting light field with
intensity $I(\mathbf{r})$ will create a trapping potential $U(\mathbf{r}) \propto I(\mathbf{r})$, as described in 3.5.3. By
reversing the sign of the detuning, δ, we can create attractive as well as repulsive
potentials. The main limitation of attractive (red-detuned) optical traps is their

---

[1]This approach is used in "BEC on a chip" systems, aided by the small size of (often printed)
components. In our case, the vacuum system imposes a minimum size of $\sim 10\,\mathrm{cm}$ on all coils

inherent heating [65]. Blue-detuned light, on the other hand, can be used to create dark-field optical traps (see e.g. [65] and references therein), in which the atoms are confined by repulsive walls in a region of low I, and thus experience little heating.

In this Section, we describe how these concepts were applied to create the first ever box-like trap for ultra-cold atoms. At the same time, we consider the effect of other external fields on the trapped atoms. These include the gravitational force, which creates a linear potential along the vertical direction. We thus address ways to cancel the gravitational potential, to make full use of our dark-field optical trap.

4.1.1 Dark optical trap

The prospects of creating arbitrary potential for ultra-cold atom experiments have been studied extensively in [81, 82]. Using a spatial light modulator (SLM), it is possible to imprint a phase pattern on a laser beam to create almost arbitrary shapes in the desired plane perpendicular to the propagation direction. Shaping light in three dimensions, on the other hand, is subject to constraints imposed by the Helmholtz equation (and ultimately, Maxwell's equations). However, many novel trapping geometries can be explored by intersecting two or more appropriately shaped beams. Our implementation is shown in Fig. 4.1. A single SLM is used to create two spatially separate beams: one in the shape of a ring and another in the shape of two sheets. The two beams are separated and guided to the vacuum cell, where both are intersected at right angles. The details of the holographic methods used to shape the beams can be found in [82]. The resulting dark-field region is cylindrical in shape and is aligned to overlap with the harmonic hybrid trap. We use off-resonant blue-detuned light, with a wavelength of $532\,\mathrm{nm}$, produced by an Excel solid state laser from Laser Quantum [83].

The performance of the trap can be gauged in two ways: first, by the effective trap parameter α which determines how closely the thermodynamics of the trapped gas resemble that of an ideal box system, and second, by the uniformity of the in-trap BEC density.

To estimate the effective parameter α, we recall that the effective volume scales as $V \propto T^{3/2-\alpha}$, or

$$\frac{\mathrm{d}\ln(V)}{\mathrm{d}\ln(T)} = \alpha - 3/2. \qquad (4.1)$$

The temperature-dependent volume can be determined from the analytic model for the light intensity $I(\mathbf{r})$, as well as from $I(\mathbf{r})$ measured in a bench environment. Alexander Gaunt found that the largest contribution to α comes from the tube
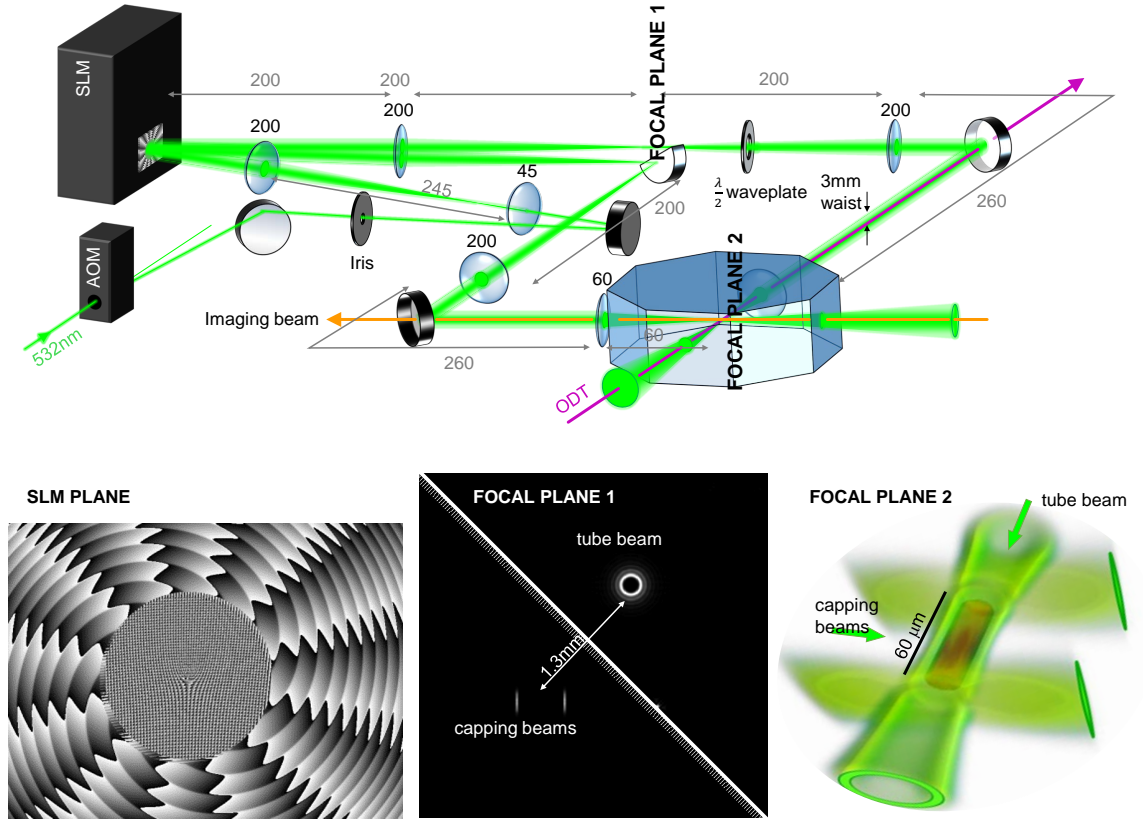
Figure 4.1: Dark optical box trap (adapted from [82]). Top: experimental setup for creating the walls of the box, showing distances and focal lengths in mm. Bottom left: SLM phase pattern (phases from 0 to 2π are represented by colours from black to white). Bottom center: tube and two sheet beams in the first focal plane, before being separated by a half-mirror. Solid line shoes the mirror edge. Bottom right: tube beam and sheet beams intersected at 90° in the second focal plane.

beam, with the effective power in the radial direction $s_r \gtrsim 10$ over a wide range of T [82]. s_r determines two of the three terms in (2), suggesting overall power $s \gtrsim 15$ and thus $1.5 \leq \alpha \leq 1.7$.

To consider the uniformity of the condensed phase, we recall that the density n is determined by the Thomas-Fermi approximation (under most experimental conditions, see later),

$$n(\mathbf{r}) = \frac{\mu - U(\mathbf{r})}{\gamma}. \tag{4.2}$$

We can easily calculate e.g. the standard deviation of the density from its mean $\langle n \rangle$ over the trapping volume ($U(\mathbf{r}) < \mu$). For the sake of argument, consider $U(\mathbf{r}) \propto r^s$. It is easy to show that the normalized root mean square deviation in density is

$$\frac{\langle (n - \langle n \rangle)^2 \rangle^{1/2}}{\langle n \rangle} = \sqrt{\frac{3}{2s + 3}} \tag{4.3}$$

where $\langle \cdots \rangle$ denotes averaging over the trap volume. For $s = 2$, this results in a 43% variation in density, while in an r^{15} potential it would be near 9%. On the other hand, speckle noise dominates $U(\mathbf{r})$ over large portions of our trap, with noise levels consistently below 1% [82]. Further, the flatness of n is fundamentally limited by the healing length ξ, typically of the same order as the extent of the sloping potential walls (few μm).

While the predicted quality of the dark optical trap look promising, the above considerations suggest that ultimately the flatness requirements will be determined by the exact origin of the experimental signatures used to probe it. Examples presented in subsequent Chapters include thermodynamic studies, Bragg spectroscopy of the ground state as well as measurements of the mean field energy.

4.1.2 Gravity compensation

While our atoms may be confined in an excellent box-shaped trap, the potential they experience is far from uniform until we take care of the gravitation potential. A simple estimate shows that the gravitational potential, expressed in temperature units, equals to

$$\frac{mg}{k_\mathrm{B}} = \frac{1\,\mu\mathrm{K}}{10\,\mu\mathrm{m}} \tag{4.4}$$

for ^{87}Rb atoms. For a BEC of $N_0 = 10^5$ atoms in a cylindrical trap with length $l = 30\,\mu$m and radius $r = 15\,\mu$m, the chemical potential is $\mu = \gamma n_0 = 1.7\,\mathrm{nK} \times k_\mathrm{B}$. Keeping the linear contribution to the trapping potential below, say, 0.1μ requires cancelling gravity to better than $0.6 \times 10^{-4}g$. A common approach is to combine a gravity-cancelling quadrupole field with a strong homogeneous bias field along the vertical direction (x), resulting in a magnetic field of the form

$$\mathbf{B} = B' \begin{pmatrix} x \\ -y/2 \\ -z/2 \end{pmatrix} - B_0 \begin{pmatrix} 1 \\ 0 \\ 0 \end{pmatrix}. \tag{4.5}$$

As described in 3.5.2, this creates a potential proportional to $B = |\mathbf{B}|$. Expanding to second order in x and $r = \sqrt{y^2 + z^2}$, we find

$$B = B_0 - B'x + \frac{1}{2}\frac{B'^2 r^2}{4B_0}. \tag{4.6}$$

Thus, we can cancel the gravitational potential to 1st order by choosing $B' = mg/\mu_B = 15.3\,\mathrm{G\,cm^{-1}}$ and a large enough B_0. The radial term in (4.6) corresponds

to a harmonic potential with trapping frequency

$$\omega_r^2 = \frac{\mu_B B'^2 r^2}{4 B_0}.$$ (4.7)

In practice, our coil arrangement is not perfectly aligned, which introduces a vertical trapping frequency ω_z. This frequency scales as $B_0^{1/2}$ - the inverse of (4.7). In our experiments, we are therefore limited to $B_0 = 30$ G, corresponding to a residual potential of $\omega_r = 2\pi \times 1.6$ Hz (as confirmed by measuring small center-of-mass oscillations of the cloud). This corresponds to a residual potential of 0.1 nK near the trap walls for a 30 μm trap - similar to that due to a relative change of 0.3×10^{-4} in B'. At the same time, we are able to stabilize B' to approximately 10^{-4} - we can improve on that by post-selecting images based on the position of the cloud center after long ToF in the more sensitive measurements.

4.2 Loading the BEC into the box

We have now described two major steps towards creating a uniform degenerate gas: first, we have a source of ultra-cold atoms in a harmonic trap (Chapter 3), and second, we have created a uniform box-like trapping potential. Next, we describe loading the atoms into the box. We describe our experimental procedure, and consider the evolution of the cloud as we transfer it between different trap types.

4.2.1 Experimental sequence

The typical transfer sequence is illustrated in Fig. 4.2. By ramping up the box trap before ramping down the optical dipole trap, we can achieve efficient transfer. The evolution of the trapping potential is kept slow to make the transfer as close to adiabatic as possible. The change in the *in situ* density profile is clearly seen in the high-intensity absorption images taken before and after the transfer. However, unlike in a harmonically trapped cloud, in a uniform trap these images do not contain any information on the temperature of degeneracy of the cloud - the density profile is well fitted by a model assuming uniform density over the cylindric trapping region, as shown in Fig. 4.2 (d). We first consider the theoretically expected evolution of the cloud's thermodynamic properties during the transfer, before discussing ways to measure these for a uniform gas using time-of-flight imaging.
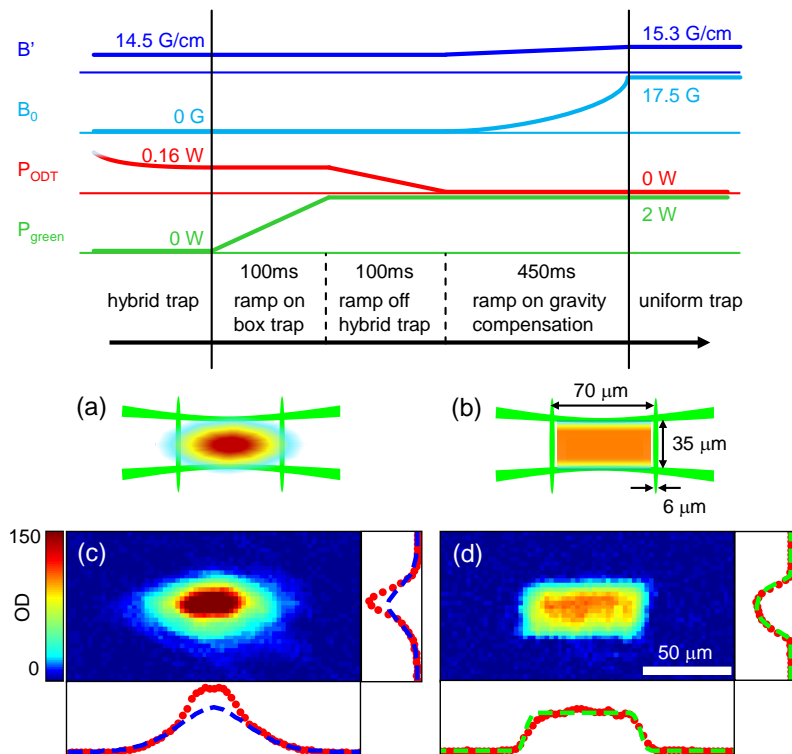
Figure 4.2: Loading sequence of the box trap(adapted from [82]). Top: evolution of the quadrupole gradient B', bias field B, ODT power P_{ODT} and green laser power P_{green}. We also show a schematic cross-section of cloud relative to the green trapping beams just before (a) and after (b) the transfer. Below, we show absorption images of the cloud at the respective times (c,d), together with integrated density profile along two directions. Dashed lines represent best fits described in the text.

4.2.2 Effect of transfer on phase space density and condensate fraction

Transferring either a thermal or a partially condensed cloud from the harmonic hybrid trap into the uniform trap will affect the phase space density ρ in the former case, and the condensate fraction N_0/N in the latter. To estimate these effects, we consider an adiabatic transfer - that is, one at constant entropy S. We neglect atom losses (due to both mismatched trap size and evaporation) during the transfer.

Thermal clouds

First, we consider the limit $T \gg T_c$. Using results and notation from Chapter 2, we can write the cloud's entropy in the form

$$\frac{S}{k_{\text{B}} N} = (\alpha_i + 1) - \ln \zeta(\alpha_i) - \ln \rho_i + \ln \zeta(3/2), \tag{4.8}$$

where α_i is the characteristic parameter of the respective trap type, i.e. $\alpha_1 = 3$ and $\alpha_2 = 3/2$ for a transfer from the harmonic to the uniform trap. From $S = \mathrm{const}$ we can immediately deduce

$$\frac{\rho_2}{\rho_1} = \frac{\zeta(\alpha_1)}{\zeta(\alpha_2)}e^{\alpha_2 - \alpha_1} = 0.10. \tag{4.9}$$

A 10-fold decrease in the phase space density (and an even bigger drop in the collision rate), combined with inefficient evaporation, suggests that the cloud should be transferred into the uniform box as late as possible in the cooling sequence. Further, limitations on the size and wall height of the uniform trap make it impossible to load large thermal clouds at high temperatures.

Partially condensed clouds

Instead, we consider transferring a degenerate cloud. The entropy in this case takes the form

$$\frac{S}{k_{\mathrm{B}}} = (\alpha_i + 1)\frac{\zeta(\alpha_i + 1)}{\zeta(\alpha_i)}N_{\mathrm{th},i}. \tag{4.10}$$

Assuming the cloud remains condensed, the final thermal number can be determined from

$$\frac{N_{\mathrm{th},2}}{N_{\mathrm{th},1}} = \frac{(\alpha_1 + 1)}{(\alpha_2 + 1)}\frac{\zeta(\alpha_1 + 1)}{\zeta(\alpha_2 + 1)}\frac{\zeta(\alpha_2)}{\zeta(\alpha_1)} = 2.81. \tag{4.11}$$

The condensed fraction after transfer can be written as

$$\left.\frac{N_0}{N}\right|_2 = \max\left[2.81 \times \left(\left.\frac{N_0}{N}\right|_1 - 0.644\right), 0\right]. \tag{4.12}$$

This suggests that the condensate will disappear if the initial condensed fraction is below 64%. In our experiments, we are unable to measure condensed fractions above 70% reliably. We do, however, observe that samples with smaller condensates are no longer condensed after loading into a sufficiently deep box trap. In shallower traps, evaporation can drive further cooling and condensation.

4.2.3 Evaporative cooling in the uniform trap

We can reduce the temperature and increase degeneracy in the uniform trap further by lowering the optical power in the walls. As discussed in 3.5.1, evaporative cooling in the uniform trap should be comparable to that in a conventional gravity-compensated optical dipole trap. We see the effect of cooling in the sharp increase of the occupancy of the low-momentum states, as shown in Fig. 4.3. In contrast
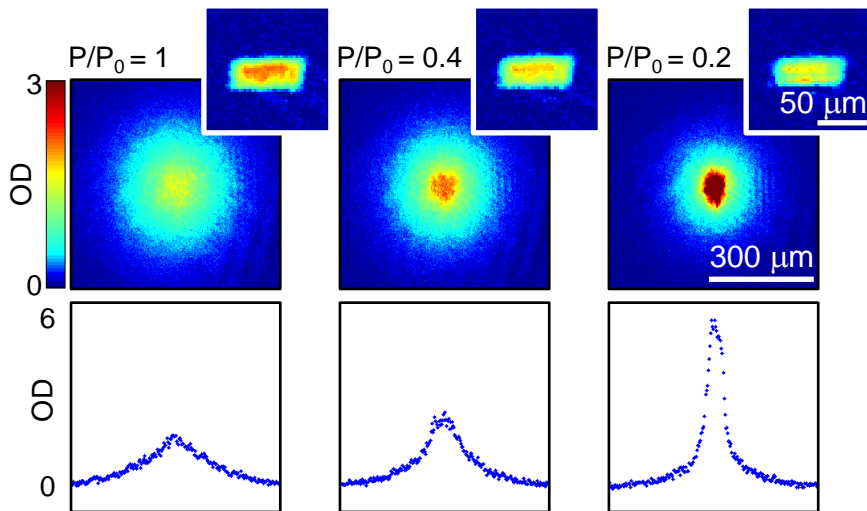
Figure 4.3: (Reproduced from [20]) Evolution of the Bose gas in a uniform trap as the optical power P is lowered from its initial value P_0. Absorption images taken after 50 ms ToF. Insets show corresponding *in situ* images. Bottom row shows cuts through the momentum distributions.

to the case of a harmonic trap, no dramatic effects of cooling are observed *in situ*. However, the appearance of a BEC is clearly seen in the bimodality of the momentum distribution and the anisotropic expansion in time of flight. Extracting the condensate fraction and temperature from these images relies on an analytic model, which we develop below.

4.3 Thermometry on a uniform BEC

As explained in 3.6.3, determining T, N_{th} and N_0 from an absorption image relies on a theoretical model. Condensation in the harmonic trap can be observed *in situ*(i.e. in *real* space) as well as in ToF images (i.e. in *momentum* space). A clear example of this was seen in Fig. 4.2 (c), where we show the fit to the thermal wings of the condensate following 3.26. The excess atoms in the central region can be identified with the condensate. In a box trap, both the thermal cloud and condensate densities are uniform - Fig. 4.2 (d) shows no signature of condensation comparable to the harmonic case. The variations in optical density are a result of the box shape only. Consider a cylindrical box of length L and radius R, with its axis at $x = z = 0$. Integrating along the imaging direction z, we expect

$$\tilde{n}(x, y, t = 0) \propto \Pi\left(\frac{y}{L}\right)\Pi\left(\frac{x}{2R}\right)\sqrt{1 - \left(\frac{x}{R}\right)^2},\qquad(4.13)$$

with the rectangle function $\Pi(x) = \begin{cases} 1, & |x| \leq 1/2 \\ 0, & |x| > 1/2 \end{cases}$. In practice, we have to correct for the finite imaging resolution, σ, to determine L and R. Assuming a Gaussian point spread function, we write

$$K(x, y) = \frac{1}{\sqrt{2\pi\sigma^2}} \exp\left(-\frac{x^2 + y^2}{2\sigma^2}\right), \tag{4.14}$$

$$\tilde{n}'(x, y, t = 0) = \iint \tilde{n}(x', y', t = 0) K(x - x', y - y') \mathrm{d}x' \mathrm{d}y'. \tag{4.15}$$

Fig. 4.2 (d) shows a typical fit (dashed green lines) with $\sigma = 2.5\,\mu\mathrm{m}$, $R = 15 \pm 1\,\mu\mathrm{m}$ and $L = 63 \pm 2\,\mu\mathrm{m}$. It is clear that these results apply to both the thermal atoms and the condensate. To distinguish the two, we must consider the behavior of the thermal cloud in time of flight.

4.3.1   ToF expansion from an ideal box

First, consider an ideal box of volume V, such that $U(\mathbf{r}) = \begin{cases} 0, & \mathbf{r} \in V \\ \infty, & \mathbf{r} \notin V \end{cases}$. To describe the thermal gas, we can consider the quantum-mechanical eigenstates ϵ_j and their respective occupancies $f[\epsilon_j]$. If we know the behaviour of the respective wavefunctions $\Psi_j(t)$, we can, in theory, deduce the condensate density (and any other observable) at any time. While this approach is suitable for a simple potential like a square box, finding the eigenstates and their time-dependence is a daunting task for, say, a general power-law potential. It is thus helpful to consider the local density approximation, which treats the gas as (locally) uniform at each point in space [23].

Local density approximation

Within the LDA, we replace the sum over all macroscopic quantum states with a sum over local plane-wave states of momentum p, as per

$$\sum_j f[\epsilon_j] \to \iint f\left[\epsilon(\mathbf{p}, \mathbf{r}')\right] \frac{\mathrm{d}^3\mathbf{p}\,\mathrm{d}^3\mathbf{r}'}{(2\pi\hbar)^3}, \tag{4.16}$$

$$n_{\mathrm{th}}(\mathbf{r}, t) = \sum_j f[\epsilon_j]^2 |\Psi_j(\mathbf{r}, t)|^2 \approx \iint f\left[\epsilon(\mathbf{p}, \mathbf{r}')\right] \delta^3\left(\mathbf{r} - \left(\mathbf{r}' + \frac{\mathbf{p}}{m}t\right)\right) \frac{\mathrm{d}^3\mathbf{p}\,\mathrm{d}^3\mathbf{r}'}{(2\pi\hbar)^3} \tag{4.17}$$

Integrating over $\mathbf{p}$, we get

$$n_{\mathrm{th}}(\mathbf{r}, t) \propto \int f\left[\epsilon\left(\mathbf{p} = \frac{m}{t}(\mathbf{r} - \mathbf{r}'), \mathbf{r}'\right)\right] \mathrm{d}^3\mathbf{r}' \tag{4.18}$$

So far, we have not made any assumptions about the nature of the potential or the statistical properties of our gas. We now recall that a non-relativistic Bose gas follows Bose-Einstein statistics, defined by

$$\epsilon(\mathbf{p}, \mathbf{r}) = U(\mathbf{r}) + \frac{\mathbf{p}^2}{2m}, \tag{4.19}$$

$$f[\epsilon] = \frac{1}{\mathcal{Z}\exp(\beta\epsilon) - 1} = g_0(\mathcal{Z}\exp(-\beta\epsilon)). \tag{4.20}$$

Using $U(\mathbf{r}) = 0$ (uniform potential), and defining the thermal radius $r_{\mathrm{th}} = t\sqrt{k_{\mathrm{B}}T/m}$, we find

$$n_{\mathrm{th}}(\mathbf{r}, t) \propto \int_V g_0\left\{\mathcal{Z}\exp\left[-\frac{(\mathbf{r} - \mathbf{r}')^2}{2r_{\mathrm{th}}^2}\right]\right\}\mathrm{d}^3\mathbf{r}'. \tag{4.21}$$

Unsurprisingly, this can be written as a convolution of the g_0-like momentum distribution with the *in situ* density distribution $n_{\mathrm{th}}(\mathbf{r}, t = 0)$:

$$n_{\mathrm{th}}(\mathbf{r}, t) \propto \int_{\mathbb{R}^3} g_0\left\{\mathcal{Z}\exp\left[-\frac{(\mathbf{r} - \mathbf{r}')^2}{2r_{\mathrm{th}}^2}\right]\right\} \times n_{\mathrm{th}}(\mathbf{r}', t = 0)\mathrm{d}^3\mathbf{r}' \tag{4.22}$$

$$= \int_{\mathbb{R}^3} g_0\left\{\mathcal{Z}\exp\left[-\frac{\mathbf{r}'^2}{2r_{\mathrm{th}}^2}\right]\right\} \times n_{\mathrm{th}}(\mathbf{r} - \mathbf{r}', t = 0)\mathrm{d}^3\mathbf{r}'. \tag{4.23}$$

Integrating both sides over z is straightforward in this form, and allows us to evaluate the z' integral (see Appendix E), yielding the column density

$$\tilde{n}_{\mathrm{th}}(x, y, t) \propto \int_{\mathbb{R}^2} g_{1/2}\left\{\mathcal{Z}\exp\left[-\frac{x'^2 + y'^2}{2r_{\mathrm{th}}^2}\right]\right\}\tilde{n}_{\mathrm{th}}(x - x', y - y', t = 0)\mathrm{d}x'\mathrm{d}y'. \tag{4.24}$$

This is, again, a convolution of the (integrated) momentum distribution (mapped to length units) with the *in situ* column density (4.13). Notice that the first term in the integral above *diverges* at $x = y = 0$ as $\mathcal{Z} \to 1$ ($\mu \to 0$): we will return to this property when we consider arbitrary power law traps below. The divergence is only curbed by the initial size - the convolution is essential to obtaining a meaningful model of the recorded optical densities. The striking difference between the uniform and the harmonic case is illustrated in Fig. 4.4. In fact, the high occupancy of the low-momentum states prompted us to scrutinize (4.17) by treating the problem fully quantum-mechanically.

Quantum-mechanical description

The abundance of low-momentum states in our semi-classical distribution at $\mu = 0$ raises the question whether these can be identified with the thermal cloud or must be attributed to the atoms in the ground state of the trap, i.e. the condensate.
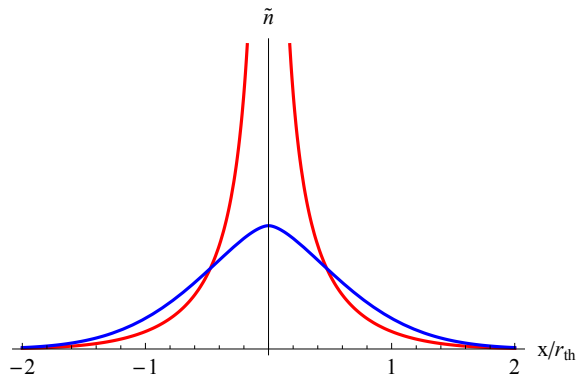
Figure 4.4: Cross-section through the calculated optical density of a thermal cloud with $\mathcal{Z} = 1$ released from a harmonic (blue) and uniform (red) traps at long time of flight. Both profiles are normalized to the same total atom number.

This is essential for extracting N_0 correctly from time-of-flight imaging. A related problem arising from (4.17) is that of the effect of the LDA on the predicted critical number. The effect on the critical number is discussed in 5.1.1.

Here, we study the expansion of a thermal cloud from our box trap using a non-interacting quantum-mechanical model. First, we consider the momentum distribution of the cloud, corresponding to the long-ToF behaviour of the sample. For an ideal rectangular box with dimensions $l_x \times l_y \times l_z$, we can write the energy levels $E_{n_x,n_y,n_z} = \frac{\hbar^2 \pi^2}{2m}(\frac{n_x^2}{l_x^2} + \frac{n_y^2}{l_y^2} + \frac{n_z^2}{l_z^2})$, $\quad n_i = 1, 2, \ldots$, with separable wavefunctions

$$\Psi_{n_x,n_y,n_z}(\mathbf{r}) = \Psi_{n_x}(x)\Psi_{n_y}(y)\Psi_{n_z}(z), \tag{4.25}$$

$$\Psi_{n_x}(x) = \sqrt{\frac{2}{l_x}} \sin\left(\frac{n\pi x}{l_x}\right), \quad 0 \le x \le l_x. \tag{4.26}$$

The wavefunction is separable in both real and momentum space, and we can thus consider one direction only. With l the relevant box size and $p = \hbar k$, the momentum wavefunction takes the following form (up to a phase factor):

$$\Psi_n(k) = \frac{1}{2}\sqrt{\frac{l}{\pi\hbar}}\left[\text{sinc}\left(\frac{lk - n\pi}{2}\right) - (-1)^n \text{sinc}\left(\frac{lk + n\pi}{2}\right)\right]. \tag{4.27}$$

We plot $|\Psi_n(k)|^2$ for $n = 1, 2, 3, 4$ in Fig. 4.5. For $n \ge 2$, the eigenfunctions contain a pair of peaks in momentum space, centered at $k = \pm\frac{n\pi}{l}$. Importantly, the momentum distributions of different thermal states add incoherently. In the high-T limit, i.e., assuming similar occupation of the relevant quantum states, we can approximate the momentum distribution as

$$f(k) \approx \sum_{n=1}^{\infty} |\Psi_n(k)|^2 = \sum_{n=-\infty}^{\infty} \text{sinc}^2\left(\frac{lk - n\pi}{2}\right). \tag{4.28}$$
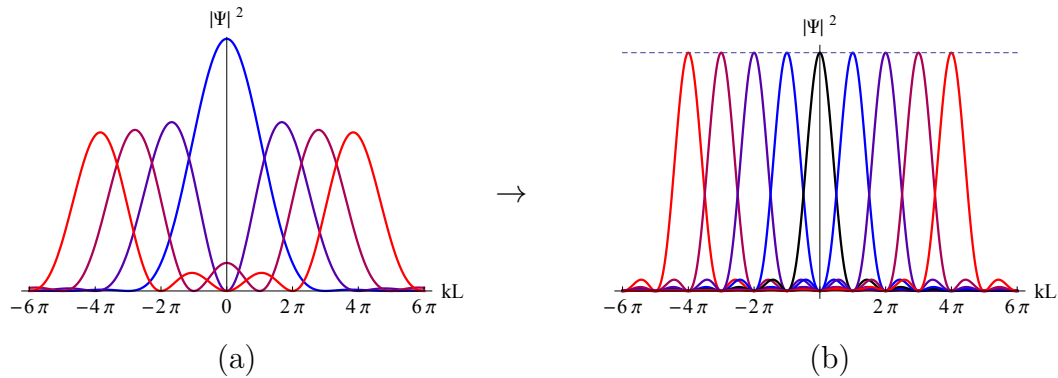
Figure 4.5: (a) Lowest 4 eigenstates of the box potential in momentum space, and (b) an equivalent decomposition of the high-T momentum distribution.

The last sum is equivalent to a uniform distribution, as is best seen by applying the convolution theorem to its Fourier transform (note this is *not* equivalent to the real-space wavefunction).

While in the case considered above we assume a uniform occupation of all states (and, implicitly, a microscopic occupation of the ground state), the treatment can be extended to an arbitrary (thermal Bose) envelope applied to the n-states. For all $k \gtrsim 1/l$, numerical calculations (by directly summing over n-states with a suitable Bose occupation factor) show that the momentum distribution is indeed equivalent to the LDA prediction.

Next, we turn our attention to the central region of the cloud and small time of flight, where both the LDA and the quantum-mechanical descriptions are affected by initial-size effects, and we must solve the time-dependent Scrödinger equation to allow direct comparison. The evolution of the wavefunction (4.26) is easy to describe in k-space, leading to

$$\Psi_n(k,t) = \Psi_n(k,0) \times \exp\left(-i\frac{\hbar^2 k^2}{2m}t\right) \tag{4.29}$$

$$\Rightarrow \quad \Psi_n(x,t) \propto \Psi_n(x,0) * \frac{1}{\sqrt{t}}\exp\left(i\frac{x^2 m}{2\hbar t}t\right). \tag{4.30}$$

To quantify possible discrepancies between the LDA and the wavefunction approach, we consider a cloud released from a $30 \times 30 \times 30\,\mu\mathrm{m}^3$ volume trap, and calculate the column density numerically using each approach for a wide range of T and μ. In Fig. 4.6 we illustrate the relative error in the column density at the box center for different expansion times. Here, we show data for the case $T = 100\,\mathrm{nK}$, $\mu = -0.1\,\mathrm{k}T$, and sum states with $n_x, n_y \leq 100$ explicitly. Higher-lying states are taken into account by including an analytic remainder term. The agreement between
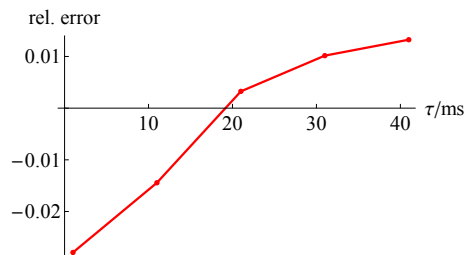
Figure 4.6: Relative error of the semi-classical approximation. $l_x = l_y = 30\,\mu\mathrm{m}$, $T = 100\,\mathrm{nK}$, $\mu = -0.1\,\mathrm{k}T$. States with $n_x, n_y \leq 100$ are summed, and an analytical estimate for the remainder term is used.

the LDA and the full quantum-mechanical sum is excellent, including at small time of flight were we expect largest deviations. We thus use the LDA model for image analysis throughout the experiments described in this Thesis.

4.3.2 ToF expansion from a quasi-uniform power-law trap

We now extend the LDA treatment of 4.3.1 to a general power-law potential $U(\mathbf{r}) \propto r^s$. The Bose factor becomes

$$f(\mathbf{p}, \mathbf{r}) = g_0 \left\{ \mathcal{Z} \exp\left[-\beta a_s r^s - \beta \frac{p^2}{2m} \right] \right\}. \tag{4.31}$$

Integrating f over $\mathbf{p}$ (see Appendix E), we find the *in situ* density distribution

$$n_{\mathrm{th}}(\mathbf{r}, t = 0) \propto g_{\frac{3}{2}} \left\{ \mathcal{Z} \exp\left[-\beta U(\mathbf{r}) \right] \right\}. \tag{4.32}$$

On the other hand, we can integrate f over all $\mathbf{r}$ to find the momentum distribution of the cloud (as measured in the very long ToF):

$$n_{\mathrm{th}}(\mathbf{p}) \propto g_{\frac{3}{s}} \left\{ \mathcal{Z} \exp\left[-\beta \frac{p^2}{2m} \right] \right\}, \tag{4.33}$$

where $\frac{3}{s} \equiv \alpha - \frac{3}{2}$, according to the notation introduced previously. Now, it is tempting to write the ToF density as a convolution of the two. Formally, (4.18) remains unchanged, and

$$n_{\mathrm{th}}(\mathbf{r}, t) \propto \int g_0 \left\{ \mathcal{Z} \exp\left[-\beta U(\mathbf{r}') - \frac{(\mathbf{r} - \mathbf{r}')^2}{2 r_{\mathrm{th}}^2} \right] \right\} \mathrm{d}^3 \mathbf{r}'. \tag{4.34}$$

However, in the general case $s < \infty$, the integrand can not be factorized like we did above. Thus,

$$n_{\mathrm{th}}(\mathbf{r}, t) \neq \int n_{\mathrm{th}}\left(\mathbf{p} = \frac{m}{t}(\mathbf{r} - \mathbf{r}') \right) \times n_{\mathrm{th}}(\mathbf{r}', t = 0) \mathrm{d}^3 \mathbf{r}'. \tag{4.35}$$

The integrand does, however, factorize when the exponential factor is small and $g_0(\mathcal{Z}e^{(\cdots)}) \approx \mathcal{Z}e^{(\cdots)}$ (i.e. the Bose factor takes the Boltzmann form). Moreover, if the potential has sharp walls in one direction, the line density $\iint n$ along this direction will be described precisely by the convolution with a box function, while α will be determined by the "invisible" directions. Even in the most general case, numerical modeling shows that the difference between the exact distribution and one written as (4.35) is diminishing as one goes from n to column density $\tilde{n} = \int n$ to line density $\int \tilde{n} = \iint n$.

In practice, the *in situ* density is indistinguishable from that of a uniform box due to the limitations of our imaging system, and we can use the form (4.13). We always analyze the region $r \gtrsim r_{\text{th}}$, and the time of flight is large to ensure that $r_{\text{th}} \gg R, L$, meaning that convolving the (integrated) momentum distribution (4.33) with (4.13) introduces a very small correction outside the central region. In the central region, on the other hand, it is convenient because it ensures the correct normalization of our distribution and allows us to count the thermal atom number without worrying about the divergence of the fitting function. The details of our fitting routine are summarized in the following section.

4.3.3 Image analysis

To analyze the column density extracted from the absorption images, we use two-dimensional fitting functions of the form[2]

$$\tilde{n}(x, y) = \frac{2\pi A}{r_x r_y} g_{\alpha-1} \left\{ \exp\left(\tilde{\mu} - \frac{x^2}{2r_x^2} - \frac{y^2}{2r_y^2} \right) \right\} * K(x, y), \qquad (4.36)$$

with the convolution kernel normalized to $\iint K(x, y)\mathrm{d}x\mathrm{d}y = 1$. We perform least-square fitting by minimizing $\sum_{i,j} M_{i,j} |\tilde{n}(x_i, y_j) - \tilde{n}_{i,j}|^2$ over the pixels (i, j) of the high-intensity absorption image, with the exclusion mask M defined by

$$M_{i,j} = \begin{cases} 1, & \frac{(x_i - x_c)^2}{r_1^2} + \frac{(x_i - x_c)^2}{r_2^2} > 1 \\ 0, & \text{otherwise} \end{cases} . \qquad (4.37)$$

Exclusion radii r_1 and r_2 are chosen such that the quasi-pure condensates remain within the excluded region throughout ToF. The fitting parameters $(\alpha, A, \mu, r_x, r_y)$

---

[2]We assume that ODs have been converted to atomic column densities.

relate to the thermodynamic properties of the condensate via[3]

$$\mathcal{Z} = e^{\tilde{\mu}}, \tag{4.38}$$

$$N_{\text{th}} = A g_\alpha(\mathcal{Z}), \tag{4.39}$$

$$k_{\text{B}} T_{x,y} = \frac{r_{x,y}^2 m}{t^2}. \tag{4.40}$$

We extract the condensate number N_0 by counting the difference between the measured column densities and the thermal fit over the exclusion region:

$$N_0 = \sum_{i,j} (1 - M_{i,j})(\tilde{n}_{i,j} - \tilde{n}(x_i, y_j)). \tag{4.41}$$

On thermodynamic grounds (Chapter 2), the overall amplitude A is not an independent parameter. In fact, for an ideal Bose gas,

$$A_{\text{th}} = \left(\frac{k_{\text{B}} T}{E_\alpha}\right)^\alpha \equiv \left(\frac{T}{\theta_\alpha}\right)^\alpha \tag{4.42}$$

$$\theta_\alpha = \text{const} \tag{4.43}$$

We will use this equality in the analysis of our trap below, as well as in the context of saturation in Chapter 5.

4.4 How good is our trap?

As discussed in [20], determining the value of α from the least-square fits is impractical. While it is easy to distinguish $\alpha = 3$ (harmonic) from $\alpha = 3/2$ (uniform), small variations around the latter do not lead to a noticeable increase in the least-squares residue. However, we can check the self-consistency of the fits according to (4.43). Identifying the value of α to be used in fits is essential to determining N_0, N_{th} and T accurately. In Figure 4.7 (a), we plot θ versus T for $1.5 \leq \alpha \leq 2.0$. The data is extracted by fitting our model to a range of clouds obtained by varying the final evaporation depth in the box trap. The analysis presented here is similar to that published in [20], with the following differences:

- We fit the 2D column density distribution $\tilde{n}(x, y)$, while in [20] the data was integrated and fitted in 1D.

---

[3]We define two temperatures for fitting purposes, one of the two is typically affected by residual trapping during the expansion. We introduce the necessary corrections, as well as a model-independent way to measure energy, in the next Chapter.

- We use an elliptic exclusion region, while [20] effectively excludes a strip region (since exclusion is done on the integrated 1D data).

- We restrict our analysis of θ to high-temperature clouds ($70\,\text{nK} \leq T \leq 110\,\text{nK}$).

Using a smaller temperature range solves several problems: first, as discussed in section 4.1.1, the effective value of α could vary with T; second, non-saturation effects [76] can potentially make θ dependent on the condensate fraction.

We extract the slopes of the straight-line fits shown in Fig. 4.7 (a), and plot them against α in Fig. 4.7 (b). It is clear that the condition $d\theta/dT = 0$ strongly excludes the values $\alpha \geq 1.7$. Thus, we can say that the effective power of our potential is $s \geq 15$. We use the value $\alpha = 1.6$ ($s = 30$) to extract the atom numbers in the thermal cloud and in the condensate, and plot them versus T in Fig. 4.7 (c) and (d), respectively. The fit in (c) corresponds to $N_{\text{th}} \propto T^{\alpha}$, and shows good agreement with the data. We can use the N_0 data to identify the transition point. From (d), we observe $T_c = 105 \pm 5\,\text{nK}$. The *predicted* value for the corresponding ideal-gas critical number is $N_c = 6.5 \pm 0.8 \times 10^5$ (using the measured box dimensions L and R). Both values with their error bars are shown in Fig. 4.7 (c), and the thermal number at the transition proves to be in excellent agreement with the ideal gas prediction.

In this Chapter, we have described the implementation of the first ever degenerate Bose gas in a uniform system. Understanding the inherent limitations of our approach is important for both developing the experimental setup and quantifying deviations from the theoretical box-like system. Our estimates show that these are extremely small, and first measurements suggest that the thermodynamics of the system closely follow the ideal-gas prediction made a century earlier. In subsequent Chapters, we continue probing our system using a variety of techniques. Our focus will be on testing the uniform-system behaviour while keeping in mind the influence of imperfections in our trapping geometry.
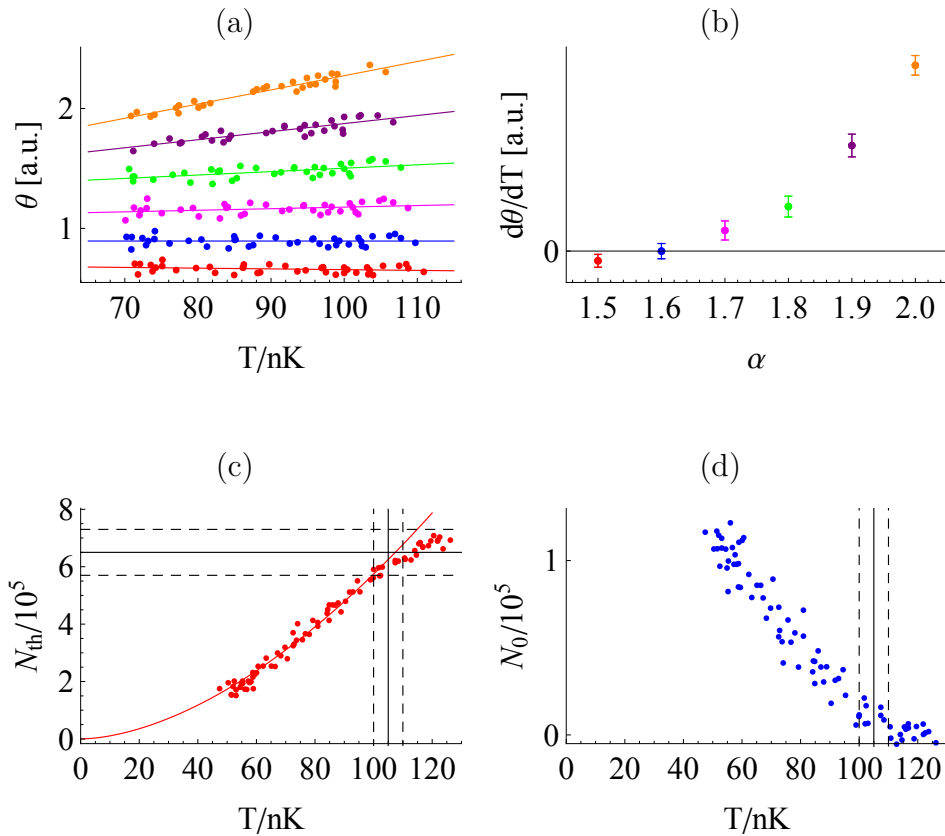
Figure 4.7: Self-consistency of thermodynamic properties of a quasiuniform degenerate Bose gas. (a) Variations of θ with T for different assumed α (see text; data sets correspond to the values of α shown in (b), i.e. between 1.5 (bottom, red) and 2.0 (top, orange)). (b) Slopes of the linear fits to θ v.s T for different α, extracted from (a). (c) Thermal atom number versus T, extracted using $\alpha = 1.6$. The solid red line shows the expected T^α scaling, and the black lines indicate the critical number and temperature. (d) Condensed atom number versus T, extracted using $\alpha = 1.6$. Black lines show the same critical temperature as in (c).

Chapter 5

Thermodynamics of a Uniform BEC

5.1 Transition temperature of a uniform BEC

One of the most important characteristics of Bose-Einstein condensation is the critical atom number $N_c(T)$. Historically calculated for an ideal uniform system [3–5], the treatment was later extended to consider the effects of interactions [84, 85] and finite trap size [86]. However, since most experiments to date have been conducted in harmonic traps, the theoretical focus has shifted towards these. A large number of theoretical [87–89] and experimental [16, 90, 91] studies have been conducted. Recently, the theory of condensation in more general power-law traps has also been considered [92, 93]. Below, we review the key theoretical results. We then present measurements of N_c in our box trap and compare these with theoretical predictions.

5.1.1 Theoretical description

Within the local density approximation (LDA), the thermal density, that is, the density of particles in the excited states, is limited to $n_c = \zeta(3/2)\lambda_T^{-3}$, with the thermal wavelength $\lambda_T = (2\pi\hbar^2/mk_BT)^{1/2}$, as defined in Chapter 2. This result extends trivially to a uniform system by multiplying both sides by the volume V. In a uniform system, condensation occurs simultaneously throughout the volume. The LDA can be extended to treat interactions between the thermal and condensed atoms, which we address in 5.2. Here, we only need to note that the interactions do not change the transition temperature T_c in a uniform system [23].

In a harmonically trapped gas, on the other hand, the density at the centre of

the trap is higher and exceeds n_c before other regions, and the interactions affect the transition temperature (among other properties).

However, the LDA explicitly neglects the effects of the low-momentum cut-off due to the finite size of the system: the lowest eigenstates of the trapping potential are far from being plane-wave states of the LDA. Thus, to account for the finite trap size, we must re-examine the density of states description.

Semi-classical description

As explained in 4.3.1, the main difference between the LDA and the full quantum-mechanical description lies in the way we count occupancies of all the energy eigenstates, as seen from the LDA

$$\sum_j f[\epsilon_j] \approx \iint f\left[\epsilon(\mathbf{p}, \mathbf{r}')\right] \frac{\mathrm{d}^3\mathbf{p}\,\mathrm{d}^3\mathbf{r}'}{(2\pi\hbar)^3} \tag{5.1}$$

(with the Bose factor f). Here, the left-hand side corresponds to the (exact) sum over all eigenstates j, while the right-hand side illustrates the phase-space integral used in the LDA . Evaluating the sum on the left is rarely possible directly, while the LDA can not, by definition, describe any effects of the finite trap size. On the other hand, the *semi-classical approximation* is often employed to write the sum on the left as

$$\sum_j f[\epsilon_j] \approx \int f[\epsilon]g(\epsilon)\mathrm{d}\epsilon, \tag{5.2}$$

with the density of states $g(\epsilon)$ defined by

$$\int_0^\epsilon g(\epsilon')\mathrm{d}\epsilon' = \sum_{j:\epsilon_j \leq \epsilon} 1. \tag{5.3}$$

To count the states with energies not exceeding ϵ, we start by considering a cubic box with side length L. The energy levels are given by

$$E_{n_x,n_y,n_z} = E_0(n_x^2 + n_y^2 + n_z^2), \tag{5.4}$$

with ground-state energy $E_0 = \frac{\pi^2\hbar^2}{2mL^2}$ and integer quantum numbers $n_{x,y,z} \geq 1$. $E \leq \epsilon$ corresponds to a volume in (n_x, n_y, n_z) of approximately

$$V_0(\epsilon) \approx \frac{1}{8} \times \frac{4\pi}{3}\left(\frac{\epsilon}{E_0}\right)^{3/2}. \tag{5.5}$$

The corresponding density of states is

$$g_0(\epsilon)\mathrm{d}\epsilon = \mathrm{d}V_0 \approx \frac{\pi}{4}\left(\frac{\epsilon}{E_0}\right)^{1/2}\frac{\mathrm{d}\epsilon}{E_0}. \tag{5.6}$$

This result is equivalent to the one quoted in Chapter 2 for $s \to \infty$.
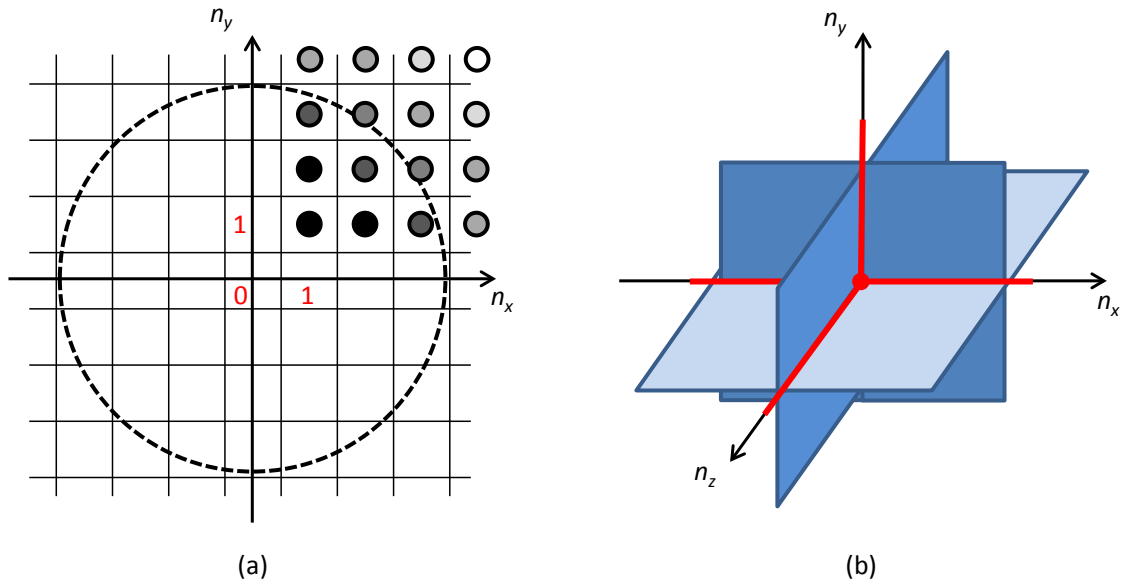
Finite size effects

(a)

(b)

Figure 5.1: Origin of finite size corrections in a uniform box. (a) Values of n_x, n_y contributing to the sum. The states (small circles) are shaded according to their thermal occupation number, from black (high) to white (low). Dashed circle : $\epsilon = $ const. (b) Origin of the higher-order corrections to the density of states: three planes ($n_x = 0$, $n_y = 0$, $n_z = 0$), three lines ($n_{x,y} = 0$, $n_{y,z} = 0$, $n_{z,x} = 0$) and the origin ($n_{x,y,z} = 0$) (see text).

We now consider the above standard derivation of $g(\epsilon)$ in more detail. In counting the states contained within a sphere of radius $\left(\frac{\epsilon}{E_0}\right)^{1/2}$ in the (n_x, n_y, n_z) space, we have implicitly included those points with one of the quantum numbers equal to 0. This is illustrated in Figure 5.1 (a), where only the allowed states ($n_x, n_y, n_z \geq 1$) are marked. To correct, we can subtract those "states" with $n_x = 0$ etc., which occupy the planes shown in Figure 5.1 (b). Now, those states with say $n_x = n_y = 0$ will have been subtracted *twice*, which can again be accounted for by introducing corrections for the states along the three axis (red in Fig. 5.1 (b)). Formally, one last term can be introduced for over-counting the state at $(0, 0, 0)$. This yields the corrected expression

$$V(\epsilon) = \frac{1}{8} \times \left[\frac{4\pi}{3} \left(\frac{\epsilon}{E_0} \right)^{3/2} - 3 \times \pi \left(\frac{\epsilon}{E_0} \right)^{2/2} + 3 \times 2 \left(\frac{\epsilon}{E_0} \right)^{1/2} - 1 \right]. \qquad (5.7)$$

The corresponding density of states is

$$g(\epsilon)\mathrm{d}\epsilon = \mathrm{d}V = \left[\frac{\pi}{4} \left(\frac{\epsilon}{E_0} \right)^{1/2} - \frac{3\pi}{8} + \frac{3}{2} \left(\frac{\epsilon}{E_0} \right)^{-1/2} \right] \frac{\mathrm{d}\epsilon}{E_0}. \qquad (5.8)$$

Now, evaluating the integral (5.2) is non-trivial. When using $g_0(\epsilon)$, we simply set $\mathcal{Z} = 1$ and integrate over $0 \leq \epsilon \leq \infty$. This does not work with the second term in $g(\epsilon)$ - the integral diverges. The problem has been treated extensively in [86]. As can be expected on dimensional grounds, the lower bound must be replaced by approximately[1] E_0, leading to the following form for the finite-size correction to the well-known result (2.6):

$$\frac{T_c}{T_{c,0}} - 1 \approx -\frac{2}{\sqrt{3\pi}}\frac{1}{\zeta(3/2)}(\beta_0 E_0)\ln(\beta_0 E_0), \tag{5.9}$$

$$\beta_0 E_0 = \frac{E_0}{k_{\mathrm{B}}T_{c,0}} \approx 2.1 N^{-1/3}. \tag{5.10}$$

We have extended this treatment to account for the anisotropy of the trap. For a
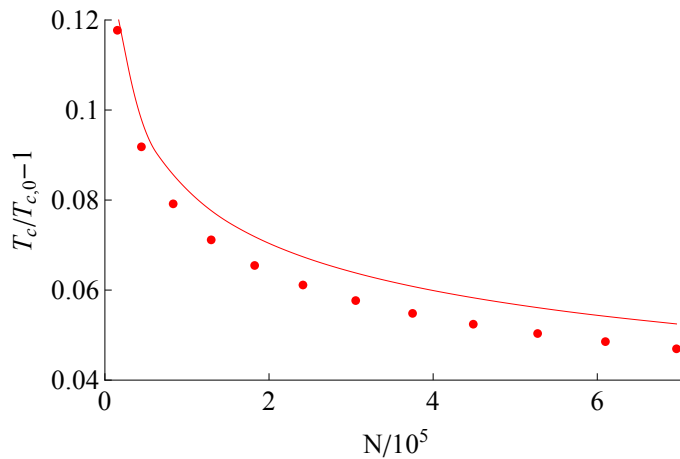
Figure 5.2: Finite size correction. Box size is $a = 2.4b = 2.4c = 63\,\mu\mathrm{m}$. We show the prediction of the equation (5.11) (solid line) and results obtained by direct summation over states.

trap with sides a, b, c, we find that the finite-size correction takes the form

$$\frac{T_c}{T_{c,0}} - 1 \approx -s(a,b,c)\frac{2}{\sqrt{3\pi}}\frac{1}{\zeta(3/2)}(\beta_0 E_0)\ln(\beta_0 E_0), \tag{5.11}$$

with the shape factor

$$s(a,b,c) = \frac{(abc)^{1/3}}{((a^{-1} + b^{-1} + c^{-1})/3)^{-1}}. \tag{5.12}$$

The finite-size correction is *positive* for realistic N, and is typically of the order of 5%. s is typically very close to unity: for $a = 2b = 2c$, $s - 1 \approx 5\%$. In Fig. 5.2, we compare the asymptotic expression (5.11) with the critical temperature obtained by explicitly summing the left-hand side of (5.2) numerically, and find good agreement.

---

[1]This applies to the first term of the integral as well. The corresponding correction is small due to fast convergence of the corresponding integral near 0.

5.1.2 Measuring the critical point

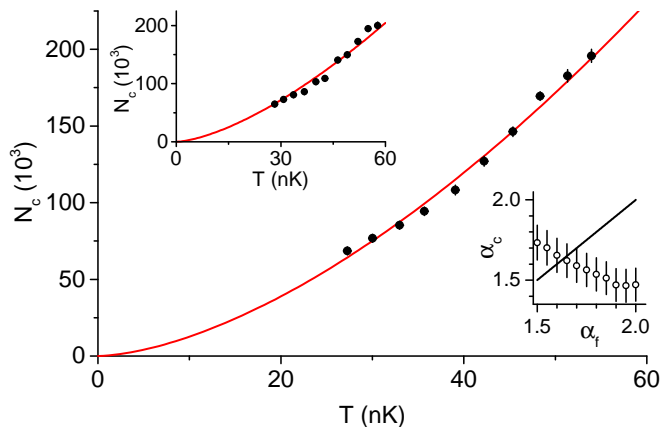**Figure 5.3:** Critical point for condensation (reproduced from [21]). A power-law fit, $N_c \propto T^{\alpha_c}$, gives $\alpha_c \approx \alpha_f = 1.65$ (see text). Bottom inset: Within errors, $\alpha_c = \alpha_f$ (solid line) is satisfied for $1.6 \lesssim \alpha_f \lesssim 1.7$. Top inset: Comparison with theory of a perfectly homogeneous gas, with fixed $\alpha_c = \alpha_f = 3/2$.

While detecting small corrections is beyond our measurement accuracy, showing the $N_c \propto T^\alpha$ scaling of the critical number also requires extra care. Experimentally, detecting the transition point relies on measuring N_0, which in turn depends on the value of the trapping parameter α (define in Chapter 2) chosen for fitting the measured momentum distribution. Thus, we perform the analysis for a range of assumed values, α_f. We image clouds close to the critical point after $50 - 70\,\text{ms}$ of time-of-flight expansion from the trap. We vary T by changing the evaporation sequence, and the total atom number N by changing the initial loading of the trap. After forced evaporation we always raise the trap depth to $\sim k_\text{B} \times 0.4\,\mu\text{K}$, where evaporation is negligible, and hold the gas for another $1\,\text{s}$ to ensure thermal equilibration before ToF. We analyze the images by fitting the thermal wings using the assumed value α_f, and identify the critical point with the appearance of small BECs on top of the thermal profile, with $N_0 \leq 5000$. Both N and T at the critical point depend on the α_f used. We plot $N_c(T)$ and fit the data with a function of the form $N_c \propto T^{\alpha_c}$, deducing the best value for α_c from least-squares fitting. The bottom inset in Fig. 5.3 show α_c vs α_f. Self-consistency requires $\alpha_c = \alpha_f$, which is the case for $1.6 \lesssim \alpha_f \lesssim 1.7$. This suggests that our trap deviates slightly from the ideal box, with $\alpha = 1.65$ corresponding to $s = 20$. At the same time, the data agrees reasonably well with $\alpha_f = \alpha_c = 3/2$, as shown in the top inset of Fig. 5.3. Deviations from the ideal box can be alternately attributed to a slight variation of

the effective trapping volume V with temperature, $V \propto T^{\alpha-3/2}$. From *in situ* images, we indeed measure a $(20 \pm 10)\%$ increase in the cloud volume between $T = 25$ and 50 nK, which is consistent with our α.

We now turn to the absolute value of N_c. In line with the ideal box assumption, this is best described in terms of the critical phase space density $\rho_c = N_c \lambda_T^3 / V$. The data in Fig. 5.3 agrees with $\rho_c = 2.0 \pm 0.2$, while the LDA value is $\rho_c = 2.612$. With the finite size correction, we expect $\rho_c \approx 2.4$. The small remaining discrepancy is within our systematic uncertainties of 10% in N_c (resulting from the absolute number calibration described in Chapter 3) and 20% in V (volume measurements are described in Chapter 4).

5.2 Saturation of the thermal gas in a box

Next, we turn to studying partially condensed clouds. In Einsteins ideal-gas picture of condensation, N_{th} saturates at the critical point and can never exceed N_c. In a harmonically trapped gas, this picture is strongly violated even for weak interactions, such as in ^{87}Rb, and can be recovered only by extrapolating to the strictly noninteracting limit [76], where direct measurements cannot be performed due to the absence of thermal equilibrium [94]. This strong deviation from ideal-gas behavior arises due to an interplay of interactions and the nonuniformity of the gas, and can be explained by using a mean-field theory that does not require violation of the saturation picture at the level of the local thermal density [91].

While interactions have no effect in the critical point in a uniform system (within LDA), they can change the number of available thermal states when a condensate is present. We first consider the effects of mean-field interactions on the saturation in a uniform system, before turning to experimental measurements of N_{th} below the condensation point.

5.2.1 The Popov approximation

Within the LDA, we define the condensate and thermal densities, n_0 and n_{th}. A thermal atom experiences the mean-field energy $2\gamma n$, where $\gamma = \frac{4\pi\hbar^2 a}{m}$ and $n = n_0 + n_{\text{th}}$, while the condensate atoms are subject to the mean-field energy $\gamma n_0 + 2\gamma n_{\text{th}}$ [23]. Within the semi-classical Popov approximation, valid for all temperatures below (but not too close to) T_c [23, 95–99], the effect of interactions can be described

by a set of equations for n_0 and n_{th}:

$$\epsilon_a(\mathbf{p}) = \frac{p^2}{2m} + \gamma n_0, \tag{5.13}$$

$$\epsilon(\mathbf{p}) = \left[\epsilon_a^2(\mathbf{r}, \mathbf{p}) - (\gamma n_0)^2\right]^{1/2}, \tag{5.14}$$

$$\mu = \gamma n_0 + 2\gamma n_{\text{th}} + U, \tag{5.15}$$

$$n_{\text{th}} = \int g_0\left(e^{-\beta\epsilon(\mathbf{p})}\right) \frac{\epsilon_a(\mathbf{p})}{\epsilon(\mathbf{p})} \frac{\mathrm{d}^3\mathbf{p}}{(2\pi\hbar)^3}. \tag{5.16}$$

$$\tag{5.17}$$

These can be solved self-consistently for a range of μ using suitable numerical
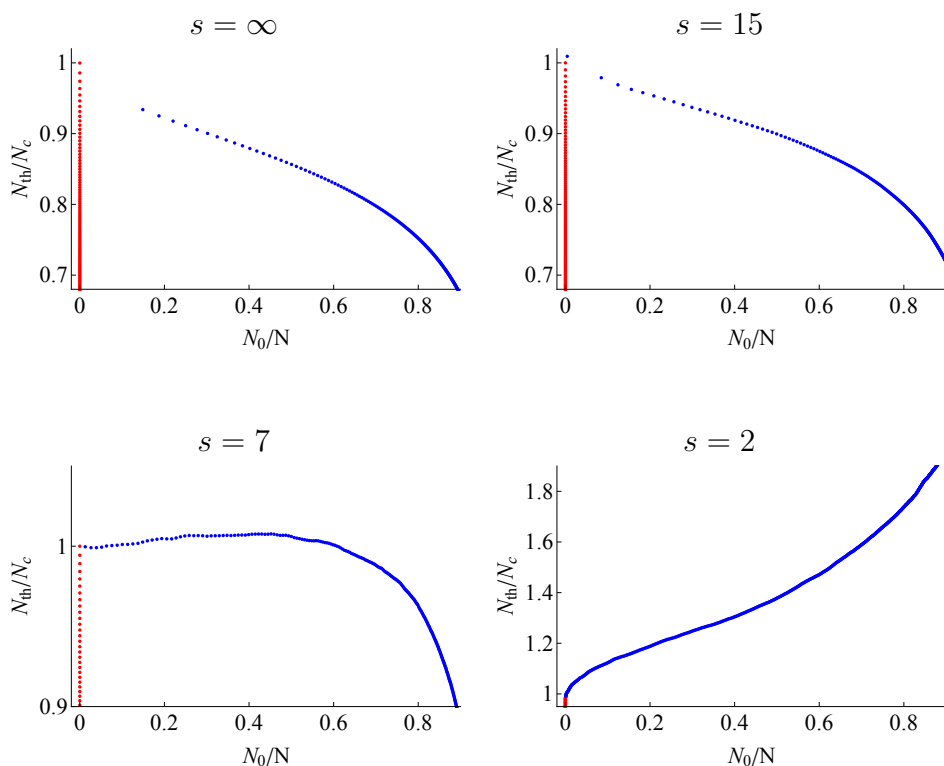
Figure 5.4: Numerical solutions of the Popov equation in different power-law potentials. We mark thermal clouds with atom number up to N_c (red) and partially condensed clouds with increasing condensate fraction (blue). N_{th} decreases with N_0 for large s and increases for small s. Only for $s \approx 7$ is the cloud saturated (note the different scale).

methods [100]. Once we have the μ-dependent LDA solution, we can easily determine N_0 and N_{th} for an arbitrary trapping potential $V(\mathbf{r})$ by integration. In Fig. 5.4 we show such solutions for a range of μ. An unfortunate feature of the equations above is that their solutions are discontinuous near the transition point, as seen in

the sudden increase in condensed fraction as μ exceeds 0. In any finite power-law potential, the discontinuity disappears, because the onset of condensation is not simultaneous throughout the trapping volume. In quasi-uniform traps ($s \gg 2$), the theory predicts a decrease in N_{th} as N_0 increases - in contrast to the $s = 2$ (harmonic) trap [28].

The dominating effect in a uniform potential is due to the modification to the dispersion relation due to the finite condensate density, as described by (5.14). This leads to a change in the density of states, and thus a decrease in the maximum thermal density. In a harmonic trap, on the other hand, the effect is geometric: the condensate, centered near the potential minimum, forces the thermal cloud into a "mexican-hat" potential, thus modifying the density of states in the opposite direction on a global rather than local level.

It has to be noted that the exact shape of the potential is irrelevant within the LDA - the saturation behaviour is determined by the volume distribution of trapping potential values, i.e. $P_U(u)\mathrm{d}u = \int \delta\left(U(\mathbf{r}) - u\right)\mathrm{d}^3\mathbf{r}\mathrm{d}u$. Thus, the effect of finitely steep walls is indistinguishable from floor noise of the same height in the central region of the trap.

Further, it has been shown [28, 76] that beyond-mean-field effects contribute significantly to the non-saturation in harmonic traps. Their influence in uniform traps is unclear and remains to be studied in the future.
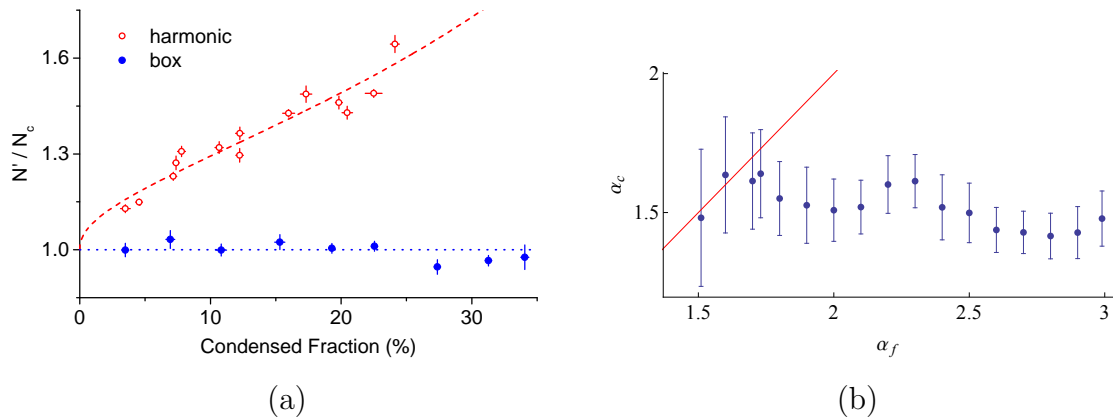
5.2.2 Experimental results

(a) (b)

Figure 5.5: (a) Saturation in a uniform Bose gas (adapted from [21]). The quasi-uniform clouds have $T_c = 45 \pm 1 \,\text{nK}$. The red data points were taken in the harmonic trap used to load our box, with $T \approx 110 \,\text{nK}$ and $N_c \approx 65 \times 10^3$. The dashed red line is the theoretical prediction from the previous section (also described in [16, 76]). (b) Self-consistency check for partially condensed clouds. For each α_f used for image analysis, we determine α_c from the fit $N_{\text{th}} \propto T^{\alpha_c}$ to the data (see text).

To study saturation, we use a variation of the experimental methods described in 5.1.2. First, we prepare degenerate samples with the condensate fraction of up to 40%. We then hold the cloud in the box trap at a constant temperature T. This is achieved by choosing a suitable box depth. Usually, our temperature is stable to $\pm 3\%$. We also post-select our data to exclude temperature outliers. As the atom number decays due to background collisions, we obtain clouds with a varying condensed fraction N_0/N. Consistently with 5.1.2, we analyze the data assuming $\alpha = 1.65$. We plot the results in Figure 5.5(a) (blue points).

It can be seen that the gas is saturated to within our experimental errors. Detecting the mean-field effects described above would require a significantly higher precision. For comparison, we show the strongly non-saturated thermal fraction in the harmonic trap, which shows significantly non-saturated behaviour.

Using our results for the critical atom number, saturation is equivalent to $N_{\text{th}} = N_c(T) \propto T^{\alpha}$. Having checked this scaling *at the transition*, we now want to confirm its validity *for all partially condensed clouds*. Again, we require self-consistency between the value α_f used for image analysis, and the value α_c providing best least-squares fit to the data. The result is shown in Figure 5.5 (b). We can see that the data are consistent with ideal uniform gas theory, while power-law potentials with
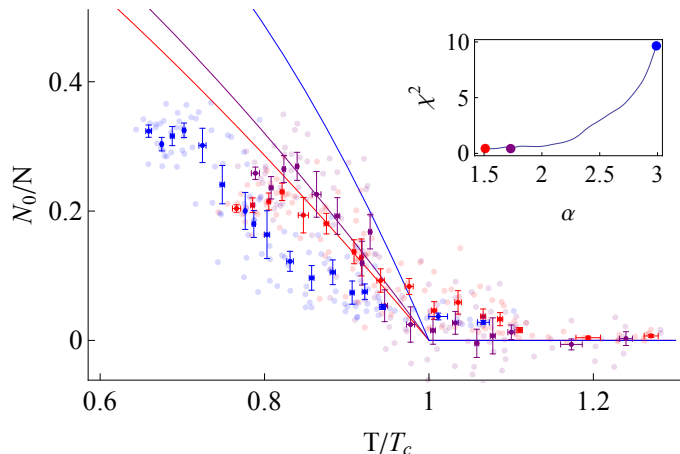
Figure 5.6: Condensed fraction of a partially condensed cloud in a quasi-uniform trap. We show data analyzed with $\alpha = 1.5$ (red), 1.73 (magenta) and 3 (blue). The data points and error bars are deduced from a running average (raw data shown in the background). Inset: χ^2 values for a range of α. $\alpha = 1.73$ produces excellent agreement, while $\alpha = 1.5$ is also very good.

$s < 15$ are strongly excluded.

A direct implication of saturation is the scaling of the condensed fraction with temperature [23]:

$$\frac{N_0}{N} = 1 - \frac{N_{\text{th}}}{N} = 1 - \frac{N_{\text{c}}}{N} = 1 - \left(\frac{T}{T_c}\right)^{\alpha}. \tag{5.18}$$

Keeping T_c constant while varying N_0 is impractical, but we can still define T_c for each N and plot the data accordingly. Again, we perform this analysis for different α. Varying α changes both the *data* and the *theoretical prediction*, and we require self-consistency between the two, as shown in Fig. 5.6.

Again, we see excellent agreement for $\alpha \leq 1.75$, seen both visually and by comparing χ^2. This is, of course, a direct consequence of the previously tested scaling of the critical number with temperature, and of saturation.

5.3   Energy and heat capacity

Next, we consider the energy E of the expanding condensate. The energy and its derivative, the heat capacity $C = \mathrm{d}E/\mathrm{d}T|_V$, are of particular interest as their behaviour near T_c changes qualitatively between uniform and harmonic systems: while C is continuous in uniform traps ($\alpha = 3/2$), it exhibits a discontinuity in harmonically trapped gases ($\alpha = 3$, and, in fact, for all $\alpha > 2$) [23]. ToF imaging

offers a way to extract the kinetic energy of the condensate in a model-free way. We will consider how this relates to the total energy, and quantify the role of interactions.

5.3.1 Theory

We start by considering an ideal gas. Using the results from Chapter 2, we can write the energy of a non-interacting Bose gas as a function T/T_c, in the spirit of (5.18):

$$\frac{E}{Nk_{\mathrm{B}}T} = \begin{cases} \alpha \frac{\zeta(\alpha+1)}{\zeta(\alpha)}\left(\frac{T}{T_c}\right)^{\alpha}, & \frac{T}{T_c} \leq 1 \\ \alpha \frac{g_{\alpha+1}(\mathcal{Z})}{g_{\alpha}(\mathcal{Z})}, & \frac{T}{T_c} > 1 \end{cases}. \tag{5.19}$$

Note that this energy term corresponds to the kinetic energy of the *thermal* atoms only (see below). In the case $\frac{T}{T_c} > 1$, $\mathcal{Z}$ has to be determined by numerically solving

$$g_{\alpha}(\mathcal{Z}) = \zeta(\alpha)\left(\frac{T}{T_c}\right)^{-\alpha}. \tag{5.20}$$

At high temperatures, we recover the well-known classical result $E = \alpha Nk_{\mathrm{B}}T$. E includes contributions from both kinetic and potential energy. In a typical experimental sequence, we switch off the external potential and let the cloud expand freely. Thus, only the kinetic energy is accessible in our measurements. The ratios of the kinetic and potential energies to the total energy E are given by the virial theorem:

$$E_{\mathrm{kin}} = \frac{3/2}{\alpha}E, \tag{5.21}$$

$$E_{\mathrm{U}} = \frac{\alpha - 3/2}{\alpha}E. \tag{5.22}$$

In the limit $\alpha \to 3/2$, we can thus measure the total energy of the cloud as E_{kin} ($E_{\mathrm{U}} = 0$).

Next, we consider the contribution due to mean-field interactions. Unlike the potential energy, the interaction energy E_{int} is converted into kinetic energy as the cloud expands. By writing $E_{\mathrm{int}}/Nk_{\mathrm{B}} = \gamma n/k_{\mathrm{B}}$, we estimate that the interaction energy per atom corresponds to $\sim 1\,\mathrm{nK}$ for 10^5 atoms in a typical trap. This contribution is negligible.

Finally, the kinetic energy of the *condensate* atoms is significantly smaller than E_{int} - a key assumption within the Thomas-Fermi approximation.

5.3.2 Extracting energy from ToF images

In 4.3, we explained how the momentum distribution of the cloud maps to the atomic density in ToF. We define the "point source" atomic density $n_{\infty}(\mathbf{r}, t) \equiv n(\mathbf{p} = m\mathbf{r}/t)$,

which describes the expansion from a trap of negligible size (or at large t), and the normalized *in situ* density $K(\mathbf{r})$. The kinetic energy can be expressed as the integral over the cloud's momentum distribution $n(\mathbf{p})$, or, equivalently, in terms of the second moment of $n_\infty(\mathbf{r})$:

$$E_{\text{kin}} = \frac{2m}{t^2} \int n_\infty(\mathbf{r}, t) r^2 \mathrm{d}^3\mathbf{r}. \tag{5.23}$$

For sufficiently steep trapping potentials and finite times, the atomic density after time t is given by the convolution

$$n(\mathbf{r}, t) = n_\infty(\mathbf{r}, t) * K(\mathbf{r}). \tag{5.24}$$

The second moment of the finite-t density distribution is *not* the sought energy. However, we can make use of a general theorem about the 2nd moment of the convolution [2] [101]: assuming all density distributions are centrally symmetric, we find the exact result

$$\int n(\mathbf{r}, t) r^2 \mathrm{d}^3\mathbf{r} = \int n_\infty(\mathbf{r}, t) r^2 \mathrm{d}^3\mathbf{r} \int K(\mathbf{r}) \mathrm{d}^3\mathbf{r} + \int n_\infty(\mathbf{r}, t) \mathrm{d}^3\mathbf{r} \int K(\mathbf{r}) r^2 \mathrm{d}^3\mathbf{r} \tag{5.25}$$

$$= \frac{t^2}{2m} E_{\text{kin}} + \int n_\infty(\mathbf{r}, t = 0). \tag{5.26}$$

Thus, correcting for the initial cloud size is possible by writing

$$E_{\text{kin}} = \frac{2m}{t^2} \left(\int n(\mathbf{r}, t) r^2 \mathrm{d}^3\mathbf{r} - \int n(\mathbf{r}, t = 0) r^2 \mathrm{d}^3\mathbf{r} \right). \tag{5.27}$$

At fixed N, the initial size correction grows quadratically with the linear size of the trap, and can be significant for larger boxes at typical ToFs.

Hidden direction

In practice, we can only measure the column density $\tilde{n}(x, y)$. We can thus extract the second moment w.r.t. x and y, but not z. Luckily, our trapping geometry possesses cylindrical symmetry around the $x = z = 0$ axis, and this gives $\int n(\mathbf{r}) z^2 \mathrm{d}^3\mathbf{r} = \int n(\mathbf{r}) x^2 \mathrm{d}^3\mathbf{r}$. For each term in (5.3.2), we can thus write

$$\int n(\mathbf{r}) r^2 \mathrm{d}^3\mathbf{r} = \int \tilde{n}(x, y)(2x^2 + y^2) \mathrm{d}x \mathrm{d}y. \tag{5.28}$$

In this form, we can extract the kinetic energy by direct summation over the optical density images.

---

[2] Generally, for $h = f * g$, the pth moment of h satisfies $m_p^{(h)} = \sum_{0 \le k \le p} \binom{p}{k} m_k^{(g)} m_{p-k}^{(f)}$. We use the special case $p = 2$, and $m_1 = 0$ for centrally symmetric distributions.

Correcting for residual potential curvature

Above, we have assumed that momentum $\mathbf{p}$ maps to position as $\mathbf{p} \to \mathbf{r} = (x, y, z) = t\mathbf{p}/m$. This is only true in absence of any external fields during ToF. As explained in 4.1.2, our gravity compensating setup introduces a harmonic trapping frequency $\omega_r \approx 1.6\,\mathrm{Hz}$ in the horizontal (y) direction[3]. Thus, the mapping is modified to $\mathbf{p} \to \mathbf{r} = (x', y', z')$ with $x' = x$, $y' = \mathrm{sinc}(\omega_r t)y$ and $z' = \mathrm{sinc}(\omega_r t)z$. The corrected expression for the kinetic energy thus becomes

$$
\begin{aligned}
E_{\mathrm{kin}} = & \frac{2m}{t^2} \int \tilde{n}(x, y, t) \left[2x^2 + \frac{y^2}{\sin(\omega_r t)} \right] \mathrm{d}x\mathrm{d}y - \\
& - \frac{2m}{t^2} \int \tilde{n}(x, y, t = 0) \left[2x^2 + y^2 \right] \mathrm{d}x\mathrm{d}y.
\end{aligned}
\tag{5.29}
$$

5.3.3 Results

We now use the optical density images from 5.2.2 to extract energies using (5.29). In practice, the noise far from the cloud center is amplified significantly due to the r^2 scaling. We thus replace the pixel values in the thermal wings outside the exclusion region (as defined in 4.3.3) by the best-fit model values to ensure convergence. At $t = 50\,\mathrm{ms}$, the correction to energy due to the residual harmonic trapping is $\approx 10\%$ in the x-direction. We plot the kinetic energy per particle against T/T_c in Fig 5.7, and compare it with the prediction (5.21). As in Fig. 5.6, the choice of α affects both the theory and the data. The E_{kin} plot indicates that the analysis is particularly sensitive to the value of α, and in fact excludes $\alpha = 3/2$ for the data set shown, giving an estimate for α very close to that obtained in 5.1.2.

Our data is also consistent with the prediction that the heat capacity is continuous. At the same time, it has proven challenging to detect the discontinuity in the first derivative of energy in harmonic condensates [102]. Another way to approach the problem is to note that $\mathrm{d}\mu/\mathrm{d}T = 0$ when C_V is continuous, and vice versa. However, determining μ from the shape of thermal clouds is extremely unreliable, and our data is not accurate enough to distinguish between μ approaching zero linearly and quadratically.

---

[3]Gravity compensation during long ToF is necessary due to the limited size of our CCD: the cloud falls outside the imaging area otherwise.
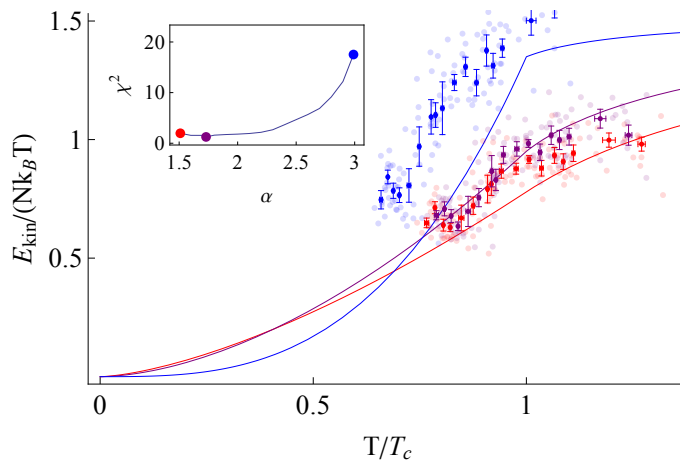
Figure 5.7: Kinetic energy of a Bose gas in a quasi-uniform trap. We show data analyzed with $\alpha = 1.5$ (red), 1.73 (magenta) and 3(blue). The data points and error bars are deduced from a running average (raw data shown in the background). Inset: χ^2 values for a range of α. $\alpha = 1.73$ produces excellent agreement, while $\alpha = 1.5$ is also very good.

5.4 Quantum Joule-Thomson effect in a Bose gas

Finally, we consider the long-time evolution of a partially condensed Bose gas held in the (uniform) box trap. We typically prepare clouds at $T_i \approx 45\,\mathrm{nK}$ in a trap of depth $U_0 \sim 10 - 20 k_\mathrm{B} T_i$, chosen such that evaporation is negligible. As the gas is held in the trap, atoms are slowly removed from the cloud, with an exponential time scale $\tau \approx 10\,\mathrm{s}$, by collisions with the background gas in the vacuum chamber. Because of low atomic density ($n < 5 \times 10^{12}\,\mathrm{cm}^{-3}$), the three-body recombination rate is negligible [30]. As N decays, the elastic collision rate (among the trapped atoms) remains sufficiently high for the gas to continuously reequilibrate on a time scale $\tau_\mathrm{eq} \lesssim 2\,\mathrm{s} \ll \tau$ [103]. Crucially, collisions with the background gas are independent of the energy of the trapped atoms, so the average energy per trapped particle, E/N, remains constant. Within the ideal-gas approximation, pressure is simply given by the energy density, so enthalpy H is simply proportional to E, and the specific enthalpy $h = H/N$ is a conserved quantity. The decay of the cloud is thus equivalent to the Joule-Thomson isoenthalpic rarefaction. In a classical ideal gas, h depends only on T, so temperature cannot change in an isoenthalpic process. This is, however, not true for a quantum degenerate ideal gas [104]. The resulting change in temperature in a Joule-Thomson process is known as the Joule-Thomson effect. We now show that the ideal Bose gas cools during isoenthalpic rarefaction, and

compare the effect with that seen in classical gases.

5.4.1 Joule-Thomson effect in partially condensed clouds

To include both ideal box and power-law traps in our description, we first recall the definition of enthalpy. In a uniform system, $H = E + pV$. While in a more general trap we have to replace p, V by a suitable pair of conjugate variables (with V describing the trapping geometry), we can always write $H = G + TS$, where $G = Nk_{\mathrm{B}}T\ln(\mathcal{Z})$ is the Gibbs free energy. Using results from Table 2.1, we find that

$$H = \frac{\alpha + 1}{\alpha}E. \tag{5.30}$$

In a uniform ideal gas, this also follows directly from $E = \frac{3}{2}pV$. Thus, keeping E/N constant does indeed correspond to an isoenthalpic process ($h = $ const). For partially condensed clouds, we can write

$$h = \frac{H}{N} \propto \frac{N_c k_{\mathrm{B}}T}{N} \propto \frac{T^{\alpha+1}}{N} = \mathrm{const}. \tag{5.31}$$

The last equation shows that, as N decreases, T follows a simple power law. This scaling is only valid while the condensed fraction is non-zero.

Consider a cloud with initial temperature T_{i}, total atom number N_{i} and *thermal* number $N_{\mathrm{th,i}}$. While isoenthalpy implies $N \propto T^{\alpha+1}$, the thermal number is saturated, and therefore $N_{\mathrm{th}} \propto T^{\alpha}$. The thermal fraction thus follows

$$\frac{N_{\mathrm{th}}}{N} \propto T \propto N^{1/(\alpha+1)}. \tag{5.32}$$

As the thermal fraction increases to 1, the condensate disappears. This happens when

$$\frac{N}{N_{\mathrm{i}}} = \left(\frac{N_{\mathrm{th,i}}}{N_{\mathrm{i}}}\right)^{\alpha+1}. \tag{5.33}$$

5.4.2 Experimental results

An experimental confirmation of the above scaling is shown in Fig. 5.8. We rescale temperatures and numbers to their values at the beginning of hold time. We show the evolution of a partially condensed sample (blue points, $N_i = 1.7 \times 10^5$, $T_i = 46\,\mathrm{nK}$) and a thermal sample (red points, $N_i = 0.7 \times 10^5$, $T_i = 52\,\mathrm{nK}$). Each point is obtained by averaging over five repeats of the experimental sequence. The data for partially condensed clouds is indistinguishable from the uniform-trap scaling $T \propto N^{1/2.5}$ (dashed blue line in the figure). While our theory describes the data
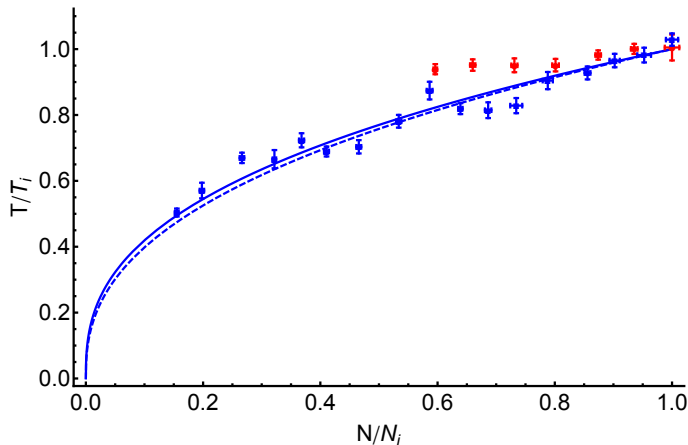
Figure 5.8: Quantum Joule-Thomson effect in a partially condensed (blue) and thermal (red) clouds. The solid and dashed blue lines are predictions of Eq. (5.31) with $\alpha = 1.65$ and $\alpha = 3/2$, respectively.

well, we have to address several features for completeness. First, our partially condensed clouds start with a condensed fraction of $30 \pm 5\%$. According to (5.33), the cloud should be purely thermal below $N/N_i = 40 \pm 6\%$, while we see continued cooling. Second, the thermal sample prepared with $N/N_c \lesssim 50\%$ also exhibits some cooling, which could be mis-interpreted as a consequence of evaporation. Thus, we must consider the isoenthalpic evolution of thermal samples, as well as the effect of external cooling (or heating).

5.4.3 Joule-Thomson cooling in a thermal Bose gas

It is instructive to recall the energy plot from Fig. 5.7, where we plotted (up to a constant factor) $E/(NT)$ vs. T/T_c. With $E/N = \text{const}$ and $T_c \propto N^{1/\alpha}$, this becomes a plot of $1/T$ vs. $T/N^{1/\alpha}$. As N decreases, the cloud is thus constrained by the energy curve in a way that requires an associated decrease in T, simply due to the fact that $E/(Nk_B T)$ increases with T/T_c as the fraction of particles with zero energy decreases. At very high temperatures, the cloud behaves classically and (in absence of interactions) the temperature remains constant along the isoenthalp.

Using the energy plot, we can predict the evolution of a thermal cloud by solving $E/N = E_i/N_i$ numerically. This allows us to extend our treatment to clouds both above and below condensation. We show the results of numerical calculations in Fig. 5.9 for the starting conditions corresponding to our two samples. Interestingly, while the condensate is depleted below $N/N_i \approx 0.45$, the deviation from (5.31) is minimal down to $N/N_i \approx 0.15$. Further, our parameter-free model correctly predicts
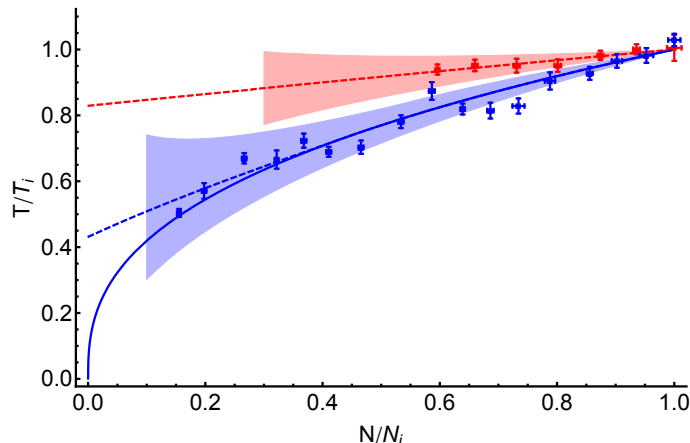
the slight cooling of the thermal sample.

Figure 5.9: Quantum Joule-Thomson effect in a partially condensed (blue) and thermal (red) clouds. The solid blue line is as in Fig. 5.8, while the dashed blue and red lines are numerical calculations described in the text. The shaded areas show the effect of heating or (evaporative) cooling between $\pm 5\,\mathrm{nK/lifetime}$ (see text).

5.4.4   Effect of heating and evaporation

The starting point of our treatment has been the assumption that loss of atoms from the trap is independent of their energy. This can be written as a rate equation of the form

$$\mathrm{d}E = \frac{E}{N}\mathrm{d}N. \tag{5.34}$$

We now seek to estimate potential contributions due to external heating (e.g. due to glancing collisions [103] or scattered trapping light) or cooling (due to evaporation). We add a heating term to the above equation and write

$$\mathrm{d}E = \frac{E}{N}\mathrm{d}N - \alpha N k_{\mathrm{B}}\tilde{T}\mathrm{d}N. \tag{5.35}$$

The last term corresponds to a constant heating rate per atom. Assuming that the atoms are lost on a time scale τ, we can write $\mathrm{d}N = -N\mathrm{d}t/\tau$, and a sample far from condensation (and thus with heat capacity $\alpha N k_{\mathrm{B}}$) would experience a change in temperature of $\tilde{T}$ in time τ. Solving this equation, we find

$$\frac{E}{N} = \frac{E_{\mathrm{i}}}{N_{\mathrm{i}}} - \alpha k_{\mathrm{B}}\tilde{T}\ln\left(\frac{N_{\mathrm{i}}}{N}\right). \tag{5.36}$$

This no longer describes isoenthalpic evolution, but allows us to extract T numerically, as described above. For partially condensed clouds, we find an analytic result

modifying (5.31):

$$\left(\frac{T}{T_\mathrm{i}}\right)^{\alpha+1} = \frac{N}{N_\mathrm{i}} - \frac{\tilde{T}}{T_\mathrm{i}}\frac{N}{N_\mathrm{th,i}}\ln\left(\frac{N}{N_\mathrm{i}}\right). \tag{5.37}$$

In Fig. 5.9, we show predictions derived from (5.36) for $-5\,\mathrm{nK} \leq \tilde{T} \leq 5\,\mathrm{nK}$ as shaded areas. This corresponds to heating rates between $\pm 0.5\,\mathrm{nK/s}$. It can be seen that our data strongly excludes higher heating (or cooling) rates. Especially for small N/N_i, we expect our data to be extremely sensitive to heating. At the same time, our temperature fits become less reliable due to decreasing optical densities of the clouds.

5.4.5 The Joule-Thomson coefficient

In classical gases, one commonly defines the Joule-Thomson coefficient

$$\mu_\mathrm{JT} = \left(\frac{\partial T}{\partial P}\right)_h. \tag{5.38}$$

For an ideal partially condensed Bose gas in a uniform trap, we can write

$$\mu_\mathrm{JT} = \frac{3}{2}V\frac{N}{E}\left(\frac{\partial T}{\partial N}\right)_h. \tag{5.39}$$

More conveniently expressed, the derivative of the scaling (5.31) (dashed blue line in Fig. 5.8) corresponds to [23]

$$\mu_\mathrm{JT} = \frac{2}{5\zeta(5/2)}\frac{\lambda_T^3}{k_\mathrm{B}}. \tag{5.40}$$

At our lowest temperatures, $\mu_\mathrm{JT} \approx 4\times 10^9\,\mathrm{K/bar}$, about 10 orders of magnitude larger than observed in classical gases.

To understand the origins of this enhancement, on dimensional grounds we write $\mu_\mathrm{JT} = c_\mathrm{JT}T/P$, so c_JT is dimensionless and $T/P \sim 1/(n_\mathrm{th}k_\mathrm{B})$, where n_th is the thermal particle density. The value of c_JT depends on the equation of state. In the ideal gas, $c_\mathrm{JT} = 0$ in the classical limit, while $c_\mathrm{JT} = 1/(\alpha+1)$ for a saturated partially condensed Bose gas. Interaction corrections to c_JT are essentially given by the ratio of interaction and thermal energy. In the partially condensed sample, we observe a drop in T by $\approx 22\,\mathrm{nK}$. Meanwhile, the interaction energy per particle is always smaller than $(8\pi\hbar^2 a/m)(N_\mathrm{i}/V)$, corresponding to under $4\,\mathrm{nK}$. The change in T therefore must predominantly be a purely quantum-statistical, rather than an interaction, effect. Moreover, note that for $a > 0$ the drop in the interaction energy should lead to slight heating rather than cooling of the gas. In our case

the interaction corrections are unimportant and $c_{\mathrm{JT}} \approx 2/5$, but for a classical gas they are the only origin of the JT effect and typically $c_{\mathrm{JT}} \lesssim 10^{-3}$. Another large enhancement of μ_{JT} comes from the fact that in a saturated gas $n_{\mathrm{th}} \sim \lambda_T^{-3} \sim T^{3/2}$ decreases with temperature, and our lowest n_{th} is $\sim 10^7$ times smaller than at ambient temperature and pressure. Combining the differences in c_{JT} and $1/n_{\mathrm{th}}$, we recover the $\approx 10^{10}$-fold increase in μ_{JT} compared to classical gases. It is also interesting to note that μ_{JT} in Eq. (5.40) explicitly vanishes in the limit $\hbar \to 0$, reiterating that this is a purely quantum effect.

On a final note, the sign of μ_{JT} in a bosonic gas is opposite to that in an ideal Fermi gas [105].

Chapter 6

Spectroscopic Studies of a Uniform BEC

Time-of-flight imaging allows measurements of the momentum distribution of weakly interacting thermal atoms in a partially condensed cloud, and is the standard technique for BEC thermometry. However, this method can not be applied to study the BEC ground state in momentum space for two reasons: first, the achievable resolution is limited by our imaging system (see 3.6), and second, the momentum distribution evolves during the time of flight due to both interactions and the residual external fields (see 5.3.2). An alternative measurement technique described in this Chapter is Bragg spectroscopy.

Bragg scattering of atoms by a standing light wave [106, 107] is a fundamental prediction of quantum theory. Following the observations of light scattering by atomic lattices, i.e. crystals [108], as well as scattering of massive particles by atomic lattices [109], it strikingly complemented other evidence for wave-particle duality.

Following the demonstration of Bose-Einstein condensation, experimental focus shifted from the scattering of atomic beams by a standing wave towards the scattering of stationary ultra-cold atoms by a moving optical lattice [110–112].

Bragg spectroscopy has allowed measurements of the relative occupation of the different momentum states in a degenerate gas [110] as well as the dynamic structure factor [111]; it has also been used to directly measure the dispersion relation over a wide range of momenta [113–115].

In a harmonically trapped condensate, the broadening of the Bragg spectrum due to mean-field interactions exceeds by far the momentum width of the condensate wave-function [110]. We shall see that this is not the case in our uniform BECs,

allowing a direct measurement of the momentum occupation function. We start by developing a theoretical description of Bragg spectroscopy for large recoil momenta, before presenting our measurements.

6.1 Theory of Bragg spectroscopy

In this chapter we present measurements of the momentum distribution of quasi-pure uniform BECs using Bragg scattering. Bragg-scattered atoms separate from the stationary BEC in time-of-flight if the recoil momentum acquired by scattered atoms, q_r, exceeds the width of the BEC in momentum space, $\Delta p \sim \hbar/L$. At the same time, having a smaller recoil momentum improves the momentum resolution. The Bogoliubov dispersion relation predicts essentially free-particle behaviour at momenta $\gtrsim \hbar/\xi$, where ξ is the healing length ($\sim 1.5\,\mu\mathrm{m}$ for 10^5 atoms in a typical box trap). Thus, we choose $q_\mathrm{r} > \hbar/\xi > \hbar/L$ to be able apply the free-particle dispersion relation. On the other hand, measurements of the Bogoliubov spectrum in future experiments would require $\hbar/\xi > q_\mathrm{r} > \hbar/L$. In the measurements described in this Chapter, $q_\mathrm{r} \approx m \times 3\,\mathrm{mm/s} \sim \hbar/(0.2\,\mu\mathrm{m})$ - about an order of magnitude higher than $\hbar/\xi$. As we shall demonstrate below, the recoil momentum is mainly determined by the beam geometry. In our system, this means that the range of achievable q_r is limited by the optical access available in our vacuum system.

We start by considering the interaction of atoms in the condensate with two Bragg beams intersecting at an angle of 2θ (see Fig. 6.6 and Fig. 6.7 below). Assume the two beams have wave vectors $\mathbf{k}_1$ and $\mathbf{k}_2 = \mathbf{k}_1 - \mathbf{k}_\mathrm{r}$ and frequencies f_1 and $f_2 = f_1 - f$. The fractional frequency difference $f/f_j = k_\mathrm{r}/k_j$ is minimal (for $780\,\mathrm{nm}$ light it is typically $\sim 1\,\mathrm{kHz}/384\,\mathrm{THz} = 2.6 \times 10^{-12}$). We can write $k = k_1 \approx k_2$,and k_r is determined by the intersection angle 2θ:

$$k_\mathrm{r} = 2k\sin(\theta). \tag{6.1}$$

The corresponding recoil momentum acquired by an atom absorbing a photon from beam one and re-emitting a photon into beam two is given by

$$q_\mathrm{r} = \hbar k_\mathrm{r} \propto \sin(\theta). \tag{6.2}$$

Consider an atom with initial momentum $\mathbf{p}_\mathrm{i}$ and energy E_i. The scattered atom has momentum $\mathbf{p}_\mathrm{f} = \mathbf{p}_\mathrm{i} + \mathbf{q}_\mathrm{r}$, and thus energy

$$E_\mathrm{f} = \frac{p_\mathrm{f}^2}{2m} = E_\mathrm{i} + E_\mathrm{r} + \frac{\mathbf{p}_\mathrm{i} \cdot \mathbf{q}_\mathrm{r}}{m}, \tag{6.3}$$
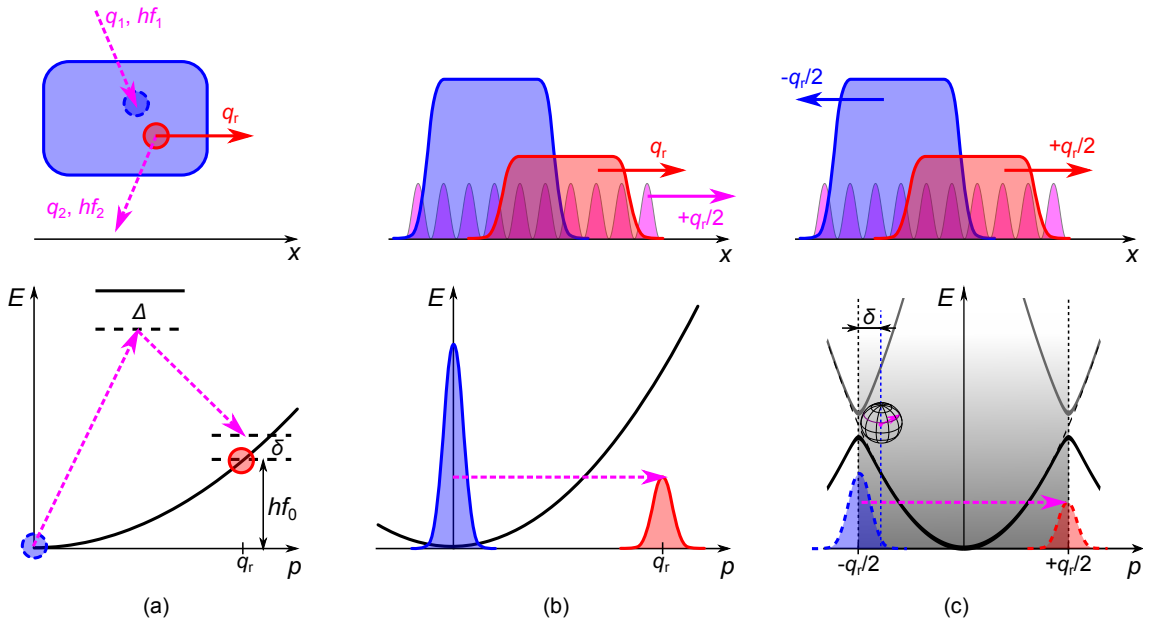
Figure 6.1: Left to right: three equivalent theoretical descriptions of Bragg scattering in real space (top) and in momentum space (bottom). (a) Single-atom picture. An atom undergoes a Raman transition by scattering a photon from beam 1 into beam 2 (top). Energy and momentum conservation must be satisfied in the transition (bottom). Both beams are far from resonance ($\Delta \gg f_0, \delta$). Detuning δ is due to the Doppler shift *or* frequency shift $f_1 - f_2 - f_0$ (see text). (b) Schrödinger picture in the lab frame. Two crossed beams create a moving lattice (top). This can be seen as a time-dependent perturbation, causing scattering between momentum eigenstates, $0 \to q_r$ (bottom). (c) Schrödinger picture in the stationary lattice frame. The condensate is initially moving left, and is Bragg-reflected by the lattice (top). In the free-particle basis, momentum changes by q_r (dashed lines, bottom). In the basis of Bloch eigenstates, the momentum is restricted to the first Brillouin zone (shaded), and remains unchanged. We show the first two bands of the dispersion relation. Bragg scattering is described by the free evolution of the Bloch vector in the two-state basis, with the level splitting given by the band gap. Resonance condition ($\delta = 0$) corresponds to the initial momentum being on the edge of the Brillouin zone (see text).

with recoil energy $E_r \equiv q_r^2/(2m)$. The transition is resonant when the photon energy difference equals

$$hf = hf_0(\mathbf{p}_i) \equiv E_r + \frac{\mathbf{p}_i \cdot \mathbf{q}_r}{m} \tag{6.4}$$

The change in E and p due to the two-photon process is shown in Fig. 6.1 (a). We define the detuning $\delta \equiv f - f_0$. As can be seen from the above resonance condition, the detuning can be seen to arise due to either the Doppler shift [second term in

(6.4)] or the change in frequency f.

6.1.1 Raman picture

To calculate the transition rates for a particular δ, we must address the atomic nature of the process. Bragg scattering is effectively a Raman transition - both photons are off-resonant, and the two-photon transition occurs via a *virtual* level, as indicated by a dashed line in Fig. 6.1 (a). Thus, the transition can be described by a single effective Rabi frequency [41]

$$\Omega = \frac{\Omega_1 \Omega_2}{2\Delta} = \frac{I}{I_{\text{sat}}} \frac{\Gamma^2}{4\Delta}, \tag{6.5}$$

where $\Omega_1 = \Omega_2$ are the Rabi frequencies of the single-photon transitions, Δ is the detuning of the individual beams from the atomic transition, $I = I_1 = I_2$ is the intensity in each beam, I_{sat} is the saturation intensity and Γ the linewidth of the atomic transition. Thus, after subjecting the atoms to the Bragg beams for time τ, we expect the transferred fraction to be

$$P(\mathbf{p}_i \to \mathbf{p}_i + \mathbf{q}_r) = \frac{\Omega^2}{\Omega^2 + \delta^2} \sin^2 \left(\frac{1}{2} \sqrt{\Omega^2 + \delta^2} \tau \right), \tag{6.6}$$

$$\text{with} \quad \delta = f - f_0(\mathbf{p}_i). \tag{6.7}$$

Next, we extend our treatment to a cloud with the momentum distribution $|\Psi(\mathbf{p})|^2$ (Fig. 6.1 (b), bottom panel). We can predict the total number of transferred atoms by integrating over all momenta; with the momentum wavefunction $\Psi(\mathbf{p})$ normalized to N, we expect the number of Bragg-diffracted atoms to be

$$N_{\text{B}} = \int |\Psi(\mathbf{p}_i)|^2 P(\mathbf{p}_i \to \mathbf{p}_i + \mathbf{q}_r) \mathrm{d}^3 \mathbf{p}_i. \tag{6.8}$$

The integrand depends on the component of $\mathbf{p}$ parallel to $\mathbf{q}_r$ only. The Doppler shift term in (6.4) suggests that we can write momentum in *Bragg frequency units* via

$$\tilde{p} = \frac{q_r}{hm} p. \tag{6.9}$$

Similarly, we introduce the recoil frequency $f_r = E_r/h$. Expression (6.8) becomes a convolution:

$$N_{\text{B}}(f) = \left(\frac{\Omega \tau}{2} \right)^2 \int |\Psi|^2(\tilde{p}) \times \mathrm{sinc}^2 \left(\frac{1}{2} \sqrt{\Omega^2 + (f - f_r - \tilde{p})^2} \tau \right) \mathrm{d}\tilde{p}. \tag{6.10}$$

So far, we have considered population transfer (wavefunction amplitudes) only, using equations (6.5) and (6.6). These are standard results of time-dependent perturbation theory, and make use of the rotating wave approximation. Within the same

framework, it is possible to find the phase evolution of each plane-wave eigenstate, and thus the evolution of $\Psi(p)$ during the Bragg pulse. We shall obtain these results using a different approach, highlighting similarities with optical lattice experiments and Bragg scattering in solid state physics.

6.1.2 Moving lattice picture

It is instructional to consider the (classical) light field created by the two beams. Representing both beams by plane waves with equal amplitudes ε, and assuming the polarization vectors of the two beams are parallel, we can write

$$E_j = \varepsilon e^{i(\mathbf{k}_j \cdot \mathbf{r} - \omega_j t)} \quad \text{with} \quad j = 1, 2, \tag{6.11}$$

$$E = E_1 + E_2 = 2\varepsilon e^{i\left(\frac{\mathbf{k}_1 + \mathbf{k}_2}{2} \cdot \mathbf{r} - \frac{\omega_1 + \omega_2}{2} t\right)} \cos\left(\frac{\mathbf{k}_2 - \mathbf{k}_1}{2} \cdot \mathbf{r} - \frac{\omega_2 - \omega_1}{2} t\right). \tag{6.12}$$

Expression (6.12) can be seen to represent an optical field with the slowly moving envelope

$$|E| = 2\varepsilon \cos\left(\frac{1}{2}(\mathbf{k}_r \cdot \mathbf{r} - 2\pi f t)\right), \tag{6.13}$$

with $\mathbf{k}_r = \mathbf{q}_r / \hbar$. The rotating wave term (the phase term in E) is off-resonant, and we can describe the effect on the Hamiltonian by the AC Stark shift potential (3.5.3), which is proportional to the single-beam light intensity $I \propto \varepsilon^2$. This is of the form

$$U(\mathbf{r}, t) = \hbar \frac{I}{I_{\text{sat}}} \frac{\Gamma^2}{4\Delta} \times 4\cos^2\left(\frac{1}{2}(\mathbf{k}_r \cdot \mathbf{r} - 2\pi f t)\right). \tag{6.14}$$

Comparing with (6.5), we can write:

$$U(\mathbf{r}, t) = \frac{\hbar\Omega}{2}\left[1 + \cos\left(\mathbf{k}_r \cdot \mathbf{r} - 2\pi f t\right)\right]. \tag{6.15}$$

We see that the potential is that of a moving 1D optical lattice with amplitude $\hbar\Omega$, as shown in Fig. 6.1 (b) (top panel). The lattice period is $\Lambda = 2\pi/k_r$, and the lattice velocity is $v_l = 2\pi f / k_r$. By changing the frequency detuning f alone, we can vary the lattice velocity, and even simulate BECs in accelerating frames [116, 117].

6.1.3 Bloch picture

Consider atoms initially at rest in the lab frame ($p_i = 0$). The resonance condition (6.4) simplifies to $f_0 = E_r$, and the lattice velocity becomes $v_l = v_r/2$, where $v_r = q_r/m$ is the recoil velocity. Upon scattering, the resonant atoms acquire *twice* the lattice velocity. This result is obvious in a frame of reference where the lattice is

stationary: in this moving frame, the atoms, initially moving at $-v_\mathrm{r}/2$, are reflected by the lattice and acquire an opposite velocity of $v_\mathrm{r}/2$, as shown in Fig. 6.1 (c).

In the lattice frame, we can treat the lattice as a time-independent perturbation to the free-particle Hamiltonian. Moreover, it is periodic, and in our case contains only few Fourier components:

$$U(x) = \sum_{G \in \mathbb{Z}k_\mathrm{r}} u_G e^{iGx} \tag{6.16}$$

$$\text{with} \quad u_{-k_\mathrm{r}} = u_{k_\mathrm{r}} = u = \frac{\hbar\Omega}{4}. \tag{6.17}$$

The eigenstates of the periodic Hamiltonian can be found explicitly. These are given by the Bloch functions [118] of the form

$$\Phi(x) = \sum_{G \in \mathbb{Z}k_\mathrm{r}} c_{k+G} e^{i(k+G)x} \tag{6.18}$$

The lattice momentum k is restricted to the first Brillouin zone, $-k_\mathrm{r}/2 \leq k \leq k_\mathrm{r}/2$. The coefficients c, as well as the energies ϵ, can be determined from the Schrödinger equation, which takes the form

$$(\epsilon_k - \epsilon)c_k + \sum_{G \in \mathbb{Z}k_\mathrm{r}} u_G c_{k+G} = 0, \tag{6.19}$$

with $\epsilon_k = \hbar^2 k^2/(2m)$. Because u_G is only non-zero when $G = \pm k_r$, the Hamiltonian is tridiagonal in matrix notation, with coupling between k and $k \pm k_\mathrm{r}$ states only. In practice, we only need to consider a small number of k. Initially, only k-states close to $-k_\mathrm{r}/2$ are occupied. First-order transition can be describe by including states with momenta k and $k + k_\mathrm{r}$ only. Including other k is equivalent to considering four-photon (and higher-order) transitions.

Expressing momenta in units of $k_\mathrm{r}/2$ and energies in units of $E_\mathrm{r}/4 = (k_\mathrm{r}/2)^2/(2m)$, the Hamiltonian (for $k < 0$) takes the form

$$H = \begin{pmatrix} k^2 & u \\ u & (k+2)^2 \end{pmatrix}, \tag{6.20}$$

with eigenenergies

$$\epsilon_\pm = k^2 + 2\left(k + 1 \pm \sqrt{\frac{u^2}{4} + (k+1)^2}\right) \tag{6.21}$$

and eigenvectors

$$\begin{pmatrix} c_1^\pm \\ c_2^\pm \end{pmatrix}. \tag{6.22}$$

These corresponds to the first two Bloch bands, with wavefunctions

$$\Phi_\pm(x, t = 0) = c_1^\pm e^{ikx} + c_2^\pm e^{i(k+k_{\mathrm{r}})x} \tag{6.23}$$

Now, we can describe the time evolution of the BEC wavefunction in the Bloch basis. The Bloch states evolve freely in time, according to[1]

$$\Phi_\pm(x, t) = \Phi_\pm(x, 0)e^{-i\epsilon_\pm t}. \tag{6.24}$$

The BEC wavefunction in the lab frame, $\Psi(k)$, transforms to the stationary-lattice frame as $\Phi(k) = \Psi(k + k_0)$, where $\hbar k_0 = -mv_l$ is the momentum acquired by the atoms upon the Galilean transformation, which relates to the previously defined detuning in the Raman picture via $(k_0 - k_{\mathrm{r}})/k_{\mathrm{r}} = \delta/f_0$. After substituting v_l in suitable units, the band gap near the Brillouin zone boundary takes the familiar form $\epsilon_+ - \epsilon_- = \frac{1}{2}\sqrt{\Omega^2 + \delta^2}$. We can invert (6.23) to write the initial state as

$$\Phi(x, 0) = \int \Phi(k)e^{ikx}\mathrm{d}k = \int \Phi(k) \left[c_1^- \Phi_-(x, 0) + c_1^+ \Phi_+(x, 0) \right] \mathrm{d}k. \tag{6.25}$$

Subsequent evolution is described by

$$\Phi(x, t) = \int \Phi(k) \left[c_1^- \Phi_-(x, t) + c_1^+ \Phi_+(x, t) \right] \mathrm{d}k \tag{6.26}$$

$$\Rightarrow \quad \Phi(x, t) = \int \Phi(k) \left[(c_1^-)^2 e^{-i\epsilon_- t} + (c_1^+)^2 e^{-i\epsilon_+ t} \right] e^{ikx}\mathrm{d}k$$
$$+ \int \Phi(k) \left[c_1^- c_2^- e^{-i\epsilon_- t} + c_1^+ c_2^+ e^{-i\epsilon_+ t} \right] e^{i(k+q_{\mathrm{r}})x}\mathrm{d}k \tag{6.27}$$

The second term in (6.27) describes the growth of the scattered cloud. Its norm corresponds to the diffracted atom number,

$$N_{\mathrm{B}} = \int |\Phi(k)|^2 \left| c_1^- c_2^- e^{-i(\epsilon_+ - \epsilon_-)t} + c_1^+ c_2^+ e^{-i\epsilon_+ t} \right|^2 \mathrm{d}k. \tag{6.28}$$

This result turns out to be equivalent to (6.10). The key assumption in both cases was that we consider first-order transitions between k-states separated by k_{r} only. In the Raman picture, we have neglected coupling via 4 and more photons, and in the Bloch picture we have considered the two lowest bands only. The Bloch picture has the advantage that it exposes a convenient basis that can be used as a starting point for e.g. describing the effect of interactions. While we considered an infinite lattice (neglecting the effect of box walls), the treatment can also be extended to finite lattices [119].

---

[1]We set $\hbar = 1$ for ease of notation

6.1.4 Condensate wavefunction in momentum space

As shown above, Bragg spectroscopy naturally maps momentum p to frequency $f = f_0 + \frac{q_r}{hm}p$. The momentum distribution $|\Psi(p)|^2$ maps to the scattered atom number $N_B(f)$, which is always broadened due to the finite effective linewidth of the transition, as described by the convolution (6.10). The minimum achievable linewidth is of the order of Ω (see below). For small enough Ω and long enough τ, we expect this broadening to be minimal, and we recover the condensate wavefunction. We start by considering how this wavefunction depends on interatomic interactions.

In a box of length L, several possible cases are conceivable: first, if the mean-field energy is very low, the condensate will be described by the non-interacting "particle in a box" groundstate. If, on the other hand, the condensate is in the Thomas-Fermi regime, we expect the wavefunction to be approximately a top-hat function. The corresponding momentum distribution is then simply a sinc^2 function, $S(L)$, of zero-to-zero width $2v_r/L$ (in Bragg frequency units). In the intermediate regime, we must consider the non-uniformity of the condensate within the healing length ξ from the walls. In Figure 6.2 (a) we show the probability density $|\Psi|^2(x)$ for the three cases ($\xi = 0, 0.1, \infty$). For $\xi \lesssim 0.2$, the deviations of the wavefunction from the uniform case are limited to the box edges, were the wavefunction follows $\Psi(x) \propto \tanh\left(\frac{x}{\sqrt{2}\xi}\right)$ [23]. We apply the Fourier transform to the analytic representation of $\Psi(x)$ thus obtained, and plot the momentum distribution $|\Psi(k)|^2$ in Fig. 6.2 (b). In our studies,
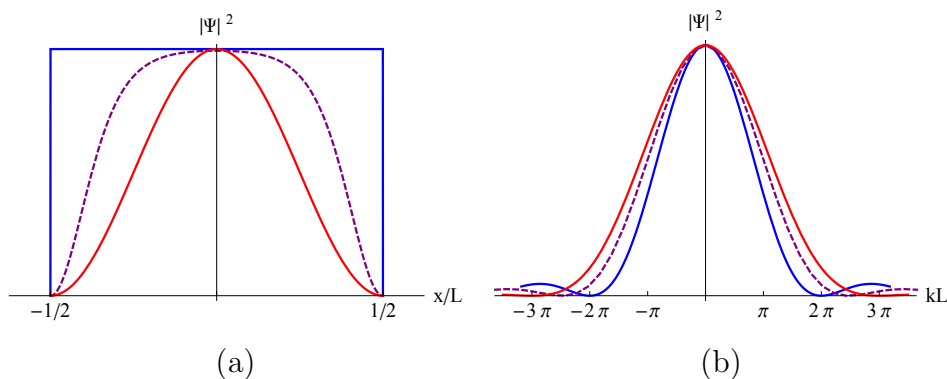

Figure 6.2: Wavefunction in real space (a) and momentum space (b) for a non-interacting BEC (red), and for an interacting BEC with $\xi = 0$ (blue) and $\xi = 0.1L$ (purple, dashed).

we seek to quantify the width of the momentum distribution of our condensate. A

common way is to consider the root-mean-squared (RMS) width, given by

$$\text{RMS}^2 = \frac{\int k^2 |\Psi(k)|^2 \mathrm{d}k}{\int |\Psi(k)|^2 \mathrm{d}k} \propto E_{\text{kin}}. \tag{6.29}$$

Unfortunately, this is infinite for a perfectly uniform condensate with sharp walls. We plot the change in the RMS width with ξ in Fig. 6.3 (a). It is easy to show that the kinetic energy density term is proportional to $1/\xi^2$ over a region of space of the width $\sim \xi$, meaning that the kinetic energy scales as $1/\xi$ for $\xi \ll L$. We demonstrate this asymptotic behaviour in the inset in Fig. 6.3 (a). The extreme sensitivity to ξ, as well as the noise issues associated with extracting the second moment from the distribution's wings, make it unsuitably for quantitative studies. While the distribution wings decay slowly, the width of the central peak in the
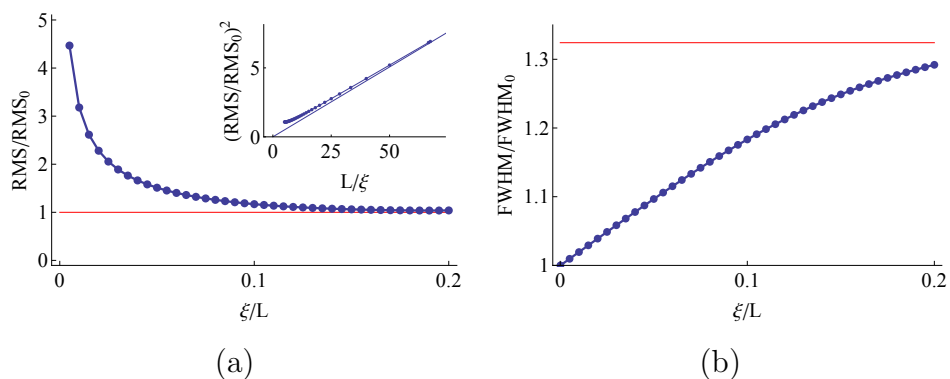

Figure 6.3: Measuring the width in momentum space: (a) root-mean-square width (rms), and (b) full width at half-maximum (fwhm) for different ξ/L. Red lines indicate result for the non-interacting wavefunction. Inset in (a) shows that the energy of the condensate ($\propto$ rms width squared) increases as $1/\xi$ for small ξ (see text).

momentum distribution is well-behaved. We quantify this using the full width at half-maximum (FWHM). Fig. 6.3 (b) shows that the variations in the FWHM is $\sim 30\%$ between $\xi = 0$ and $\xi = \infty$, with deviations from the ideal box on the order of a few % in the experimentally relevant range.

The effect of finite wall steepness is similar to that of finite ξ. Generally, our imaging resolution ($\sim 5\%$ in box length) is sufficient to distinguish $\xi = 0$ from $\xi = \infty$, but it will largely mask the smaller effects of non-zero ξ and finite wall width.

6.1.5 Effect of Rabi frequency and pulse length

Next, we consider the broadening of the measured momentum distribution during Bragg spectroscopy, as described by the convolution kernel in (6.10). For small Rabi frequencies ($\Omega\tau \ll 1$), and thus small scattered fraction ($N_{\mathrm{B}}/N \ll 1$), the convolution kernel is a sinc^2 with zero-to-zero width of $2/\tau$ in frequency units. However, even for large τ, we expect the measured momentum distribution to be broadened by $\sim \Omega$. The measured Bragg spectrum for a given box length, $\tilde{S}(L)$, will therefore deviate from the Heisenberg-limited spectrum $S(L)$. An illustration is shown in Fig. 6.4.
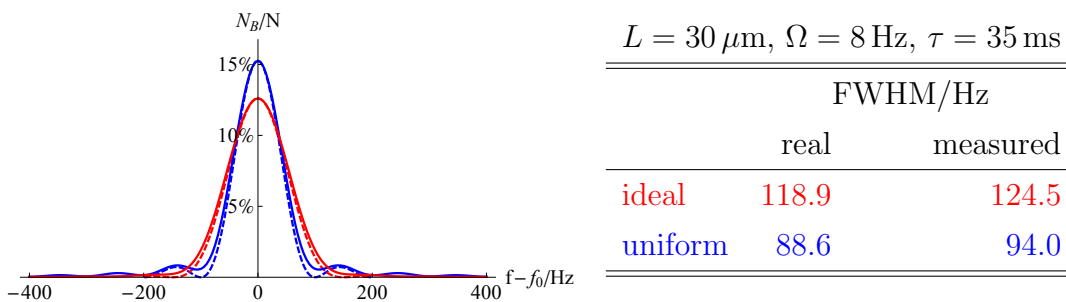

$L = 30\,\mu\mathrm{m}$, $\Omega = 8\,\mathrm{Hz}$, $\tau = 35\,\mathrm{ms}$		
	FWHM/Hz	
	real	measured
ideal	118.9	124.5
uniform	88.6	94.0

Figure 6.4: Broadening of the measured momentum distribution in Bragg spectroscopy. We show the transfer fraction $N_{\mathrm{B}}(f)/N$ vs f for ideal (non-interacting, red) and uniform (Thomas-Fermi, blue) BECs. Dashed lines are Heisenberg-limited momentum spectra S in frequency units, solid lines are predicted experimental spectra $\tilde{S}$ calculated using (6.10). The FWHM is tabulated for each of the four spectra shown.

To minimize the broadening, we should therefore use the smallest possible Ω. The transferred fraction at resonance scales $\sim (\Omega\tau)^2$, and we are thus forced to increase τ to obtain a detectable signal. While this approach works well for stationary clouds, the pulse length τ limits the time resolution when performing spectroscopy on freely expanding clouds, or studying time dependence in general. It is intuitively clear that short Bragg pulses will lead to excessive broadening for $\tau \lesssim L/v_{\mathrm{r}}$, e.g. 10 ms for a 30 μm box. We demonstrate this dependence in Fig. 6.5, where we plot the broadening of the Thomas-Fermi momentum distribution versus τ while keeping $\Omega\tau$ same as in Fig. 6.4.

The choice of suitable τ and Ω will ultimately depend on the required time resolution and the detectable scattered fraction, as limited by the initial atom number and the signal-to-noise ratio in the imaging system. While the broadening can not be fully eliminated in our system, the theoretical understanding developed in the preceding sections provides us with a quantitative, no-free-parameters model of the
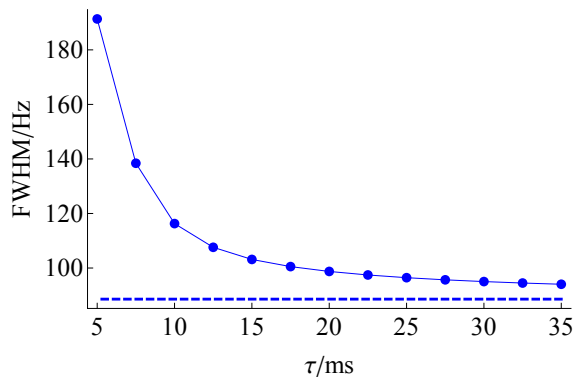
Figure 6.5: FWHM after Bragg spectroscopy vs τ for a uniform (strongly interacting) cloud, computed using (6.10). $L = 30\,\mu\text{m}$, $\Omega\tau = 8\,\text{Hz} \times 35\,\text{ms}$. For large τ, the broadening does not disappear, but approaches a constant $\sim \Omega$.

Bragg spectroscopy precess. Both τ and Ω are well known in our experiments, the latter from direct measurements of Rabi oscillations on resonance.

6.1.6 The mean-field shift

So far we have considered the effect of interactions on the condensate wavefunction only. However, interactions will also affect the Bragg spectroscopy process. As a direct consequence of the bosonic exchange symmetry, an atom scattered out of a BEC will experience *twice* the mean-field energy compared to an atom in the condensate ground state - often described as the "bosonic factor of two" [23]. This changes the energy conservation condition (6.4) to

$$hf = hf_0(\mathbf{p}_\text{i}) + \gamma n_0, \tag{6.30}$$

with $\gamma = 4\pi\hbar^2 a/m$ and $n_0 = N_0/V$. The same result can be obtained by considering the Taylor expansion of the Bogoliubov dispersion relation at large momenta.

For a typical box ($L = 30\,\mu\text{m}$, $R = 16\,\mu\text{m}$), this shift equals $32\,\text{Hz}$ for each 10^5 atoms in the condensate. The Bragg spectroscopy peak will therefore be centered on $f_\text{c} = f_\text{r} + \gamma n_0$. Bragg spectroscopy can thus be used to measure the mean-field energy of a uniform BEC directly. In a non-uniform system, on the other hand, the mean-field shift varies spatially due to variations in density. This can lead to broadening of the spectroscopic peak, which in harmonic BECs has been seen to greatly exceed the Heisenberg width [110].

Note that n_0, and thus the shift (6.30), changes as n_0 changes during the Bragg pulse itself - another reason to keep Ωt small, and introduce suitable corrections.

6.1.7 Time evolution and the GPE

Finally, we briefly mention the time evolution of freely expanding clouds, and especially their width in momentum space. The Thomas-Fermi approximation states that the in-trap kinetic energy is negligible compared to the interaction energy. However, the interaction energy is converted into kinetic energy upon expansion. It is easy to see that the kinetic energy acquired per particle will be proportional to the in-trap density. Unlike for BECs in harmonic traps [120], we are not aware of an analytic form describing the expansion of a BEC from a cylindrical box trap. The temporal evolution of the condensate wavefunction is described by the Gross-Pitaevskii (GP) equation [23]:

$$i\hbar\frac{\mathrm{d}\Psi}{\mathrm{d}t} = -\frac{\hbar^2}{2m}\nabla^2\Psi + U\Psi + \gamma|\Psi|^2\Psi \qquad (6.31)$$

As described above, the non-interacting part of the Hamiltonian is best solved in momentum space, while the interacting part has to be solved in real space. We thus employ a split-operator method, implemented by Alexander Gaunt. This provides numerical results for the real-space as well as momentum wavefunction of the condensate after different expansion times. Combining the momentum wavefunction obtained by integrating the GP equation with our model of the Bragg transfer process [equation (6.10], we can obtain a theoretical prediction for the width of the Bragg spectrum, while considering the peak density of the cloud in real space allows us to predict the mean-field shift of the Bragg peak. This proves extremely useful in analyzing our experimental results, as shown below.

6.2 Experimental setup

To perform Bragg spectroscopy, we split a beam derived from the 780 nm repump laser in two parts (affectionately referred to as "Henry" and "Lawrence"), as shown in Fig. 6.6. The beams are thus detuned by 6.8 GHz from the nearest resonant transition. Each beam passes through an AOM, and the frequency of one of the AOMs is adjustable. Although the coherence length of our laser source is typically on the order of meters, we took care to keep both optical paths (from the polarizing beam splitter to the atoms) equal in length to within a centimeter. Finally, both beams are intersected at an angle of $2\theta \approx 30°$, giving a recoil velocity of $v_\mathrm{r} \approx 3$ mm/s. Each beam is collimated to a width of approximately 3 mm, making the individual beam size, as well as the intersection region of the two beams, much larger than
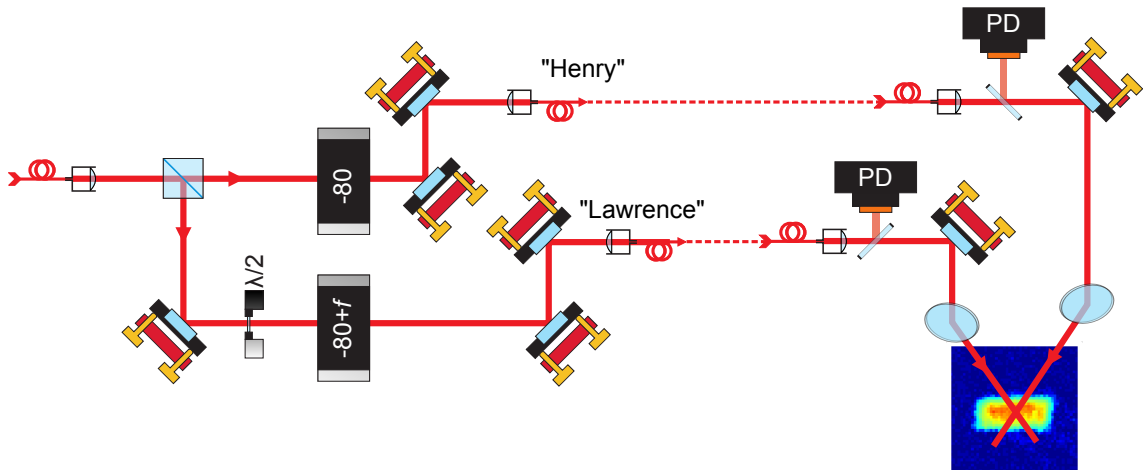
Figure 6.6: Optical arrangement for Bragg spectroscopy.

our box trap, and thus providing an optical field of uniform intensity across the condensate, both *in situ* and in time-of-flight.

Further, we stabilize the optical power in each of the beams using feedback signals from independent photodiodes (see Fig. 6.6). This allows us to keep the Rabi frequency Ω constant. We calibrate Ω by observing Rabi oscillations at resonance ($f \approx f_0$). Since Ω is directly proportional to the optical power in the beams [equation (6.5)], we can use the photodiode signal to measure Ω. For example, we adjust Ω when we change the duration of the Bragg pulse τ to keep the scattered fraction approximately constant in different experiments, as explained above.

We generally distinguish two different measurement regimes of Bragg spectroscopy: *in situ* and in time-of-flight.

In the former case, the momentum distribution does not change with time, allowing us to probe it using long pulses with $\tau \gtrsim L/v_{\mathrm{r}}$. This ensures that the Bragg spectrum is not significantly Fourier-broadened. Equivalently, it ensures that a recoiling atom can traverse the box during the pulse, and we thus probe phase coherence across the whole BEC. To apply very long Bragg pulses on a trapped cloud, we set the trap depth below the recoil energy hf_{r} [see Fig. 6.7(a)], so the diffracted atoms can continuously leave the box without bouncing off the trap walls.

In the case of ToF measurements, on the other hand, the wavefunction evolves in time, and τ places an upper limit on our temporal resolution. We thus use shorter pulses and increase Ω accordingly. We address *in situ* measurements first, before discussing measurements in ToF.
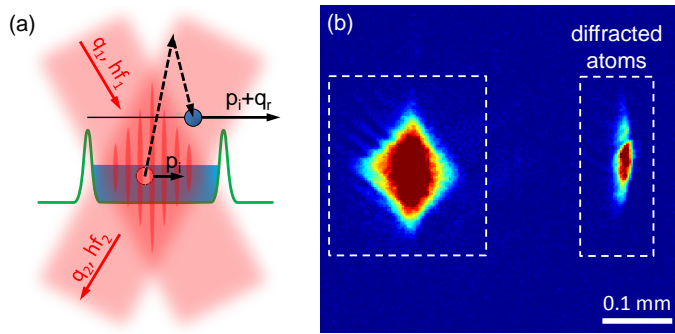
Figure 6.7: Bragg spectroscopy of a uniform BEC. (a) A trapped atom with initial momentum p_i undergoes Bragg scattering (see text). The trap wall height (green) is lower than the energy of the recoiling atoms. (b) Absorption image of the main cloud and the diffracted atoms, after $\approx 150\,\mathrm{ms}$ of separation. After the Bragg pulse, the non-diffracted atoms are released from the trap.

6.3 Ground-state wavefunction in momentum space

6.3.1 Spectrum width

In Fig. 6.8 we present our measurements of the momentum uncertainty of the condensed atoms in a box potential. Here $\tau = 35$ ms and the Bragg Rabi frequency was $\Omega/(2\pi) \approx 8$ Hz, keeping the fraction of diffracted atoms to $\lesssim 15\,\%$. We turn off the trap 25 ms after the end of the Bragg pulse, and measure the fraction of diffracted atoms after a further 110 ms of ToF [see Fig. 6.7(b)].

In Fig. 6.8 (a), we show measurements for $L = 30 \pm 1\,\mu$m. As shown in the left inset, L is determined by fitting the in-trap BEC density profile with a top-hat function convolved with a Gaussian that accounts for our 5-μm imaging resolution (as described in 4.3). In the main panel we show the measured Bragg spectrum, centered[2] on $f_\mathrm{c} \approx 1$ kHz. The solid red line shows the sinc^2 function $S(L)$. The dashed blue line shows the predicted spectrum $\tilde{S}(L)$, taking into account the small corrections due to the non-infinite τ and non-zero Ω, as described above. The data is clearly extremely close to the Heisenberg limit, corresponding to a fully coherent BEC wavefunction spanning the whole box.

We quantitatively compare different (measured and calculated) Bragg spectra using their full-width-at-half-maximum W. In the right inset of Fig. 6.8 (a), we plot the measured W versus the total atom number N, for $L = 30\,\mu$m. The solid red and

---

[2]Here, we take f_c to be the experimentally determined center of the distribution. It is close to f_r, and we address small deviations from f_r below.
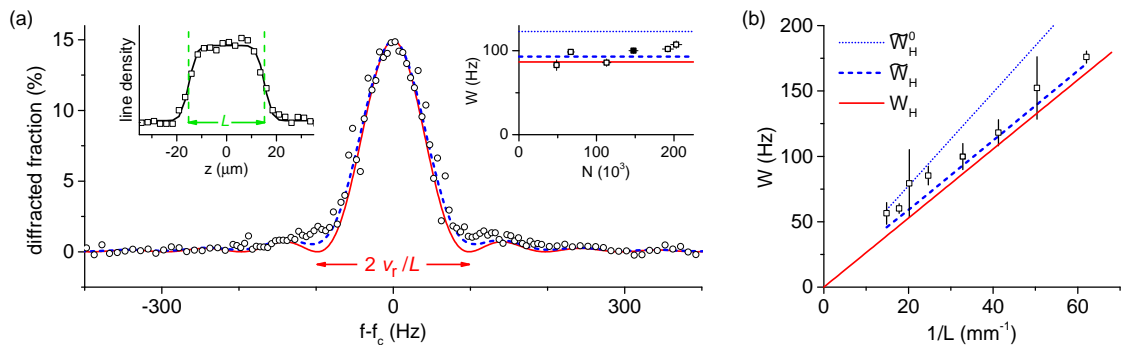
Figure 6.8: Heisenberg-limited momentum spread in a uniform interacting BEC. (a) Main panel: Bragg spectrum of a trapped BEC of length $L = 30\,\mu$m. The solid red and dashed blue lines show the theoretical Heisenberg-limited spectra $S(L)$ and $\tilde{S}(L)$, respectively (see text). Left inset: L is determined by fitting the in-trap BEC density profile, accounting for the imaging resolution. Right inset: Spectral width W versus the atom number N, for the same L. The filled square corresponds to the data in the main panel, with $W = (100 \pm 3)$ Hz. The solid red and dashed blue lines show $W_{\mathrm{H}} = 0.89\,v_{\mathrm{r}}/L = 87$ Hz and $\tilde{W}_{\mathrm{H}} = 93$ Hz, corresponding to $S(L)$ and $\tilde{S}(L)$, respectively. The dotted blue line shows $\tilde{W}_{\mathrm{H}}^0 = 123$ Hz, expected for a non-interacting BEC. (b) W versus inverse box length, $1/L$, showing the expected Heisenberg scaling. Solid red, dashed blue and dotted blue lines show W_{H}, $\tilde{W}_{\mathrm{H}}$ and $\tilde{W}_{\mathrm{H}}^0$, respectively.

dashed blue lines show the two calculated Heisenberg-limited values, W_{H} for $S(L)$ and $\tilde{W}_{\mathrm{H}}$ for $\tilde{S}(L)$. For comparison, we also calculate $\tilde{W}_{\mathrm{H}}^0$ (dotted blue line) for the sine-like non-interacting ground state of the box potential. We see that interactions reduce W below $\tilde{W}_{\mathrm{H}}^0$. Moreover, the measured W shows essentially no dependence on N, as expected for a BEC of a spatially uniform density.

In Fig. 6.8 (b) we summarise data for a range of box lengths, $L = 15 - 70\,\mu$m. Plotting W versus $1/L$, we observe the expected Heisenberg scaling of the momentum uncertainty.

6.3.2 Mean-field shifts

We now turn to the study of the ground-state energy of a uniform interacting BEC, which is seen in the shift of the Bragg resonance, f_{c}, from the recoil frequency f_{r}. Thanks to the extreme narrowness of our Bragg spectra, we can measure such shifts with a precision of ≈ 2 Hz, corresponding to an energy of $k_{\mathrm{B}} \times 100$ pK.

In Fig. 6.9 we plot f_{c} versus N, for a fixed $L \approx 30\,\mu$m and for two sets of Bragg spectra, taken "in-trap" (solid symbols) and "in-ToF" (open symbols). The in-trap
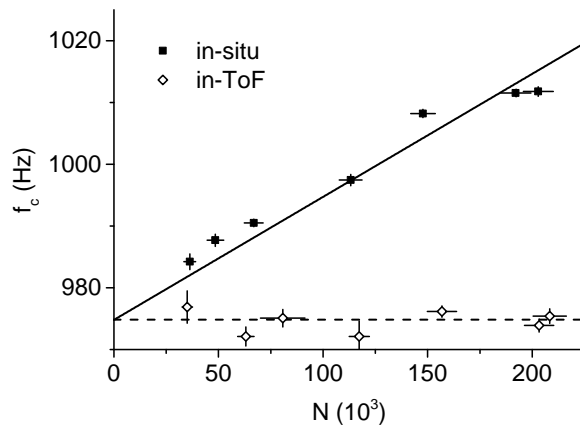
Figure 6.9: Interaction energy in a uniform BEC, for $L = 30\,\mu$m. We plot f_0 versus N for Bragg pulses applied in-situ (solid squares) and after 50 ms of ToF (open diamonds). Dashed line: $f_0 \approx f_r \approx 975$ Hz, solid line: $f_0 = f_r + \alpha N$, with $\alpha \approx 20 \times 10^{-5}$ Hz/atom.

spectra are taken as above, with the main cloud trapped during the Bragg pulse. For the in-ToF spectra we release the BEC from the box and let it expand for 50 ms before applying the Bragg pulse. After long ToF the atomic density is negligible and the N-independent f_c provides a good measurement of $f_r \approx 975$ Hz. According to 6.30, we can write

$$\Delta f_c \equiv f_c - f_r = \alpha N, \qquad (6.32)$$

with $\alpha = 2\eta\hbar a/(mV)$, where η is the condensed fraction[3] and V is the volume of the box. From in-situ images we get $V = (25 \pm 2) \times 10^3\,\mu$m^3. We assess $\eta = 0.8 \pm 0.1$ by numerically simulating the fraction of Bragg-diffracted atoms for $f = f_c$ [see Fig. 6.8 (a)]; here the uncertainty indicates variations between experimental runs. This estimate is further supported by "BEC filtering" introduced in Ref. [121], i.e., using a short (4 ms) Bragg π-pulse to separate the BEC from the residual thermal component in ToF[4]. We thus predict $\alpha_{\mathrm{th}} = (24 \pm 2) \times 10^{-5}$ Hz/atom.

From a linear fit to the in-trap data (solid line in Fig. 6.9) we get $\alpha_{\mathrm{exp}} = (20 \pm 1) \times 10^{-5}$ Hz/atom, slightly below α_{th}. This small difference is indeed expected for our $\Omega_R\tau$, due to the $\approx 15\%$ depletion of the ground-state population during the pulse. For $N \approx 200 \times 10^3$ we took additional measurements with a reduced Ω_R [122] and

---

[3]Both before and after undergoing Bragg scattering an atom initially in the BEC feels the same "double" interaction with any thermal component of the cloud. Bragg spectroscopy is thus sensitive only to the ground-state interactions.

[4]Note that the small thermal fraction is not directly measurable from either standard ToF images or the Bragg spectra such as shown in Fig. 6.8(a).

extrapolating to $\Omega_R = 0$ we get a slightly revised[5] $\tilde{\alpha}_{\mathrm{exp}} = (23 \pm 1) \times 10^{-5}$ Hz/atom.
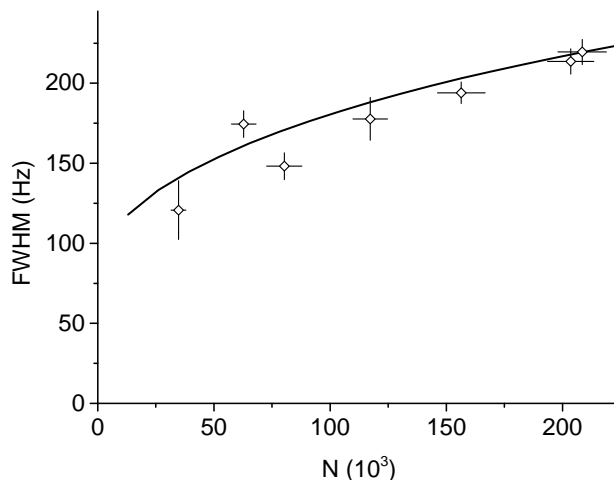

Figure 6.10: Measured FWHM of the momentum distribution after $50\,\mathrm{ms}$ TOF for different N (open diamonds). Simulated width shown (solid line).

Complementary to Fig. 6.9, in Fig. 6.10 we plot W values for the same in-ToF Bragg spectra. Qualitatively, W now grows with N because during ToF interaction energy gets converted into kinetic energy. Quantitatively, the problem of the expansion of an interacting BEC from a box potential has not been solved analytically (see [123] for the harmonic-trap case). However, we find good agreement between our data and numerical simulations based on the GP equation (solid line). In our simulations, we neglect the small thermal component and use the measured in-trap BEC energy ($\propto \tilde{\alpha}_{\mathrm{exp}} N$) to predict W in ToF[6].

6.4 Expansion of a quasi-pure BEC from a uniform trap

Finally, we study the evolution of the BEC in ToF, for $L \approx 30\,\mu\mathrm{m}$ and $N \approx 200 \times 10^3$. In Fig. 6.11 (a) we show absorption images of the expanding cloud (top), and the corresponding GP-based simulations (bottom). The simulations reproduce the characteristic diamond shape that emerges during ToF, also seen in Fig. 6.7 (b). In Fig. 6.11 (b) we show the gradual decay of Δf_0 and growth of W for in-ToF Bragg

---

[5]The systematic uncertainty in $\tilde{\alpha}_{\mathrm{exp}}$, due to the systematic uncertainty in our absolute atom-number calibration, is 10%.

[6]We also take into account the small curvature of our gravity-compensating magnetic field (see 5.3.2). This has a noticeable effect only for very long ToF ($\gtrsim 100$ ms).

spectra, again finding good agreement with our simulations (solid lines). Note that in these experiments, and simulations, we reduced τ to 10 ms and increased $\Omega_R/(2\pi)$ to 28 Hz, reducing our spectral resolution in order to improve the time resolution.
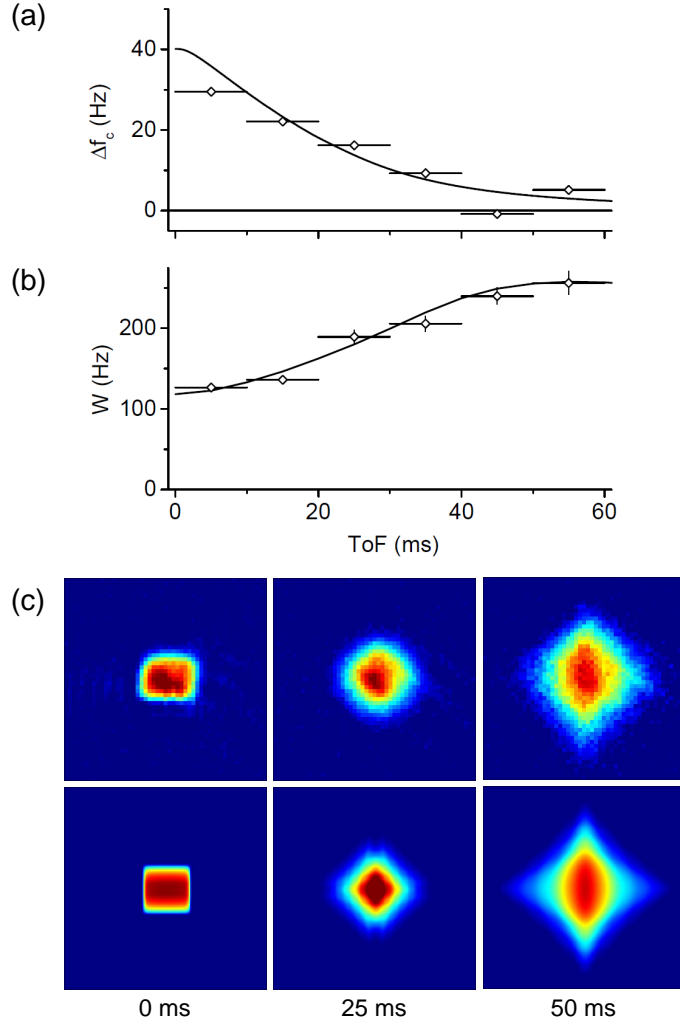

Figure 6.11: Evolution of the momentum distribution and mean-field energy of a BEC released from a uniform trap ($N = 125000$). (a),(b) FWHM and f_0 vs TOF: measured (open diamonds) and simulated (solid line,see text). The solid square indicates the value obtained from data in Fig. 6.9 by interpolation. (c) Measured (top row) and simulated (bottom row) optical density images of the expanding cloud at 0, 25 and 50ms.

In conclusion, we have characterised the ground-state properties of an interacting homogeneous Bose gas, including the Heisenberg-limited momentum distribution, the interaction energy, and the free-expansion dynamics. An important by-result of our measurements is that they place the most stringent bound so far on the spatial uniformity of an ultracold gas produced in our optical box. While earlier (thermodynamic) studies established uniformity on a $10 - 100$ nK energy scale [20, 21], all our present measurements indicate that our gas behaves as a homogeneous system down to a sub-nK energy scale (corresponding to 20 Hz in frequency units). Such a high degree of uniformity offers great promise for future studies of correlation physics in a homogeneous gas in the $T \to 0$ limit, for example for the preparation and detection of topologically protected states [124].

Chapter 7

Conclusions and Outlook

The system we chose to study in the experiments presented here - a uniform gas of identical bosons - is a textbook example of a quantum many-body system. Its appeal lies first and foremost in its fundamental importance and its apparent simplicity. Nonetheless, as this Thesis hopefully demonstrates, the system's behaviour is rich and complex. Both the theoretical description and the experimental studies present unique challenges. Importantly, however, it is the experimental implementation that was lagging decades behind the theorists' efforts. In the present work we tried to provide the missing experimental tools, and thus went to some length in documenting the details of technical nature.

The reader is probably aware that few of the experimental results presented here were unexpected. In fact, we have stressed excellent agreement with theoretical predictions throughout. Yet, none of these results could have been directly confirmed prior to the implementation of the tools we describe. Thus, one important aspect of this work is that it confirms existing mean-field theories in a textbook experimental system. Yet another way to look at it is that all our experiments confirm the quality of our system, in other words, we have shown that our system is indeed close to the textbook system we set out to emulate, beyond current experimental accuracy. Specifically, our implementation of a box trap is suitable for a variety of high-precision measurements.

Several applications can be envisioned. Some are in the planning or construction stage, while others are already producing promising results at the time of writing. As typical for evolutionary progress, many of these rely on combining several techniques previously explored in independent settings. Examples include:

- Uniform BECs with tunable interactions: A system producing BECs of ^{39}K for

loading into a uniform box trap is currently being built. Interaction strength can be tuned over a wide range using a Feshbach resonance [28], thus allowing further studies of interaction effects (including the potentially present beyond-mean-field contributions).

- BECs in two dimensions: By reducing the length of our box trap, the gas can be forced to effectively enter a 2D regime, where the reduced dimensionality leads to qualitatively different behaviour.

- Domain dynamics near the phase transition: By quenching the ultra-cold gas, we can observe the evolution of incoherent domains before coherence is established throughout the volume. Bragg spectroscopy allows us to measure the spatial correlation function, either by Fourier-transforming the momentum distribution, or directly, by using interferometric methods. We envision fundamental links to the Kibble-Zurek mechanism.

- Interferometric measurements using flexible geometries: Our light-shaping methods allow the creation of multiple boxes simultaneously. Degenerate samples can be split and overlapped, and various implementations are imaginable.

- Transport phenomena: We can also create a pair of weakly coupled reservoirs, with a narrow channel (either 2D or 1D) linking the two. Thermal and super-fluid flow across the channel can be studied, in analogy with superfluid helium experiments.

Overall, the work presented here will hopefully prove to be a useful step towards further developments in the field of ultra-cold atoms. The enthusiasm and dedication exhibited by every member of our group as they commit to these new challenges leaves me certain that new results will be plentiful in the very near future.

Appendices

Appendix A

Performance of Grating-Stabilized Diode Lasers

A.1 Grating-Stabilized Tunable Diode Laser Basics

One of the experimental appeals of ^{87}Rb is the availability of relatively cheap and maintenance-free laser diodes at $780\,\text{nm}$. Laser diodes utilize various semiconductor geometries to provide a gain medium and a lasing cavity. Pumping is achieved by passing a current through the semiconductor structure. For a review of basic operating principles and available types of laser diodes we refer to [125]. The internal cavity of a laser diode provides frequency selectivity due to its typical Fabry-Pérot gain profile. However, the free spectral range of typically $\sim 50\,\text{GHz}$ is much smaller than the frequency range over which the lasing medium provides a significant gain. The laser diode will thus typically emit a multi-mode signal at a range of frequencies. To provide frequency selectivity, an external cavity with a frequency-selective output coupler can be used. A diffractive grating adjusted such that it reflects a particular non-zero order back into the laser diode allows us to select one of the internal cavity modes, and the narrow width of the external cavity modes can further reduce the line width of the output. The mode selection process is illustrated in Fig. A.1.

Multiple variants of the grating feedback mechanism have been successfully implemented [125]. The two most widely used schemes are the Littman/Metclaf [42] and the Littrow [45]. Most atomic physics experiments use variations of the latter, mainly due to its simplicity and higher output power. A wide-spread design proposed in [45] (Hänsch) is shown in Fig. A.2 (a). Several mechanisms allow tuning
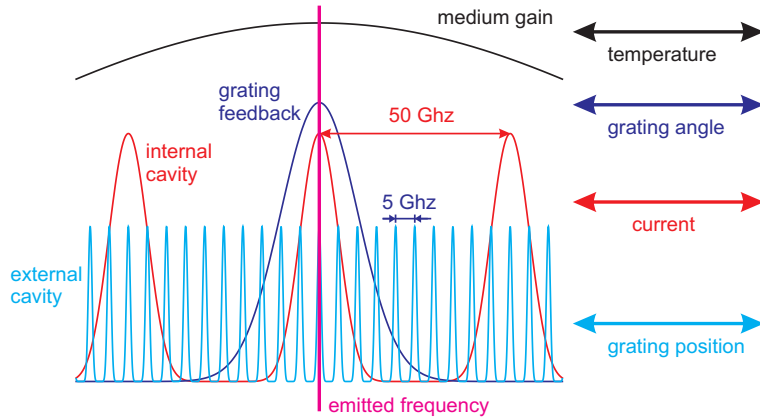
Figure A.1: Mode selectivity in a grating stabilized diode laser: main contributions and tuning mechanisms

of the diode laser frequency. The internal cavity modes are tunable by adjusting the temperature and/or the current. The external cavity is tunable by displacing the grating, and the preferred grating feedback wavelength depends on the grating angle. For continuous frequency tuning, we must ensure that the same mode receives maximum gain throughout, thus avoiding mode hops. It is important to control grating angle, external cavity length and the diode current simultaneously. The first two are usually controlled using a single piezoelectric actuator. Modulating the diode current with a signal proportional to the piezo control voltage ("current feed-forward") improves the mode hop free scanning range and facilitates locking (see below).
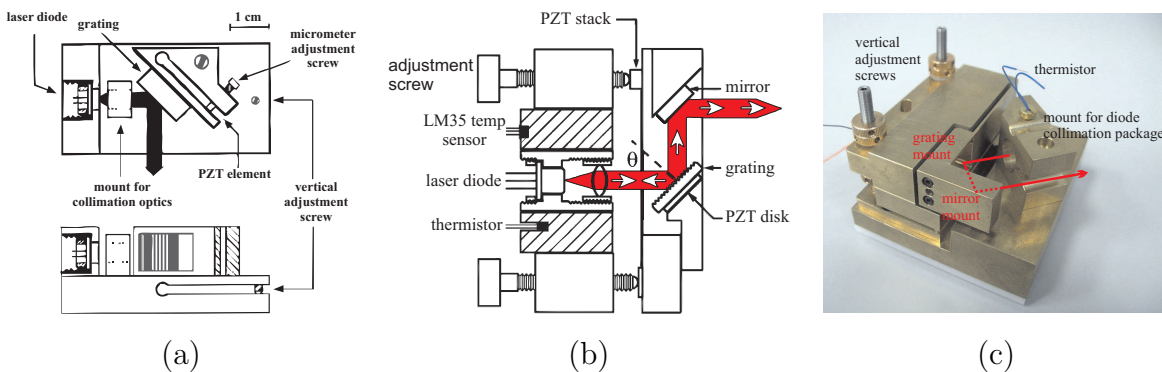

(a)   (b)   (c)

Figure A.2: ECDLs in Littrow configuration: Hänsch design [45] (a), Sussex-Melbourne design [47] (b) and Alex Gaunt design (c)

A.2   Laser Design and Performance

The Hänsch design has two drawbacks: firstly, the output beam direction changes if tuning over a wide range, and secondly, the grating feedback and external cavity modes do not move at the same rate in frequency space (Fig. A.1), causing mode hops. The first problem can be eliminated by introducing a mirror moving with the grating [47], as shown in Fig. A.2 (b). Same design addresses the second issue by introducing an additional piezoelectric actuator ("disk") for cavity length control. Another way is to choose a pivot point which maximizes the mode hop free tuning range [44]. Alex Gaunt built a diode laser combining the benefits of an optimized pivot point and fixed beam output direction by mounting a mirror in the moving cantilever arm, as seen in Fig. A.2 (c). However, since the mode hop free range required to resolve the hyperfine structure of Rb is very small ($\sim 7\,\mathrm{GHz}$), these design features turned out to be far less important than the overall mechanical stability, power and locking bandwidth.

Diode lasers can typically provide $\sim 20 - 100\,\mathrm{mW}$ of power. Since this is clearly not sufficient for cooling, it was decided to purchase a Toptica DLpro diode laser with a BoosTA tapered amplifier, providing up to $100\,\mathrm{mW}$ before and $1.5\,\mathrm{W}$ after the amplifier. The laser is supplied with an FPGA controlled digital locking system and is highly stable and virtually maintenance free.

Following some previous in-house laser development by Phil Richman [126] and Alex Gaunt, it was decided to use one of their designs for the repump laser. We first address laser operation issues common to both lasers, and then discuss the drawbacks of each design.

A.2.1   Laser Diodes and Alignment

Crucial to laser performance is the choice of diodes. Most important in our experience was to choose a diode with a free-running wavelength closest to $780\,\mathrm{nm}$. It is advantageous to tune the free-running wavelength of the diode (without grating feedback) by changing the temperature prior to further alignment. A tunability of $+0.3\,\mathrm{nm/K}$ can be expected. Most laser diodes have a higher wavelength which necessitates cooling, we are however restricted by the dew point, only allowing a $6\,\mathrm{K}$ reduction in temperature. This corresponds to typically $2\,\mathrm{nm}$ wavelength change, which is insufficient for some diodes. We made good progress with ADL-78901TL diodes from Laser Components, achieving output powers of $60\,\mathrm{mW}$ at the desired wavelength. Other high power diodes we tested included L785P090 and L785P100

from Thorlabs. They lased at $785 \pm 1\,\text{nm}$ and where unsuitable form our applications. Both lasers utilize a diode collimation package from Thorlabs. The first step is to collimate the output beam by adjusting the lens. Output of most commercial laser diodes is elliptic and plane polarized, with the polarization axis parallel to the semi-minor axis of the ellipse. For improved resolution, we want to illuminate as many grating lines as possible. This requires the laser diode to be rotated such that the polarization plane is parallel to the grating lines. Both designs use the -1st order reflection, with both the incidence and reflection angle close to 45°. A wavelength of $\approx 780\,\text{nm}$ is achieved in this configuration if a $1800\,\text{mm}^{-1}$ grating is used. A small diffraction efficiency (< 0.3) is required to avoid diode damage at high powers. The grating must be aligned such that it is perpendicular to the beam plane. Both laser designs have a vertical adjustment screw. Coarse alignment is achieved by observing the reflection off the diode facet and overlapping it with the main beam. Further feedback optimization is best performed by measuring the threshold current and minimizing it using both vertical and horizontal adjustment screws. The grating position can then be scanned with an effective scanning range of $\sim 10\,\text{GHz}$ while tweaking current and temperature to achieve best mode hop free performance near the desired absorption spectroscopy peaks (spectroscopy and locking are discussed in B). Multi-mode lasing is often an issue. It leads to dramatic deterioration in the error signal and can be easily spotted by observing the Fabry-Pérot spectrum using a wavemeter. It is best corrected by making small adjustments to the current. The performance of both lasers improves dramatically when using a mechanically shielded enclosure, as shown in Fig. A.3. Heavy aluminium blocks
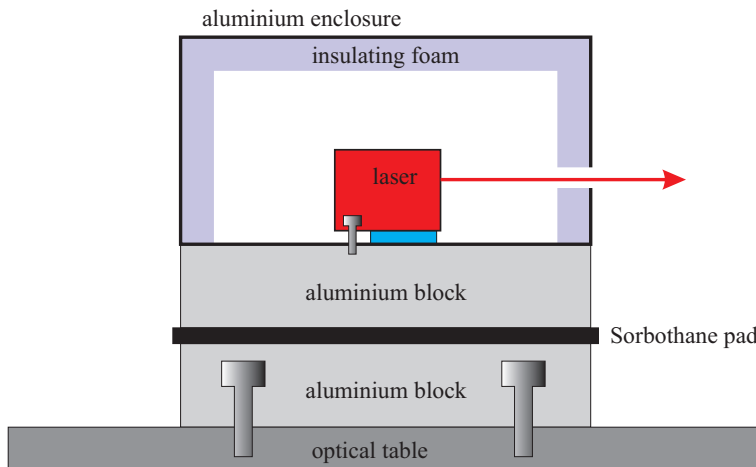

Figure A.3: Components for mechanical shielding and thermal stabilization of grating-stabilized diode lasers

provide mechanical and thermal stability. A viscoelastic Sorbothane pad is used for additional vibrational isolation. A layer of foam provides acoustic shielding and impedes convection currents.

A.2.2   Alex Gaunt design

The first laser we used in the optical setup was built by Alex Gaunt with high mode hop free scanning range in mind, necessitating a large distance between the pivot point and the grating. The additional mirror also increased the oscillating mass significantly. The long, thin cantilever deformed plastically on multiple occasions and was not able to provide the restoring moment to follow the piezo stack at high frequencies. In scanning mode, the effects can be reduced by avoiding discontinuous sawtooth modulation and using a low-frequency triangle or sine wave instead. The main drawback of the laser turned out to be its susceptibility to external noise. To investigate the problem further, we performed eigenmode analysis of the cantilever design using Autodesk Inventor Simulation. The two lowest eigenmodes are shown in Fig. A.4.
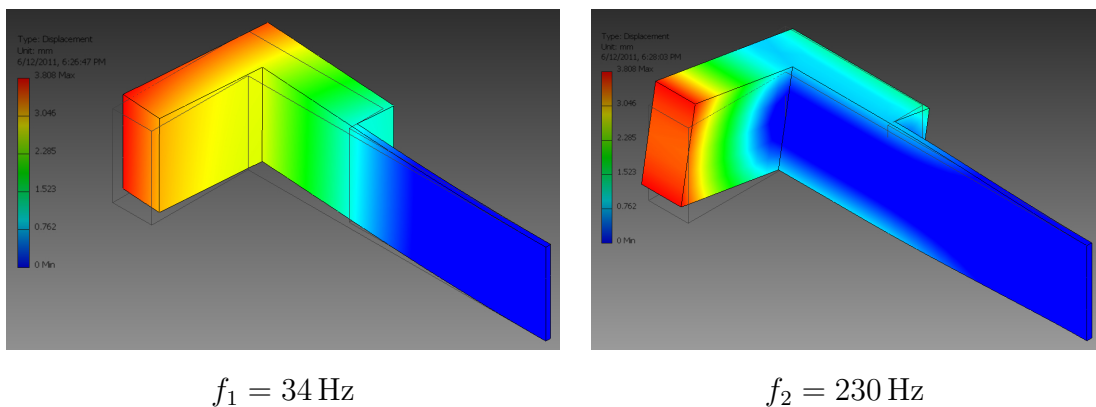

$$f_1 = 34\,\mathrm{Hz} \qquad\qquad\qquad f_2 = 230\,\mathrm{Hz}$$

Figure A.4: Two lowest eigenmodes of the cantilever

The first eigenmode at $f_1 \approx 34\,\mathrm{Hz}$ corresponds to the desired cantilever motion during laser tuning. Its frequency however is very low due to the increased mass and length compared to other common designs. For the grating to respond to the piezo with a high enough bandwidth, the cantilever has to be pre-bent strongly, approaching the limit of elastic deformation. The effect of reduced bandwidth is clearly visible in the spectroscopy signal as ringing when driving the piezo with a discontinuous signal like a sawtooth (see below).

The second lowest eigenfrequency of the cantilever is $f_2 \approx 230\,\mathrm{Hz}$ and corre-

sponds to a torsional mode. It appears due to the large mass of the mirror positioned out of the cantilever plane. Like the first eigenfrequency, it lies in the acoustic range and the cantilever will be susceptible to noise. Unlike the bending however, the torsional mode will lead to loss of feedback altogether, and thus severe mode hopping.

The eigenfrequencies of a standard Hänsch design are much higher, and especially the torsional modes only appear in the kHz region.

Using Alex Gaunt's design in a saturated absorption spectroscopy setup, we were able to resolve the hyperfine structure of the ^{87}Rb D2 line in a single scan, i.e. with a scanning range of at least $7\,$GHz. We where however unable to achieve stable locking.

A.2.3 Phil Richman design

The laser built by Phil Richman is based on the Sussex-Melbourne design shown above, however it lacks the second piezoelectric actuator (PZT disk). Its greatest advantage is the ease of manufacture from standard parts. The heavy, spring-loaded lever provided mechanical stability far superior to the laser by Alex Gaunt. Due to the large lever length, the pizo stack only allowed a scanning range of $\sim 10\,$GHz, which could easily be solved by replacing the stack. We only managed to achieve a mode hop free scanning range of a few GHz, this was however sufficient to lock the laser and use it in a MOT experiment. The laser often remained locked for hours, was however subject to mechanical creep following alignment. Currently, we are using this laser for MOT experiments with varying degrees of success. Due to the compromised stability if the laser we decided to replace it with another DLPro.

Appendix B

Saturated Absorption Spectroscopy and Locking

Atomic physics experiments require laser sources which are stable to within a fraction of the natural linewidth of the atomic transition. While the linewidth of an external cavity diode laser is usually sufficiently small, drifts in the central frequency exceed the ^{87}Rb linewidth of $6\,\text{MHz}$ by far. The frequency of the diode laser must thus be actively stabilized using a feedback loop.

B.1 Principles of Absorption Spectroscopy

Absorption of a single probe beam passing through an atomic vapour will peak when it is on resonance with an atomic transition. Absorption can be easily measured by scanning the frequency of a tunable laser over the range of interest and recording the transmitted beam intensity with a photodiode. Due to the Doppler effect, a simple two-level atom moving at velocity v along the beam will only be on resonance if the laser frequency ω satisfies $\omega = \omega_0 + kv$, where ω_0 is the actual transition frequency and k the wavenumber of the laser. Since the velocities in a gas follow a thermal distribution, every absorption peak will be Doppler-broadened by as much as $1\,\text{GHz}$ in ^{87}Rb at room temperature. While transitions in the D2 line with different ground states can still be resolved, the hyperfine splitting of the excited state is not detectable. A common method is to introduce a strong counterpropagating pump beam derived from the same laser source. A moving atom sees the pump and the probe beam at frequencies $\omega \pm kv$ respectively. If we make the pump beam strong enough (such that it exceeds the saturation intensity), it will deplete the ground state population of resonant atoms, i.e. those satisfying $\omega = \omega_0 - kv$. This will not

affect the probe beam unless the latter is resonant with the same group of atoms, which will only happen if $v = 0$ and $\omega = \omega_0$. Is this the case, the absorption of the probe beam will be greatly reduced and we will see a "Lamb dip" in the absorption signal. The position and width of the Lamb dips is no longer affected by the (first-order) Doppler effect.

The observed saturated absorption spectrum is more complicated for a multi-level atom. If two atomic transitions at ω_1 and ω_2 share a common ground state, we will see a drop in absorption for any of the four cases

$$\omega - kv = \omega_1, \quad \omega + kv = \omega_1 \tag{B.1}$$

$$\omega - kv = \omega_2, \quad \omega + kv = \omega_2 \tag{B.2}$$

$$\omega - kv = \omega_1, \quad \omega + kv = \omega_2 \tag{B.3}$$

$$\omega - kv = \omega_2, \quad \omega + kv = \omega_1 \tag{B.4}$$

Solving these, we see that a Lamb dip will appear at frequencies ω_1, ω_2 as well as $(\omega_1 + \omega_2)/2$. The last one leads to the appearance of what is known as a cross-over peak.

Finally, if the two transitions share a common excited state, the pump beam resonant with the transition at ω_1 will deplete the corresponding ground state and *increase* the occupancy of the second ground state through spontaneous decays. If the pump beam is resonant with the second transition at ω_2 at the same time, absorption will *increase*, showing as an inverted cross-over peak in the frequency scan.

A typical spectroscopy setup is shown in Fig. B.1. The pump beam is retroreflected and used as the probe beam. A $\lambda/4$ wave plate before the mirror is used to make the light circularly polarized. Its handedness changes upon reflection, and after passing through the wave plate a second time the probe light's polarization is at 90° to that of the pump beam, enabling us to divert it to a photodiode.

A typical absorption spectroscopy signal obtained with this setup is shown in Fig. B.2 (a). The $F = 1$ and $F = 2$ Doppler peaks in ^{87}Rb are clearly visible, as well as the peaks originating from ^{85}Rb contained in the same vapour cell. The hyperfine structure within each Doppler peak is visible through saturation peaks, as shown for the repump transition in Fig. B.2 (b). All six peaks corresponding to the $F = 1$ ground state can be clearly identified, including the three stronger crossover peaks. The $F = 1 \to F' = 0$ peak appears inverted, suggesting multiple closely spaced ground states. This can be explained if one remembers that any external
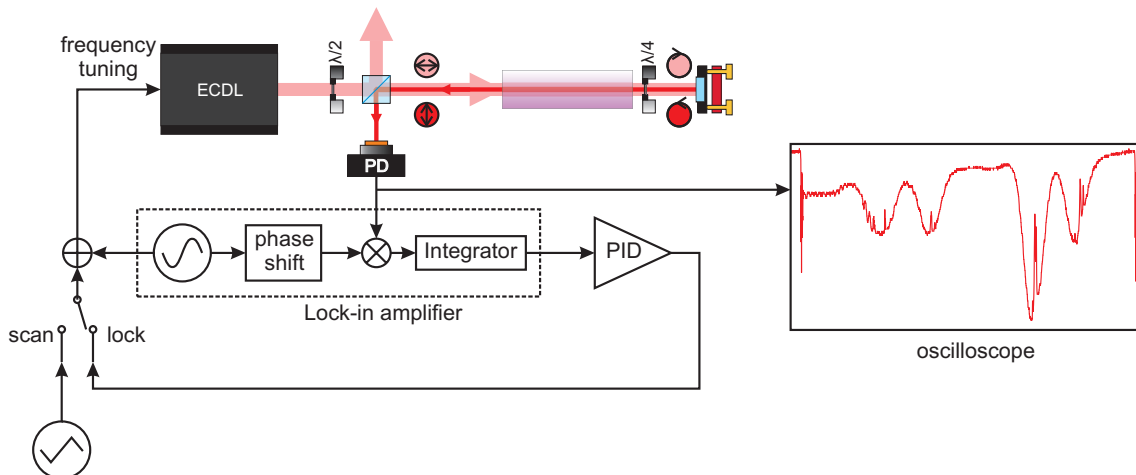
Figure B.1: A simple setup for saturated absorption spectroscopy and AC locking

magnetic field will split the $F = 1$ state into three Zeeman sub-states. There are therefore three distinct transitions: $\sigma^+ (|F = 1, m_F = -1\rangle \rightarrow |F' = 0, m_{F'} = 0\rangle)$, $\pi(|F = 1, m_F = 0\rangle \rightarrow |F' = 0, m_{F'} = 0\rangle)$ and $\sigma^- (|F = 1, m_F = +1\rangle \rightarrow |F' = 0, m_{F'} = 0\rangle)$. Each pair of these can produce an inverted cross-over peak. The six peaks are not resolved for the small fields in question - typical Zeeman splitting in the Earth field is $0.5\,\text{MHz}$. Note that for most magnetic field directions both the σ^+ and the σ^- transitions couple to either vertically or horizontally polarized light, in particular for a B field along the laser beam. This is also the field direction for which the π transition is not permitted with either polarization. The strength of each of the corresponding peaks is therefore strongly dependant on the magnetic field direction, and thus add up to a peak of variable strength. This is easily confirmed experimentally by moving a bar magnet in proximity to the vapour cell. Experimentally, we always observed the peak to be inverted, meaning that the cross-over peaks dominate for all field directions.

B.2   Frequency Modulation Spectroscopy and Locking

To lock the laser frequency to one of the ^{87}Rb D2 transitions we must derive an error signal, that is a signal which is monotonous near the peak centre and zero when the laser is on resonance. Using the spectroscopy signal $s(\omega)$, it is only possible to lock to the side of one of the peaks (after introducing an offset to make it zero-crossing). What we really need is its derivative. This can be achieved using frequency
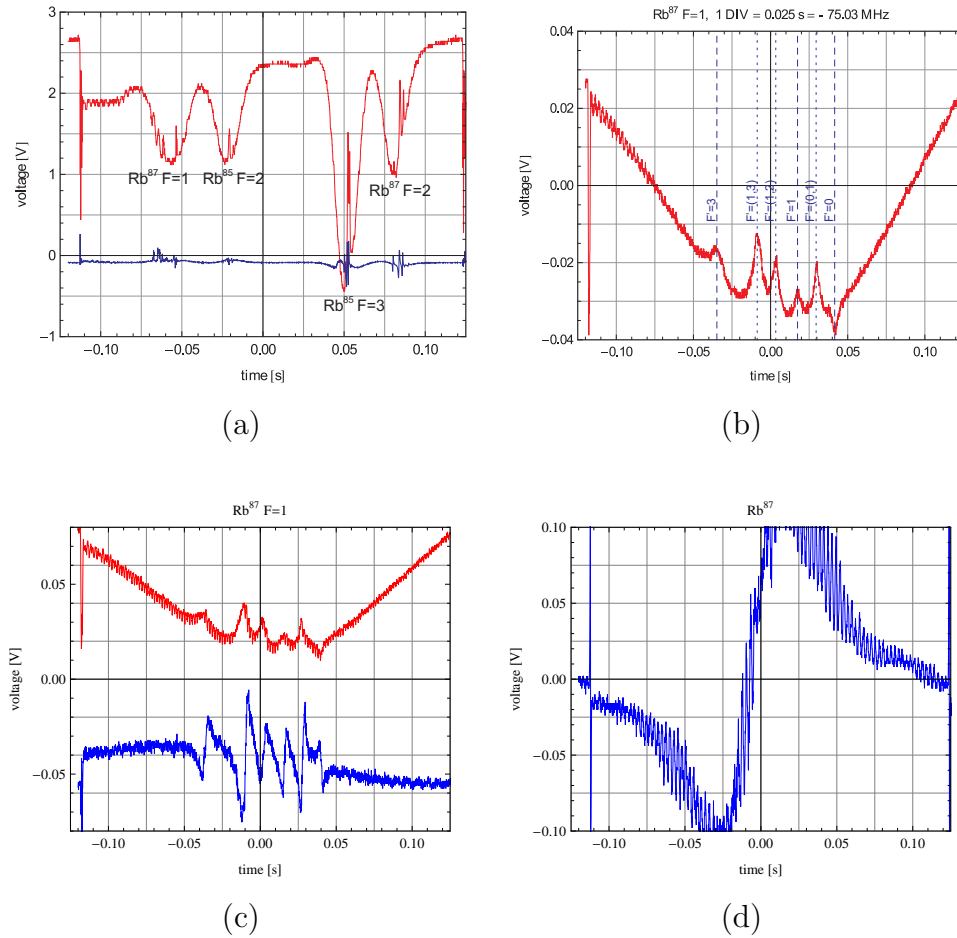
Figure B.2: Saturated absorption signals (red) and deriver error signals (blue). (a) Scan over $\sim 10\,\mathrm{GHz}$, showing the hyperfine structure of two Rb isotopes; (b) scan over the $^{87}\mathrm{Rb}F = 1$ feature, with theoretical peak positions fitted to the data; (c) same as (b) with modulation and the corresponding error signal; (d) magnified view of the error signal slope centred on the (0,1) cross-over peak. (Alex Gaunt's laser was used for spectroscopy)

modulation spectroscopy [49]. Consider sinusoidal modulation of the laser frequency around the centre frequency ω_0: $\omega(t) = \omega_0 + A\sin\omega_m t$. For small modulation amplitude A, we can write $s(t) \approx s(\omega_0) + As'(\omega_0)\sin\omega_m t$. Extracting the spectral component at ω_m therefore yields s', which can be used as the error signal. This is achieved using a lock-in amplifier shown schematically in Fig. B.1. Fig. B.2 (c) shows the spectroscopy signal from Fig. B.2 (b) with added modulation in red, and the derived error signal in blue. Optimizing the error signal quality is paramount for stable locking. The error signal slope shown in Fig. B.2 (d) is indicative of the maximum noise level for which stable locking is possible. The error signal is processed using a proportional-integral-derivative controller (PID) which provides

the feedback signal for adjusting the laser frequency.

Appendix C

IGBT driver electronics

Our experimental sequence requires switching quadrupole coil currents of up to 200 A on the ms timescale. Insulated-gate bipolar transistors (IGBTs) are among the few solid state devices capable of operating at such high currents (in our setup, we use IGBTs of the type SEMiX402GB066HDs). In the process of building our experiment, we have developed custom driver electronics with the intention of providing a reliable standard solution for the current as well as future BEC machines and incorporating various safety features.

Figure C.1: IGBT driver curcuit: IGBT interface.

The gate capacity of an IGBT is typically high, requiring high driving currents. A typical driving circuit is shown in Fig. C.1. At the input, it takes a TTL signal derived from the logics circuit shown in Fig. C.2. The latter implements safety features by combining inputs from external temperature sensors, coolant flow sensors and interlocks. The safety shut-off is latching, and a reset must be forced to resume operation. Further, the circuit provides facilities to set a maximum "on" time.

All components are assembled on a two-sided printed circuit board, as shown in Fig. C.3. The interface to the IGBT is via a ribbon cable, and the system was

designed with the ease of small-series assembly in mind. Figure C.4 shows two IGBT drivers, together with the front panel, the IGBTs, water cooling, and high current leads, assembled for use in a new BEC experiment currently under construction in our group.
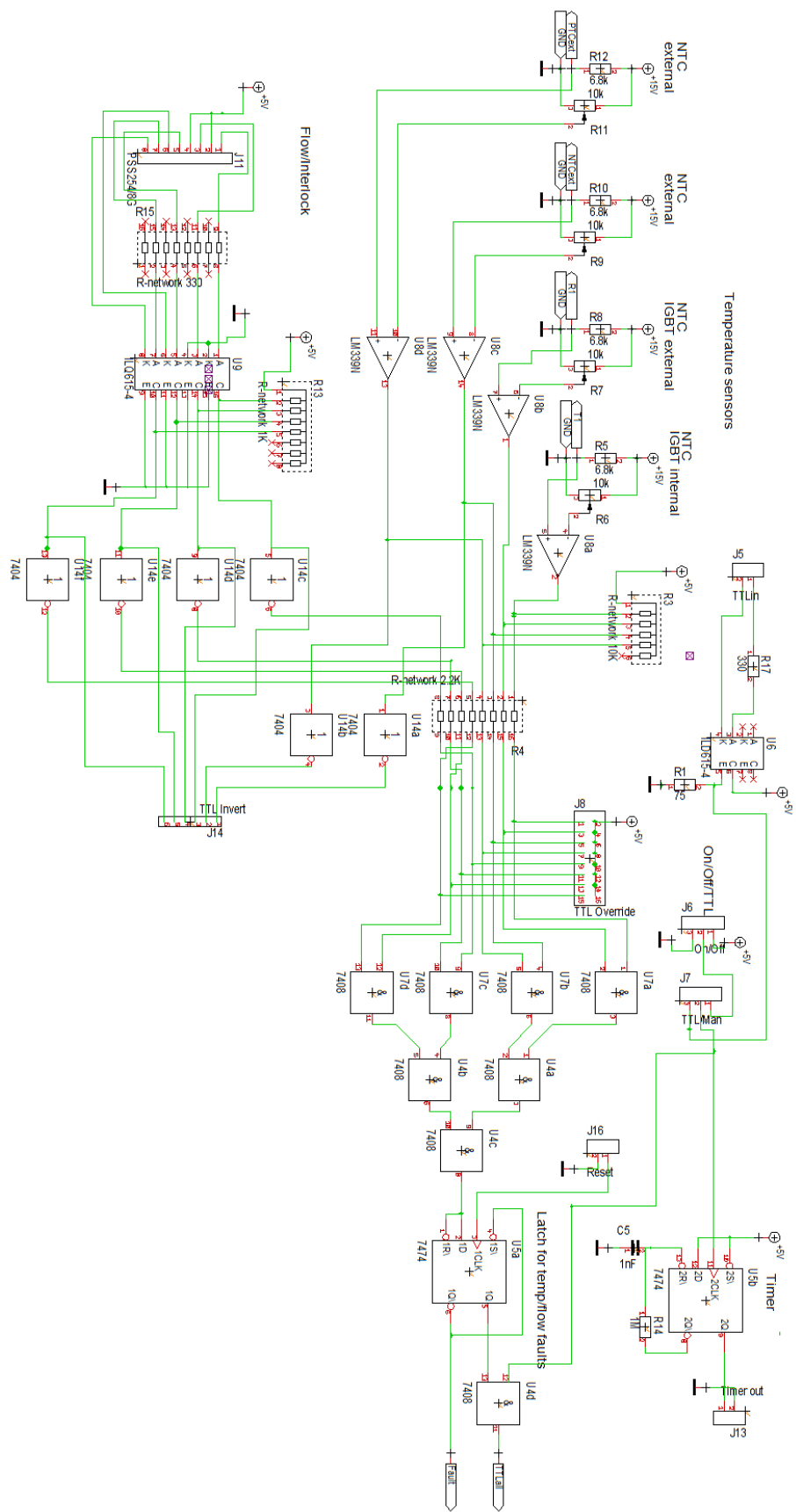
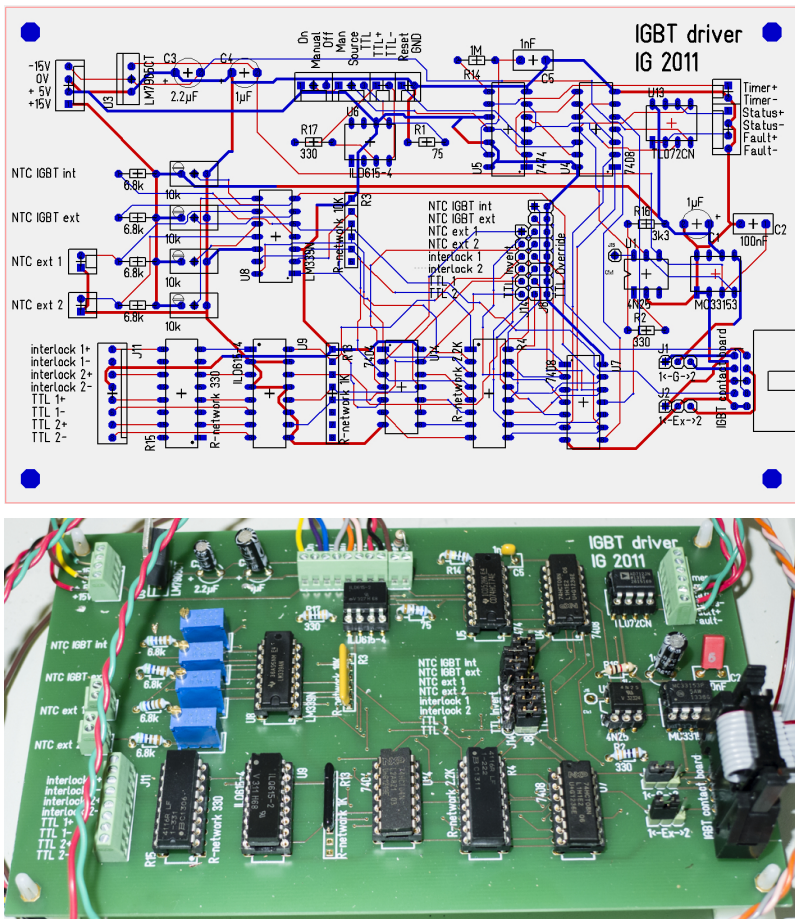**Figure C.2:** IGBT driver curcuit: TTL layout and external inputs.

Figure C.3: IGBT driver implementation, showing the printed circuit board layout (top, two copper layers shown in red and blue) and the assembled circuit(bottom).
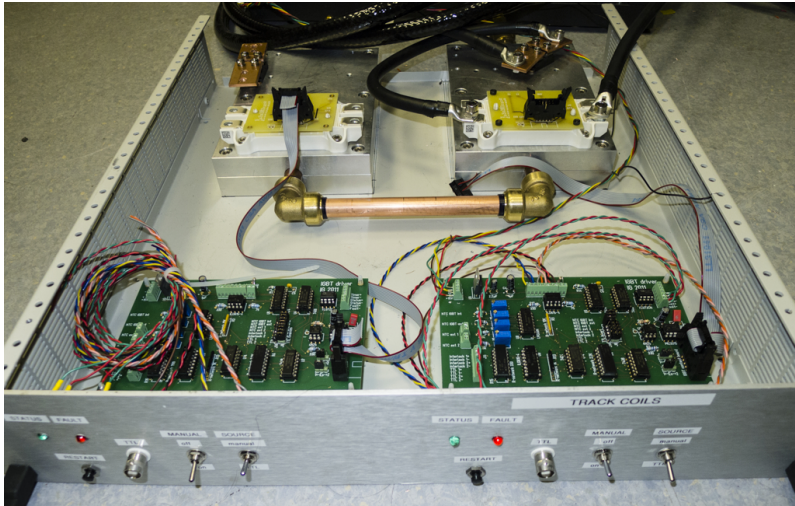

Figure C.4: Two IGBT drivers in use. Front panel, two water-cooled IGBTs, and ribbon cable leads carrying driving signals and temperature sensor signals are clearly visible.

Appendix D

Analysis Software

Ultra-cold atom experiments rely on analyzing thousands of optical density images. We have developed custom software ("Image Analysis GUI") for this purpose. The software is implemented in MATLAB, and a clear separation between the front-end (the graphical user interface, GUI) and the back-end (all processing and analysis routines) is maintained. This allows us to use the back-end code in external batch-processing routines to provide functionality not implemented in the GUI. Below, we present the main components of the software.

D.1 Graphical user interface

The GUI is shown in Fig. D.1, and includes the following key components:

- Toolbar (topmost): provides import, export, auto-load and image sorting buttons.

- Thumbnail panel (top): provides a quick view of the open images.

- Properties tab (left): displays file information, allows the input of physical parameters and the region of interest (ROI) to be used for image analysis.

- Inspect tab (left): shows properties of the ROI of individual pixels.

- Image tab (center): displays the selected image, its cuts and the fitting function.

- Summary tab (center): shows a table of all images with analysis results.

- Fitting tab (right): gives access to different analysis routines, allows fine-tuning of fitting parameters and batch fitting.
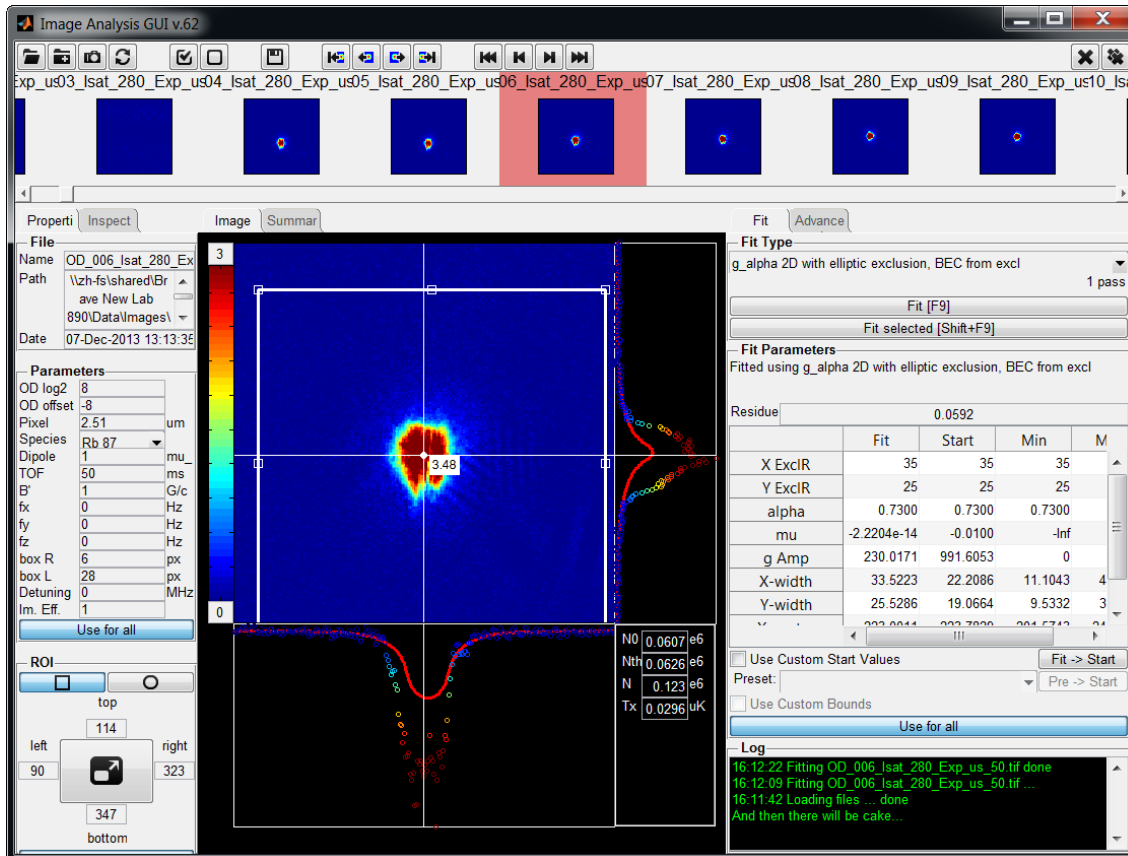
131

Figure D.1: Image analysis GUI window, showing the main components of the user interface (see text).

- Advanced tab (right): controls down-sampling and filtering of images.

D.2 Software architecture

We use object-oriented implementation. The following files and classes are provide the core functionality

- `AnalysisGUI62.m` (executable): defines the user interface; maintains an array of loaded images of the type `ODImage`.

- `ThumnailViewer.m` (class): defines the functionality of a scrollable panel of thumbnails.

- `ODImage.m` (class): stores file path, name, image data, fitting data and all other image information. `ODImage.FitPlugin` is used to store a fitting plugin object implementing the mathematical fitting routines.

- Fitting plugins, e.g. `Gauss2D.m`, `g_alpha_2D_ell_mu0_excl_count.m` etc. (each a handle class): implement the respective fitting routines. Their methods are called from the respective `ODImage` object.

An important consideration was efficient memory use. Thus, `ODImage.Compress()` and `ODImage.Expand()` routines are implemented to remove image data from RAM when not needed for plotting or analysis and load it from the hard drive when necessary.

Appendix E

The polylogarithm function

E.1 Definition

The polylog function is commonly defined as

$$g_\alpha(x) = \sum_{k=1}^{\infty} \frac{x^k}{k^\alpha} \tag{E.1}$$

For $\alpha > 1$ and $x = 1$, this becomes the Riemann zeta function:

$$g_\alpha(0) = \zeta(\alpha) \tag{E.2}$$

Trivially, $g_\alpha(x)$ converges as $x \to 1$ for $\alpha > 1$ and diverges otherwise.

E.2 Integrals

Within the local density approximation, we often need to evaluate integrals of the form

$$\int_{-\infty}^{\infty} g_\alpha\left(ze^{-a|x|^s}\right) \mathrm{d}x = 2\int_0^\infty \sum_{k=1}^{\infty} \frac{z^k e^{-kax^s}}{k^\alpha} \tag{E.3}$$

$$= \sum_{k=1}^{\infty} \frac{z^k}{k^\alpha} 2 \int_0^\infty e^{-kax^s} \tag{E.4}$$

$$= \sum_{k=1}^{\infty} \frac{z^k}{k^\alpha} 2 \frac{\Gamma(1+\frac{1}{s})}{(ak)^{1/n}} \tag{E.5}$$

$$= 2\Gamma\left(1+\frac{1}{s}\right) a^{-1/n} \sum_{k=1}^{\infty} \frac{z^k}{k^{\alpha+1/n}} \tag{E.6}$$

$$= 2\Gamma\left(1+\frac{1}{s}\right) a^{-1/n} g_{\alpha+1/n}(z) \tag{E.7}$$

In the commonly encountered case $n = 2$, the pre-factor is $2\Gamma\left(1+\frac{1}{2}\right) = \sqrt{\pi}$.

Appendix F

Efficient numerical evaluation of the polylogarithm functions

Polylogarithm functions $g_\alpha(x)$ are used extensively in our image analysis routines. Least-square fitting of a parametrised model to an optical-density can involve $\sim 10^8$ evaluations of g_α *per image*. Processing thousands of experimental runs in real-time requires an efficient algorithm. Unfortunately, few standard libraries provide the polylogarithm functions of arbitrary order. Wolfram Mathematica provides the arbitrary-precisions function PolyLog$[\alpha, x]$. In our applications, precisions well short of machine precision is acceptable, while evaluation time is often critical. As a starting point, we used the MATLAB implementation by M. Kuhnert [127], which is in turn based on the numerical approximations derived in [128]. The relative numerical error of this method is illustrated in Fig. F.1 for $g_0.5(x)$ and $g_1.5(x)$, $0 \leq x < 1$. It can be seen that the relative error never exceeds 10^{-5} - this is always significantly lower than experimental errors in the optical density measurements. While this method provides a huge improvement in speed compared to the built-in Mathematica function (see Table F.1), we found that it was not allowing real-time image processing (i.e., fitting a single image took longer than one repetition of the experimental sequence).

We achieved more than a 10-fold improvement in evaluation speed by optimizing the evaluation order, without changing the mathematical approximations used (Table F.1). The general principle is best illustrated by a simple example: assume we are trying to evaluate a polynomial approximation of the form

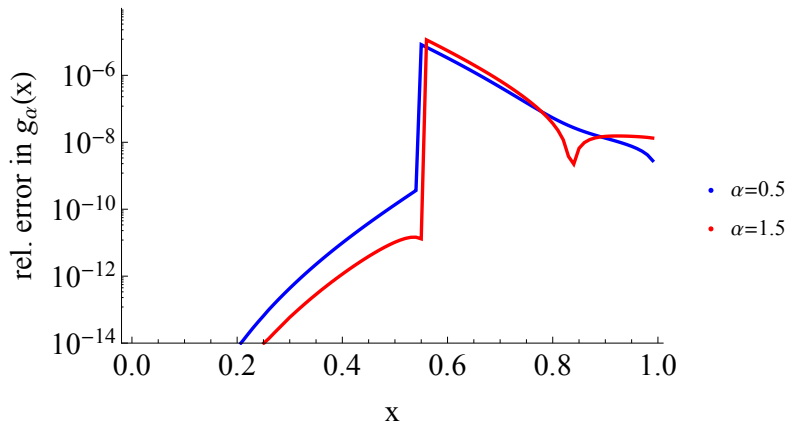$$p(x) = a_0 + a_1 x + \cdots + a_n x^n \tag{F.1}$$

Figure F.1: Relative error of our numerical approximation for $g_\alpha(x)$, plotted for $0 \leq x < 1$ for $\alpha = 0.5$ (blue) and $\alpha = 1.5$ (red)

method	PolyLog [129]	polylog [127]	polylog [130]
evaluation time	$40\,\mathrm{s}$	$0.2\,\mathrm{s}$	$0.018\,\mathrm{s}$
relative speed	$1/400$	1	11

Table F.1: Benchamarks for different implementations of the polylogarithm function. We evaluate $g_\alpha(x)$ for n uniformly spaced points on $[0, 1]$. Data shown was obtained for $n = 10^5$, $\alpha = 0.5$. Test rig: Sony Vaio laptop, Intel(R) Core(TM) i7-3632QM 2.20GHz CPU, 8GB RAM, 64-bit Windows 7, Mathematica 9.0 64-bit, MATLAB R2012n 64-bit.

Evaluating terms of the form x^n requires (in the worst case) n multiplications[1], for a total of $\sim n^2/2$ multiplications to evaluate all terms in the above expression. On the other hand, we can write

$$p(x) = a_0 + x(a_1 + x(a_2 + x(\cdots))) \tag{F.2}$$

for a total of only n multiplications. Further optimizations can be made, generally by minimizing repeated calls to recursive sub-routines. A comparison between the original and the improved code can be seen in the (shortened) listing below.

---

[1]Optimized algorithms allow an evaluation in $\sim \log_2(n)$ multiplications, by noticing that e.g. $x^8 = ((x^2)^2)^2$. However, the difference is small for small n.

```matlab
function [y errors] = polylog(n,z)
%% polylog — Computes the n—based polylogarithm of z: Li_n(z)
% Usage:   [y errors] = PolyLog(n,z)
% Input:   z < 1   : real/complex number or array
%          n > −4  : base of polylogarithm
% Output: y      ... value of polylogarithm
%         errors  ... number of errors

...%error checking etc.
version = 2;
switch n
case 1
    y = −log(1−z);
otherwise
switch version
case 1
% original, slower version
alpha = −log(z);
y = zeros(size(z));
j = find(abs(z)>0.55); % if |z| > 0.55
preterm = gamma(1−n)./alpha(j).^(1−n);
nominator = b(0) + ...
    − alpha(j).*( b(1) − 4*b(0)*b(4)/7/b(3) ) + ...
    + alpha(j).^2.*( b(2)/2 + b(0)*b(4)/7/b(2) + ...
    − 4*b(1)*b(4)/7/b(3) ) − alpha(j).^3.*( b(3)/6 + ...
    − 2*b(0)*b(4)/105/b(1) + b(1)*b(4)/7/b(2) + ...
    − 2*b(2)*b(4)/7/b(3) );
denominator = 1 + alpha(j).*4*b(4)/7/b(3) +...
    + alpha(j).^2.*b(4)/7/b(2) +...
    + alpha(j).^3.*2*b(4)/105/b(1) +...
    + alpha(j).^4.*b(4)/840/b(0);
y(j) = preterm + nominator ./ denominator;
j = find(abs(z)<=0.55); % if |z| <= 0.55
nominator = 6435*9^n.*S(n,z(j),8) − 27456*8^n*z(j).*S(n,z(j),7) + ...
+ 48048*7^n*z(j).^2.*S(n,z(j),6) − 44352*6^n*z(j).^3.*S(n,z(j),5) + ...
+ 23100*5^n*z(j).^4.*S(n,z(j),4) − 6720*4^n.*z(j).^5.*S(n,z(j),3) + ...
+ 1008*3^n*z(j).^6.*S(n,z(j),2) − 64*2^n*z(j).^7.*S(n,z(j),1);
denominator = 6435*9^n − 27456*8^n*z(j) + ...
+ 48048*7^n*z(j).^2 − 44352*6^n*z(j).^3 + ...
+ 23100*5^n*z(j).^4 − 6720*4^n*z(j).^5 + ...
+ 1008*3^n*z(j).^6 − 64*2^n*z(j).^7 + ...
+ z(j).^8;
y(j) = nominator ./ denominator;
```

```matlab
44   case 2
45   % new version optimized for array evaluation
46   y = zeros(size(z));
47   j = (z>0.55); % if |z| > 0.55
48   alpha = -log(z(j));
49   alphan = alpha;
50
51   preterm1 = gamma(1-n)./alpha.^(1-n);
52   den1 = ones(size(alpha));
53   nom1 = b(0)* den1;
54   nom1 = nom1 - alpha.*( b(1) - 4*b(0)*b(4)/7/b(3) );
55   den1 = den1 + alpha.*4*b(4)/7/b(3);
56   alphan = alphan.*alpha; %alpha.^2
57   nom1 = nom1 + alphan.* ...
58       ( b(2)/2 + b(0)*b(4)/7/b(2) - 4*b(1)*b(4)/7/b(3) );
59   den1 = den1 + alphan.*b(4)/7/b(2);
60   alphan = alphan.*alpha; %alpha.^3
61   nom1 = nom1 - alphan.* ...
62       ( b(3)/6 - 2*b(0)*b(4)/105/b(1) + b(1)*b(4)/7/b(2) + ...
63       - 2*b(2)*b(4)/7/b(3) );
64   den1 = den1 + alphan.*2*b(4)/105/b(1);
65   alphan = alphan.*alpha; %alpha.^4
66   den1 = den1 + alphan.*b(4)/840/b(0);
67   y(j) = (preterm1 + nom1./den1);
68   coeffs = [6435*9^n, -27456*8^n, 48048*7^n, -44352*6^n, ...
69             23100*5^n, -6720*4^n, 1008*3^n, -64*2^n, 1];
70   j = ~j; % if |z| <= 0.55
71   z = z(j);
72   den2 = zeros(size(z));
73   nom2 = den2; %zeros
74   s = den2; %zeros
75   % last term first
76   den2 = den2 + coeffs(end);
77   zn = ones(size(z));
78   for i = 1:( length(coeffs)-1 )
79       zn = zn.*z;
80       s = s + zn./i.^n;
81       nom2 = nom2 + coeffs(end-i)*s./zn;
82       den2 = den2 + coeffs(end-i)./zn;
83   end
84   % at the end, zn = z.^8
85   nom2 = nom2.*zn;
86   den2 = den2.*zn;
```

```matlab
87  y(j) = nom2./den2;
88  end
89  end
90  % define b
91  function out = b(i)
92      out = zeta(n-i);
93  end
94  % define partial sums S
95  function out = S(n,z,j)
96      out =0;
97      for i=1:j
98          out = out + z.^i./i^n;
99      end
100 end
101 ...%define zeta(x) etc.
102 end
```

Bibliography

[1] E. Fermi, "Sulla quantizzazione del gas perfetto monoatomico," *Rendiconti Lincei*, vol. 3, pp. 145–149, 1926.

[2] P. A. M. Dirac, "On the Theory of Quantum Mechanics," *Proc. R. Soc. Lond. A*, vol. 112, no. 762, pp. 661–677, 1926.

[3] S. N. Bose, "Plancks Gesetz und Lichtquantenhypothese," *Zeitschrift f\"{u} Physik*, vol. 26, p. 178, 1924.

[4] A. Einstein, "Quantentheorie des einatomigen idealen Gases," *Sitzungsber. Kgl. Preuss. Akad. Wiss.*, p. 261, 1924.

[5] A. Einstein, "Quantentheorie des einatomigen idealen Gases (Zweite Abhandlung)," *Sitzungsber. Kgl. Preuss. Akad. Wiss.*, p. 3, 1925.

[6] M. H. Anderson, J. R. Ensher, M. R. Matthews, C. E. Wieman, and E. a. Cornell, "Observation of bose-einstein condensation in a dilute atomic vapor," *Science (New York, N.Y.)*, vol. 269, pp. 198–201, July 1995.

[7] K. Davis, M.-O. Mewes, M. Andrews, N. Van Druten, D. Durfee, D. Kurn, and W. Ketterle, "Bose-Einstein condensation in a gas of sodium atoms," *Physical Review Letters*, vol. 75, no. 22, pp. 3969–3973, 1995.

[8] I. Bloch and W. Zwerger, "Many-body physics with ultracold gases," *Reviews of Modern Physics*, vol. 80, pp. 885–964, July 2008.

[9] T. Meyrath, F. Schreck, J. Hanssen, C.-S. Chuu, and M. Raizen, "Bose-Einstein condensate in a box," *Physical Review A*, vol. 71, p. 041604, Apr. 2005.

[10] S. Gupta, K. Murch, K. Moore, T. Purdy, and D. Stamper-Kurn, "Bose-Einstein Condensation in a Circular Waveguide," *Physical Review Letters*, vol. 95, p. 143201, Sept. 2005.

[11] S. Nascimbène, N. Navon, K. J. Jiang, F. Chevy, and C. Salomon, "Exploring the thermodynamics of a universal Fermi gas.," *Nature*, vol. 463, pp. 1057–60, Feb. 2010.

[12] T.-L. Ho and Q. Zhou, "Obtaining the phase diagram and thermodynamic quantities of bulk systems from the densities of trapped gases," *Nature Physics*, vol. 6, pp. 131–134, Dec. 2009.

[13] T. Yefsah, R. Desbuquois, L. Chomaz, K. J. Günter, and J. Dalibard, "Exploring the Thermodynamics of a Two-Dimensional Bose Gas," *Physical Review Letters*, vol. 107, p. 130401, Sept. 2011.

[14] M. J. H. Ku, A. T. Sommer, L. W. Cheuk, and M. W. Zwierlein, "Revealing the superfluid lambda transition in the universal thermodynamics of a unitary Fermi gas.," *Science (New York, N.Y.)*, vol. 335, pp. 563–7, Feb. 2012.

[15] T. Yefsah, R. Desbuquois, L. Chomaz, K. J. Günter, and J. Dalibard, "Exploring the Thermodynamics of a Two-Dimensional Bose Gas," *Physical Review Letters*, vol. 107, p. 130401, Sept. 2011.

[16] R. P. Smith, N. Tammuz, R. L. D. Campbell, M. Holzmann, and Z. Hadzibabic, "Condensed Fraction of an Atomic Bose Gas Induced by Critical Correlations," *Physical Review Letters*, vol. 107, p. 190403, Nov. 2011.

[17] T. E. Drake, Y. Sagi, R. Paudel, J. T. Stewart, J. P. Gaebler, and D. S. Jin, "Direct observation of the Fermi surface in an ultracold atomic gas," *Physical Review A*, vol. 86, p. 031601, Sept. 2012.

[18] Y. Sagi, T. E. Drake, R. Paudel, and D. S. Jin, "Measurement of the Homogeneous Contact of a Unitary Fermi Gas," *Physical Review Letters*, vol. 109, p. 220402, Nov. 2012.

[19] I. Gotlibovych, T. F. Schmidutz, S. Moulder, R. L. D. Campbell, N. Tammuz, R. J. Fletcher, A. L. Gaunt, S. Beattie, R. P. Smith, and Z. Hadzibabic, "A compact single-chamber apparatus for bose-einstein condensation of ^{87}Rb," *arXiv:1212.4108*, Dec. 2012.

[20] A. L. Gaunt, T. F. Schmidutz, I. Gotlibovych, R. P. Smith, and Z. Hadzibabic, "Bose-Einstein Condensation of Atoms in a Uniform Potential," *Physical Review Letters*, vol. 110, p. 200406, May 2013.

[21] T. F. Schmidutz, I. Gotlibovych, A. L. Gaunt, R. P. Smith, N. Navon, and Z. Hadzibabic, "Quantum Joule-Thomson Effect in a Saturated Homogeneous Bose Gas," *Physical Review Letters*, vol. 112, p. 040403, Jan. 2014.

[22] I. Gotlibovych, T. F. Schmidutz, A. L. Gaunt, N. Navon, R. P. Smith, and Z. Hadzibabic, "Observing the Ground-State Properties of an Interacting Homogeneous Bose Gas," *arXiv:1403.7081*, Mar. 2014.

[23] C. Pethick and H. Smith, *Bose-Einstein Condensation in Dilute Gases*. Cambridge University Press, second ed., 2008.

[24] V. Bagnato, D. E. Pritchard, and D. Kleppner, "Bose-Einstein condensation in an external potential," *Physical Review A*, vol. 35, no. 10, p. 4354, 1987.

[25] K. Huang, *Statistical Mechanics*. Wiley, second edi ed., 1987.

[26] S. Moulder, *Simple single chamber system for the condensation of dilute atomic gases*. PhD thesis, 2010.

[27] R. L. D. Campbell, *Thermodynamic properties of a Bose gas with tuneable interactions*. PhD thesis, University of Cambridge, 2011.

[28] N. Tammuz, *Thermodynamics of ultracold ^{39}K atomic Bose gases with tuneable interactions*. PhD thesis, University of Cambridge, 2011.

[29] Y.-J. Lin, A. Perry, R. Compton, I. Spielman, and J. Porto, "Rapid production of ^{87}Rb Bose-Einstein condensates in a combined magnetic and optical potential," *Physical Review A*, vol. 79, pp. 1–8, June 2009.

[30] J. Söding, D. Guéry-Odelin, P. Desbiolles, F. Chevy, H. Inamori, and J. Dalibard, "Three-body decay of a rubidium BoseEinstein condensate," *Applied Physics B*, vol. 69, pp. 257–261, Feb. 2014.

[31] R. N. Watts and C. Wieman, "Manipulating atomic velocities using diode lasers," *Optics Letters*, vol. 11, p. 291, May 1986.

[32] W. D. Phillips, J. V. Prodan, and H. J. Metcalf, "Laser cooling and electromagnetic trapping of neutral atoms," *Journal of the Optical Society of America B*, vol. 2, p. 1751, Nov. 1985.

[33] J. Schoser, A. Batär, R. Löw, V. Schweikhard, A. Grabowski, Y. Ovchinnikov, and T. Pfau, "Intense source of cold Rb atoms from a pure two-dimensional magneto-optical trap," *Physical Review A*, vol. 66, p. 023410, Aug. 2002.

[34] M. Zaiser, J. Hartwig, D. Schlippert, U. Velte, N. Winter, V. Lebedev, W. Ertmer, and E. Rasel, "Simple method for generating Bose-Einstein condensates in a weak hybrid trap," *Physical Review A*, vol. 83, pp. 1–4, Mar. 2011.

[35] I. Gotlibovych, *Single Chamber System for BEC Studies.* {CPGS} report, University of Cambridge, 2011.

[36] Triad Technology, Inc. Company website: http://www.triadtechno.com/.

[37] Oerlikon Leybold Vacuum UK. Company website: http://www.oerlikon.com/.

[38] VAT Vacuum Products Ltd. Company website: http://www.vatvalve.com/.

[39] Alvatec Production and Sales GesmbH. Company website: http://www.alvatec.com/.

[40] D. A. Steck, "Rubidium 87 D Line Data," *available online at http://steck.us/alkalidata (revision 2.1.4, 23 December 2010).*

[41] C. J. Foot, *Atomic Physics.* Oxford University Press, 2005.

[42] K. Liu and M. G. Littman, "Novel geometry for single-mode scanning of tunable lasers," *Optics letters*, vol. 6, pp. 117–8, Mar. 1981.

[43] M. de Labachelerie, H. Sasada, and G. Passedat, "Mode-hop suppression of Littrow grating-tuned lasers," *Applied optics*, vol. 32, pp. 269–274, June 1993.

[44] M. de Labachelerie, H. Sasada, and G. Passedat, "Mode-hop suppression of Littrow grating-tuned lasers: erratum," *Applied optics*, vol. 33, pp. 3817–9, June 1994.

[45] L. Ricci, M. Weidemüller, T. Esslinger, A. Hemmerich, C. Zimmermann, V. Vuletic, W. König, and T. Hänsch, "A compact grating-stabilized diode laser system for atomic physics," *Optics Communications*, vol. 117, no. 5-6, pp. 541–549, 1995.

[46] A. S. Arnold, J. S. Wilson, and M. G. Boshier, "A simple extended-cavity diode laser," *Review of Scientific Instruments*, vol. 69, no. 3, p. 1236, 1998.

[47] C. J. Hawthorn, K. P. Weber, and R. E. Scholten, "Littrow configuration tunable external cavity diode laser with fixed direction output beam," *Review of Scientific Instruments*, vol. 72, no. 12, p. 4477, 2001.

[48] TOPTICA Photonics AG. Company website: http://www.toptica.com/.

[49] G. Bjorklund, "Frequency-modulation spectroscopy: a new method for measuring weak absorptions and dispersions," *Optics Letters*, vol. 5, no. 1, pp. 15–17, 1980.

[50] Thorlabs Inc. Company website: http://www.throlabs.com/.

[51] T. Lauber, J. Küber, O. Wille, and G. Birkl, "Optimized Bose-Einstein-condensate production in a dipole trap based on a 1070-nm multifrequency laser: Influence of enhanced two-body loss on the evaporation process," *Physical Review A*, vol. 84, pp. 1–8, Oct. 2011.

[52] National Instruments. Company website: http://www.ni.com/.

[53] H. J. Metcalf and P. Van Der Straten, *Laser Cooling and Trapping*. Springer, 1999.

[54] D. Wineland and W. Itano, "Laser cooling of atoms," *Physical Review A*, vol. 20, pp. 1521–1540, Oct. 1979.

[55] P. Lett, R. Watts, C. Westbrook, W. Phillips, P. Gould, and H. Metcalf, "Observation of Atoms Laser Cooled below the Doppler Limit," *Physical Review Letters*, vol. 61, pp. 169–172, July 1988.

[56] J. Dalibard and C. Cohen-Tannoudji, "Laser cooling below the Doppler limit by polarization gradients: simple theoretical models," *Journal of the Optical Society of America B*, vol. 6, p. 2023, Nov. 1989.

[57] C. N. Cohen-Tannoudji and W. D. Phillips, "New Mechanisms for Laser Cooling," *Physics Today*, vol. 43, no. 10, p. 33, 1990.

[58] S. Chu, L. Hollberg, J. Bjorkholm, A. Cable, and A. Ashkin, "Three-dimensional viscous confinement and cooling of atoms by resonance radiation pressure," *Physical Review Letters*, vol. 55, pp. 48–51, July 1985.

[59] A. Aspect, E. Arimondo, R. Kaiser, N. Vansteenkiste, and C. Cohen-Tannoudji, "Laser Cooling below the One-Photon Recoil Energy by Velocity-Selective Coherent Population Trapping," *Physical Review Letters*, vol. 61, pp. 826–829, Aug. 1988.

[60] W. Petrich, M. H. Anderson, J. R. Ensher, and E. a. Cornell, "Behavior of atoms in a compressed magneto-optical trap," *Journal of the Optical Society of America B*, vol. 11, p. 1332, Aug. 1994.

[61] K. B. Davis, M. O. Mewes, and W. Ketterle, "An analytical model for evaporative cooling of atoms," *Appl Phys B*, vol. 60, no. 2-3, p. 155, 1995.

[62] I. Gotlibovych, "Microwave Manipulation of Ultra-cold Atoms," Master's thesis, 2010.

[63] C. Bradley, C. Sackett, J. Tollett, and R. Hulet, "Evidence of Bose-Einstein condensation in an atomic gas with attractive interactions," *Physical Review Letters*, vol. 75, no. 9, pp. 1687–1691, 1995.

[64] M. Barrett, J. Sauer, and M. Chapman, "All-Optical Formation of an Atomic Bose-Einstein Condensate," *Physical Review Letters*, vol. 87, p. 010404, June 2001.

[65] R. Grimm, M. Weidemüller, and Y. Ovchinnikov, "Optical dipole traps for neutral atoms," *Advances in atomic, molecular, and optical physics*, vol. 42, pp. 95–170, 2000.

[66] T. Kinoshita, T. Wenger, and D. Weiss, "All-optical Bose-Einstein condensation using a compressible crossed dipole trap," *Physical Review A*, vol. 71, Jan. 2005.

[67] J.-F. Clément, J.-P. Brantut, M. Robert-de Saint-Vincent, R. A. Nyman, A. Aspect, T. Bourdel, and P. Bouyer, "All-optical runaway evaporation to Bose-Einstein condensation," *Physical Review A*, vol. 79, p. 061406, June 2009.

[68] D. Jacob, E. Mimoun, L. De Sarlo, M. Weitz, J. Dalibard, and F. Gerbier, "Production of sodium BoseEinstein condensates in an optical dimple trap," *New Journal of Physics*, vol. 13, p. 065022, June 2011.

[69] K. Arnold and M. Barrett, "All-optical BoseEinstein condensation in a 1.06μm dipole trap," *Optics Communications*, vol. 284, pp. 3288–3291, June 2011.

[70] C.-L. Hung, X. Zhang, N. Gemelke, and C. Chin, "Accelerating evaporative cooling of atoms into Bose-Einstein condensation in optical traps," *Physical Review A*, vol. 78, pp. 1–4, July 2008.

[71] G. Kleine Büning, J. Will, W. Ertmer, C. Klempt, and J. Artl, "A slow gravity compensated Atom Laser," *Applied Physics B*, vol. 100, no. 1, pp. 117–123, 2010.

[72] E. Burt, R. Ghrist, C. Myatt, M. Holland, E. Cornell, and C. Wieman, "Coherence, Correlations, and Collisions: What One Learns about Bose-Einstein Condensates from Their Decay," *Physical Review Letters*, vol. 79, pp. 337–340, July 1997.

[73] W. Ketterle, S. Durfee, M. Stamper, I. The, and E. Fermi, "Making, probing and understanding Bose-Einstein condensates," 1996.

[74] G. Reinaudi, T. Lahaye, Z. Wang, and D. Guéry-Odelin, "Strong saturation absorption imaging of dense clouds of ultracold atoms," *Optics Letters*, vol. 32, no. 21, p. 3143, 2007.

[75] PCO AG. Company website: http://www.pco.de/.

[76] N. Tammuz, R. Smith, R. Campbell, S. Beattie, S. Moulder, J. Dalibard, and Z. Hadzibabic, "Can a Bose Gas Be Saturated?," *Physical Review Letters*, vol. 106, June 2011.

[77] R. P. Smith, R. L. D. Campbell, N. Tammuz, and Z. Hadzibabic, "Effects of Interactions on the Critical Temperature of a Trapped Bose Gas," *Physical Review Letters*, vol. 106, p. 250403, June 2011.

[78] F. Gerbier, J. Thywissen, S. Richard, M. Hugbart, P. Bouyer, and A. Aspect, "Critical Temperature of a Trapped, Weakly Interacting Bose Gas," *Physical Review Letters*, vol. 92, p. 030405, Jan. 2004.

[79] C. Sanner, E. Su, A. Keshet, R. Gommers, Y.-i. Shin, W. Huang, and W. Ketterle, "Suppression of Density Fluctuations in a Quantum Degenerate Fermi Gas," *Physical Review Letters*, vol. 105, July 2010.

[80] G. Baym and C. Pethick, "Ground-state properties of magnetically trapped Bose-condensed rubidium gas," *Physical review letters*, vol. 76, pp. 6–9, Jan. 1996.

[81] A. L. Gaunt and Z. Hadzibabic, "Robust digital holography for ultracold atom trapping.," *Scientific reports*, vol. 2, p. 721, Jan. 2012.

[82] A. Gaunt, *Unconventional Bose-condensed Gases: Tuning Interactions & Geometry*. PhD thesis, 2013.

[83] Laser Quantum UK. Company website: http://www.laserquantum.com/.

[84] P. Grüter, D. Ceperley, and F. Laloë, "Critical Temperature of Bose-Einstein Condensation of Hard-Sphere Gases," *Physical Review Letters*, vol. 79, pp. 3549–3552, Nov. 1997.

[85] M. Bijlsma and H. Stoof, "Renormalization group theory of the three-dimensional dilute Bose gas," *Physical Review A*, vol. 54, pp. 5085–5103, Dec. 1996.

[86] S. Grossmann and M. Holthaus, "Bose-Einstein condensation in a cavity," *Zeitschrift fr Physik B Condensed Matter*, vol. 97, pp. 319–326, June 1995.

[87] S. Grossmann and M. Holthaus, "On Bose-Einstein condensation in harmonic traps," *Physics Letters A*, vol. 208, pp. 188–192, Nov. 1995.

[88] S. Giorgini, L. Pitaevskii, and S. Stringari, "Condensate fraction and critical temperature of a trapped interacting Bose gas," *Physical Review A*, vol. 54, pp. R4633–R4636, Dec. 1996.

[89] F. Dalfovo, S. Giorgini, and S. Stringari, "Theory of Bose-Einstein condensation in trapped gases," *Reviews of Modern Physics*, vol. 71, pp. 463–512, Apr. 1999.

[90] F. Gerbier, J. Thywissen, S. Richard, M. Hugbart, P. Bouyer, and a. Aspect, "Critical Temperature of a Trapped, Weakly Interacting Bose Gas," *Physical Review Letters*, vol. 92, pp. 1–4, Jan. 2004.

[91] R. P. Smith and Z. Hadzibabic, "Effects of interactions on Bose-Einstein condensation of an atomic gas," in *Physics of Quantum Fluids* (A. Bramati and M. Modugno, eds.), ch. 16, pp. 341–359, Springer, 2013.

[92] A. Jaouadi, N. Gaaloul, B. Viaris de Lesegno, M. Telmini, L. Pruvost, and E. Charron, "Bose-Einstein condensation in dark power-law laser traps," *Physical Review A*, vol. 82, Aug. 2010.

[93] A. Jaouadi, M. Telmini, and E. Charron, "Bose-Einstein condensation with a finite number of particles in a power-law trap," *Physical Review A*, vol. 83, Feb. 2011.

[94] A. L. Gaunt, R. J. Fletcher, R. P. Smith, and Z. Hadzibabic, "A superheated Bose-condensed gas," *Nature Physics*, vol. 9, pp. 271–274, Mar. 2013.

[95] V. N. Popov, *Functional Integrals and Collective Excitations*. Cambridge: Cambridge University Press, 1987.

[96] A. Griffin, "Conserving and gapless approximations for an inhomogeneous Bose gas at finite temperatures," *Physical Review B*, vol. 53, pp. 9341–9347, Apr. 1996.

[97] D. A. Huse and E. D. Siggia, "The density distribution of a weakly interacting bose gas in an external potential," *Journal of Low Temperature Physics*, vol. 46, pp. 137–149, Jan. 1982.

[98] V. Goldman, I. Silvera, and A. Leggett, "Atomic hydrogen in an inhomogeneous magnetic field: Density profile and Bose-Einstein condensation," *Physical Review B*, vol. 24, pp. 2870–2873, Sept. 1981.

[99] S. Giorgini, L. Pitaevskii, and S. Stringari, "Condensate fraction and critical temperature of a trapped interacting Bose gas," *Physical Review A*, vol. 54, pp. R4633–R4636, Dec. 1996.

[100] J. Dalibard, "Using the Popov approximation for a Bose gas," *unpublished*, 2010.

[101] J. Flusser, J. Boldyš, and B. Zitová, "Invariants to Convolution in Arbitrary Dimensions," *Journal of Mathematical Imaging and Vision*, vol. 13, pp. 101–113, 2000.

[102] J. Ensher, D. Jin, M. Matthews, C. Wieman, and E. Cornell, "Bose-Einstein Condensation in a Dilute Gas: Measurement of Energy and Ground-State Occupation," *Physical Review Letters*, vol. 77, pp. 4984–4987, Dec. 1996.

[103] C. R. Monroe, E. A. Cornell, C. A. Sackett, C. J. Myatt, and C. E. Wieman, "Measurement of Cs-Cs elastic scattering at T=30 μK," *Physical Review Letters*, vol. 70, pp. 414–417, Jan. 1993.

[104] D. S. Kothari and B. N. Srivasave, "Joule-Thomson Effect and Quantum Statistics," *Nature (London)*, vol. 140, p. 970, 1937.

[105] E. Timmermans, "Degenerate Fermion Gas Heating by Hole Creation," *Physical Review Letters*, vol. 87, p. 240403, Nov. 2001.

[106] A. Bernhardt and B. Shore, "Coherent atomic deflection by resonant standing waves," *Physical Review A*, vol. 23, pp. 1290–1301, Mar. 1981.

[107] P. Martin, B. Oldaker, A. Miklich, and D. Pritchard, "Bragg scattering of atoms from a standing light wave," *Physical Review Letters*, vol. 60, pp. 515–518, Feb. 1988.

[108] W. Bragg, "The diffraction of short electromagnetic waves by a crystal," *Proceedings of the Cambridge Philosophical Society*, vol. 17, pp. 43–57, 1913.

[109] C. Shull, "Early development of neutron scattering," *Reviews of Modern Physics*, vol. 67, pp. 753–757, Oct. 1995.

[110] J. Stenger, S. Inouye, A. Chikkatur, D. Stamper-Kurn, D. Pritchard, and W. Ketterle, "Bragg Spectroscopy of a Bose-Einstein Condensate," *Physical Review Letters*, vol. 82, pp. 4569–4573, June 1999.

[111] D. Stamper-Kurn, A. Chikkatur, A. Görlitz, S. Inouye, S. Gupta, D. Pritchard, and W. Ketterle, "Excitation of Phonons in a Bose-Einstein Condensate by Light Scattering," *Physical Review Letters*, vol. 83, pp. 2876–2879, Oct. 1999.

[112] F. Zambelli, L. Pitaevskii, D. Stamper-Kurn, and S. Stringari, "Dynamic structure factor and momentum distribution of a trapped Bose gas," *Physical Review A*, vol. 61, pp. 063608–, May 2000.

[113] J. Steinhauer, R. Ozeri, N. Katz, and N. Davidson, "Excitation Spectrum of a Bose-Einstein Condensate," *Physical Review Letters*, vol. 88, p. 120407, Mar. 2002.

[114] J. Steinhauer, N. Katz, R. Ozeri, N. Davidson, C. Tozzo, and F. Dalfovo, "Bragg Spectroscopy of the Multibranch Bogoliubov Spectrum of Elongated Bose-Einstein Condensates," *Physical Review Letters*, vol. 90, p. 060404, Feb. 2003.

[115] R. Ozeri, J. Steinhauer, N. Katz, and N. Davidson, "Direct Observation of the Phonon Energy in a Bose-Einstein Condensate by Tomographic Imaging," *Physical Review Letters*, vol. 88, p. 220401, May 2002.

[116] O. Morsch, J. Müller, M. Cristiani, D. Ciampini, and E. Arimondo, "Bloch Oscillations and Mean-Field Effects of Bose-Einstein Condensates in 1D Optical Lattices," *Physical Review Letters*, vol. 87, p. 140402, Sept. 2001.

[117] L. Fallani, F. S. Cataliotti, J. Catani, C. Fort, M. Modugno, M. Zawada, and M. Inguscio, "Optically Induced Lensing Effect on a Bose-Einstein Condensate Expanding in a Moving Lattice," *Physical Review Letters*, vol. 91, p. 240405, Dec. 2003.

[118] C. Kittel, *Introduction to Solid State Physics*. John Wiley & Sons, Inc, 8 ed., 2005.

[119] M. J. Steel and W. Zhang, "Bloch function description of a Bose-Einstein condensate in a finite optical lattice," *arXiv:cond-mat/9810284*, Oct. 1998.

[120] F. Dalfovo, C. Minniti, S. Stringari, and L. Pitaevskii, "Nonlinear dynamics of a Bose condensed gas," *Physics Letters A*, vol. 227, pp. 259–264, Mar. 1997.

[121] F. Gerbier, J. H. Thywissen, S. Richard, M. Hugbart, P. Bouyer, and A. Aspect, "Experimental study of the thermodynamics of an interacting trapped Bose-Einstein condensed gas," *Physical Review A*, vol. 70, p. 013607, July 2004.

[122] T. F. Schmidutz, *PhD Thesis, in preparation*. PhD thesis, University of Cambridge, 2014.

[123] Y. Castin and R. Dum, "Bose-Einstein Condensates in Time Dependent Traps," *Physical Review Letters*, vol. 77, pp. 5315–5319, Dec. 1996.

[124] N. Goldman, J. Dalibard, A. Dauphin, F. Gerbier, M. Lewenstein, P. Zoller, and I. B. Spielman, "Direct imaging of topological edge states in cold-atom systems.," *Proceedings of the National Academy of Sciences of the United States of America*, vol. 110, pp. 6736–41, Apr. 2013.

[125] C. Ye, *Tunable external cavity diode lasers*. World Scientific Pub Co Inc, 2004.

[126] P. Richman, *Development of laboratory equipment for the trapping and cooling of atomic gases including a grating-stabilised external cavity diode laser*. PhD thesis, 2010.

[127] M. Kuhnert, "polylog MATLAB function," 2012.

[128] V. Bhagat, R. Bhattacharya, and D. Roy, "On the evaluation of generalized BoseEinstein and FermiDirac integrals," *Computer Physics Communications*, vol. 155, pp. 7–20, Sept. 2003.

[129] W. Research, "PolyLog Mathematica function."

[130] I. Gotlibovych, "polylog MATLAB function," 2013.